SOIL PENETROMETER WITH RAMAN SAMPLING, FLUORESCENCE AND REFLECTED LIGHT IMAGING: A FEASIBILITY STUDY

By

Youssef Kadiri

A thesis submitted in partial fulfillment
of the requirements for the degree

of

Masters of Science

in

Electrical Engineering

MONTANA STATE UNIVERSITY
Bozeman, Montana

January, 2005

APPROVAL

of a thesis submitted by

Youssef Kadiri

This thesis has been read by each member of the thesis committee and has been found to be satisfactory regarding content, English usage, format, citation, bibliographic style, and consistency, and is ready for submission to the college of Graduate Studies.

Dr. David Dickensheets

Approved for the Department of Electrical & Computer Engineering

Dr. James Peterson

Approved for the College of Graduate Studies

Dr. Bruce McLeod

STATEMENT OF PERMISSION OF USE

In presenting this thesis in partial fulfillment of the requirements for a master's degree at Montana State University, I agree that the library shall make it available to borrowers under the rules of the library.

If I have indicated my intention to copyright this thesis by including a copyright notice page, copying is allowable only for scholarly purposes, consistent with "fair use" as prescribed in the U.S. Copyright Law. Requests for permission for extended quotation from or reproduction of this thesis in whole or in parts may be granted only by the copyright holder.

Youssef Kadiri

December, 2004

ACKNOWLEDGEMENTS

I would like to express my sincere gratitude to my advisor, Professor David Dickensheets, for his guidance, support, for all the valuable knowledge he has taught me, and for giving me the great opportunity to be part his research group.

I would like also to thank Professor Joe Shaw and Professor Richard Wolff for their evaluations and for being members of my graduate committee.

My sincere gratitude to the electrical engineering department's faculty and to the Montanans with whom I had very pleasurable and memorable times during my graduate studies.

Warmest thanks to my parents, family, and friends for their support.

TABLE OF CONTENTS

TABLE OF CONTENTS - CONTINUED

LIST OF TABLES

LIST OF FIGURES

Figure Page

LIST OF FIGURES-CONTINUED

Figure Page

LIST OF FIGURES-CONTINUED

Figure Page

LIST OF FIGURES-CONTINUED

Figure Page

LIST OF FIGURES-CONTINUED

Figure Page

ABSTRACT

This thesis describes the feasibility and capabilities of a Fluorescence Imaging and Raman Probe (FIRP). This miniature instrument will combine reflected light and fluorescence imaging and Raman spectroscopy for potential exobiology or terrestrial environmental use. With the help of a penetrometer, the probe might be used to assess the presence of life on Mars and gain an understanding of Martian soil. Furthermore, this thesis will delineate how this penetrometer may be used to detect underground constituents and pollutants present on our own planet.

The proposed FIRP will be incorporated into a penetrometer that will go several meters below the surface seeking bio-signatures and information about soil composition. Microscopic imaging with reflected light will provide morphological context, fluorescence imaging can provide biomass detection, and Raman spectrometry can provide chemical identification of imaged material. The fluorescence technique will mainly depend on the performance of a non-cooled low-noise monochrome imaging camera, optical filters, and high efficiency light emitting diodes in the UV and visible. This miniature instrument will be connected by optical fiber to a surface platform that will host the Raman spectrometer and Raman laser excitation source.

This thesis will show the experimental results of a bench-top proof of concept system. Images and spectra were collected and analyzed. Important choices and characteristics of the optical design are discussed relative to Raman and fluorescence detection. Finally, the thesis will propose a prototype of a compact device that combines both sensing methods and is compatible with a penetrometer platform.

CHAPTER ONE

INTRODUCTION

No single scientific method can reveal all the different chemical and physical aspects of a structure as diverse and complex as soil. Soil has numerous characteristics: its composition, fertility, density, and its moisture just to cite a few. Despite the complexity of soil, the combination of Raman spectrometry and fluorescence imaging can provide some relevant analytical information. Fluorescence imaging can locate fluorescing elements and Raman spectrometry can tell us about their chemical make-up. Additionally, real time imaging can provide us with sound ideas about soil morphology. For our concern, we are interested in developing a sub-surface probe able to assess soil composition and detect the presence of pollutants and bio-signatures. The fluorescence imaging Raman penetrometer (FIRP) offers this opportunity.

Optical Probe for Martian Exploration

This work has been funded by the National Aeronautics and Space Administration (NASA). It has the objective of better understanding the Martian soil and Martian biology. So far, there is no confirmation that life exists or has ever existed on the surface of Mars and the earlier missions failed to prove it [1] [2] [3]. But, there is emerging evidence that the chemical and physical properties of early Earth and Mars were very similar [4]. The Viking missions proved that most essential elements that compose

biological matter are present on Mars. In fact, elements such as C, H, O, N, P, K, Mg, S and Ca were detected through X-ray fluorescence [5]. In addition, recent studies of Martian history suggest the presence of liquid water sometime during its past, and the previous missions to Mars (Mariner 9, Viking 1 and 2 Pathfinder and Mars Global surveyor) largely stressed that [1] [2] [3]. Like Earth, Mars has polar ice caps; the southern cap is mostly dry ice of frozen carbon dioxide and the northern cap is mostly composed of water ice. The rest of the planet is heavily cratered and shows traces of violent volcanic activity - the largest in the solar system [6]. Even though liquid water disappeared from the surface of Mars some 3.8 million years ago, it might exist deep beneath the surface, which leads to the hypothesis that beneath the Martian surface there may be life.

On Mars, carbon dioxide gas is the major constituent of the atmosphere; it is also the major filter of UV radiation. However, UV radiation wavelengths above 200 nm penetrate the atmosphere, which would make life on the surface of the red planet practically impossible. In addition, the extremely cold and dry climate (between –123 ^{o}C to 25 ^{o}C) would not allow the presence of liquid water [6]. Moreover, the presence of strongly oxidizing agents on the Martian surface would make the formation of organic compounds very improbable. The depth of the oxidized layer has been estimated to range from 3 to 5 meters [7]. Therefore, the subsurface and the interior of rocks remain one of the potential oases for microbial communities.

Since liquid water was once abundant on the surface of Mars, primitive Martian life may have existed as well. Some other potential sites for exobiological activity are paleolakes, pre-historical fluvial channels, and floodplains [8]. Therefore, understanding

the history of water on Mars is very important in selecting appropriate landing sites for conducting penetrometer tests. Indeed, landing sites should be carefully selected as some areas might be more hospitable to life than others and may require less drilling depths.

It has been proven that Earth's sub-surface microbial community density diminishes with depth; however, the depth in which life is still present on our planet is still unknown.

There has been a continuous effort to develop various autonomous drilling machines for the Martian exobiology research program. In 1975, the Viking Lander could not go below 25 cm of depth [3]. Recently, the Beagle 2 from the European Space Agency (ESA), was scheduled to land in Mars on 2004 [9]. Its rover was equipped with a penetrometer, or mole that will search for life traces underneath rocks to a depth between 1 and 2 meters. Unfortunately, the Beagle 2 mission to Mars did not succeed. Another European Lander, the Vanguard, is expected to follow with a deeper penetration capability of 5 meters [11]. More ambitious projects suggest the subsurface penetration of 200 to 300 meters [12]. Hence, deep drilling remains the ultimate approach in detecting life on Mars.

Figure 1.1: The Vanguard rover with three ground penetrating moles (European space agency ESA) after [11].

Different sensing methods were used in the previous Martian explorations. For example, the Viking lander used an X-ray fluorescence spectrometer for the detection of chemical elements, Mass spectrometer, and gas chromatograph; to detect elemental or molecular composition [13]. Mass spectrometry specifically was employed for detecting traces of water. Recently, the Beagle 2 was equipped with a Mossbauer and an X-ray spectrometer to give sample information based on valence state and electron intensities respectively [9][10]. All these techniques have advantages and drawbacks. Their success depends on the targeted element or molecule. Plus, not all of these sensors can be used with a penetrometer. The Raman spectrometry should not be taken as a substitute of all these previously used techniques. However, Raman and fluorescence techniques, used together, offer the possibility of detecting a multitude of organic and inorganic substances, which makes them suitable for Martian exploration.

Bio-signatures

The Antarctic is home to various life forms in the most remote and hostile environment on earth. One of these is Cyanobacteria, a photosynthetic microbe that can resist the extremely cold Antarctic temperature and the UVB radiation (290-320 nm). The cyanobacteria use various pigments to protect themselves from the high UVB influx [14]. These pigments proved to be recognizable with their unique Raman spectra [15]. Other oases of life were even found in places where there was almost no trace of liquid water (Victoria Valley) [16]. Iceland hot springs is another example, where thermophilic organisms anaerobically respire using nitrate [17]. These types of microorganisms would be the most relevant for understanding the Martian ecosystem. Hence, there are several microbiological processes naturally occurring on earth that have no requirement for the presence of liquid water, and occurring under very hostile environments. These living microorganisms may have analogues on the subsurface of Mars.

The cell has many constituents that can be detected by fluorescence or by Raman spectroscopy. All microorganisms use a similar genetic code stored in the DNA and translated into the RNA and into proteins. Some cells take energy from solar radiation with the help of photosynthetic pigments such as chlorophyll. DNA, amino-acids, enzymes, and photosynthetic pigments can be detected through their auto-fluorescence.

Tippkotter studied the primary fluorescence of soil organic matter, microorganisms, minerals, and cellular constituents and found that many of those have a strong to moderate primary fluorescence [18]. Hence, fluorescence could be valuable tool

for detecting life in Mars; Raman spectrometry coupled with primary fluorescence imaging can help us locate and subsequently identify bio-matter.

Optical Probe for Environmental Purposes

While it can be used to explore the Martian subsurface, a soil penetrometer also can be employed on earth with the objective of better understanding our soil composition and detecting various pollutants. The problem of hazardous waste generation, storage, and recycling has become a major concern. The movement of chemicals into the soil depends on the chemical properties of the waste and on the physical properties of the soil. Also, the properties of the soil play an important role in the absorption and the degradation of waste.

On our planet, wide ranges of pollutants reach the underground and affect its natural ecosystem. These can be pesticides, inorganic fertilizers, heavy metals, acids, fuels and other harmful solvents. The most widespread industrial chemical components regarded as pollutants are the heavy metals (Cd, Pb, Hg), nitrous oxides (NO_2), sulfuric compounds (SO_2) and polycyclic hydrocarbons [19]. Soil ecosystems are complex and not fully understood, and the impact of the pollutants may be extremely strong.

Therefore, there is an urgent need for a sub-terrestrial instrument that will assess the impact of pollutants on the biodiversity and stability of the soil inhabiting microorganisms. These toxic materials are also very dangerous for the underground water resources. Understanding the movement of those toxic elements is also very important in understanding the hazards they pose. In our case, we are particularly interested in the

detection of poly-aromatic hydrocarbons. Their fluorescence proved to be highly sensitive to ultraviolet light. Again, the combination of reflected light imaging, Raman spectrometry, and fluorescence imaging can help us detect many of the toxic materials.

Fluorescence

Fluorescence and Raman scattering are two separate physical phenomena. Fluorescence happens when an element absorbs light and emits light of different wavelengths. Such elements are called fluorophores or fluochromes. Atoms or molecules have many electronic states in addition to the one of lowest energy that we call the ground state. When the atom or molecule is exposed to electromagnetic radiation, the absorbed photonic energy moves it from the ground state to the excited electronic state. The excited state is also referred as the unstable state. Once excited, the element can re-emit photons of different frequencies. The emitted wavelengths will depend on the various transition states. When electrons cascades through these intermediate electronic states the atom emits photons of lower frequencies corresponding to the energy difference of the excited state and the intermediate electronic states. The process can also be non-radiative and energy can be lost and dissipated as heat. The excitation-emission process can be extremely fast- in the order of nanoseconds [20].

The difference between the excitation wavelength and the emission wavelength is known as the Stoke's shift after the British scientist who first discovered this phenomenon.

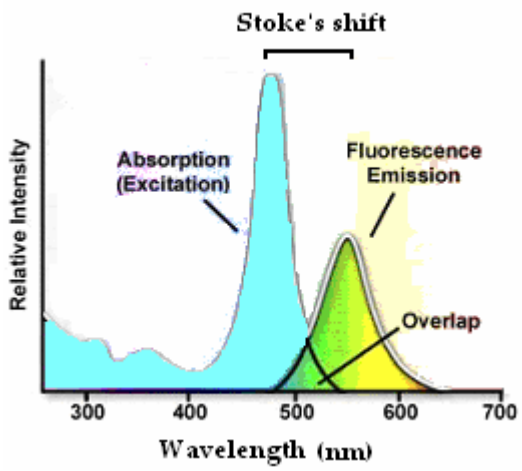

Figure 1.2: Typical excitation and emission spectra of a fluorophore after [20].

Many theories have been developed to understand why an element fluoresces in a particular wavelength, and a broad documentation is available for the excitation and emission spectra of biological and chemical elements. It has been proven that environmental factors have a big influence on the peak excitation and emission wavelengths of the fluorescent material. The fluorescence signal often shows sensitivity to the nature of the solvent, pH of the solution, temperature, pressure, and excitation light intensity, just to cite a few. For example, organic compounds fluoresce more intensely at low temperatures [21]. As illustrated in figure 1.2, the absorption-emission spectral diagram of a fluorescing element may overlap.

The following illustration shows the apparatus of a typical fluorescence microscope.

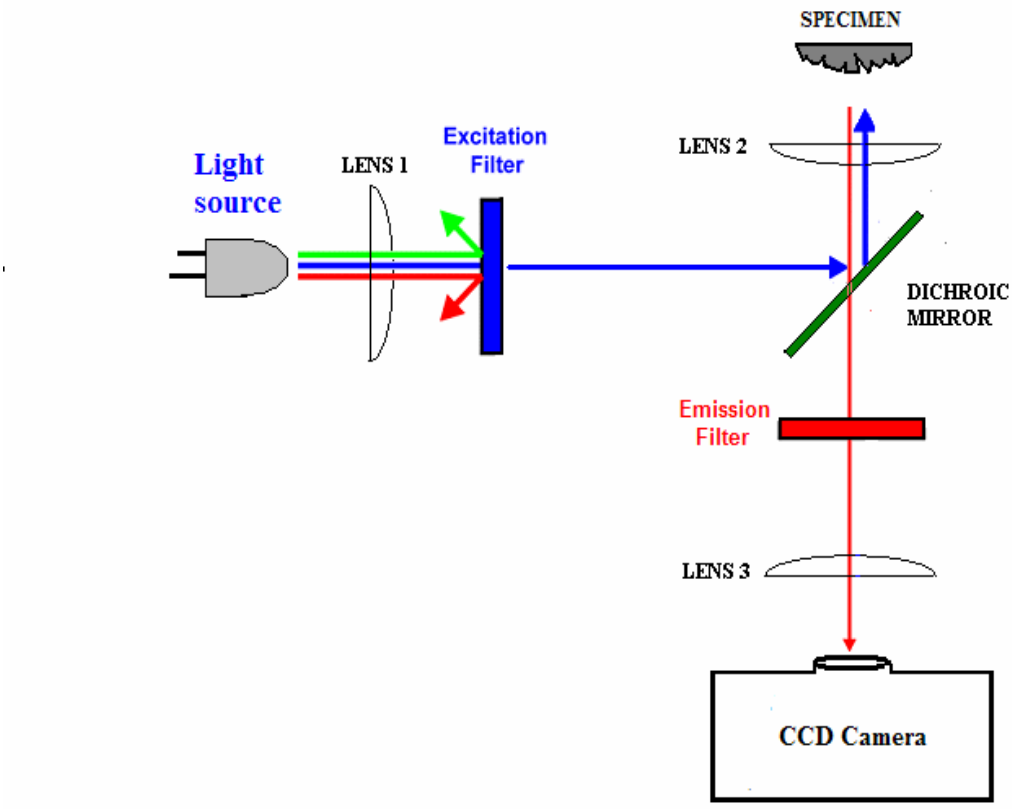

Figure 1.3: Basic apparatus of a fluorescence microscope.

Separating the excitation and emission wavelengths is very important. This is typically done by a proper selection of filters to block or pass specific wavelengths. Basically, there are three categories of filters used in a fluorescence microscope: excitation filter, emission filter and a 45^{o} angled dichroic mirror. The essential task of the fluorescence microscope is to permit excitation light to irradiate the specimen and then to collect and filter the much weaker emitted fluorescent light.

Proper selection of filters is the key to a successful fluorescence probe. The properties of the excitation filter will depend on the illumination source. Similarly, the emission filter or barrier filter will absorb the excitation wavelengths and permit only fluorescence light to reach the detector. Dichroic mirrors are special filters designed to efficiently reflect excitation wavelengths and pass emission wavelengths.

Fluorescence and reflected light imaging will give us important information that will help us recognize an entity by its morphology and its fluorescence. In addition to that, Raman spectroscopy will further confirm the presence of a bio-signature or a toxic element by probing chemical identification in the cases where a Raman spectrum may be obtained.

Raman Spectroscopy

The principle of Raman spectroscopy relies on a particular scattering principle discovered by the Indian physicist, C. V. Raman, in 1928 [22]. Raman spectroscopy is based on the scattering of monochromatic laser radiation due to its interaction with the molecular vibrations and rotations, also refereed to as inelastic scattering of photons by molecules.

In Raman spectroscopy, the incident light loses energy to the molecule vibrations. Frequencies from the vibrations and rotations of molecules will give us information about the molecular bonding. The energy of the scattered wavelengths is less than the energy of the incident light. The frequency difference corresponds to the various vibrations and rotations of the target molecule. These frequencies can be larger and smaller than the

excitation light frequency. Higher frequency signals are known as anti-stokes whereas low frequency signals are referred to as stokes. Anti-stokes emission is obtained when the target molecules are already in an excited state. Stokes scattering is much more common than anti-Stokes scattering because, at common temperatures, a molecule is most likely to be in its ground vibrational state. Typically, only Stokes Raman scattering is used in spectroscopy. A Raman spectrum is a plot of the intensity of Raman scattered radiation as a function of the frequency difference from the incident radiation frequency in wavenumbers (cm^{-1}). This difference is called the Raman shift. Although the Raman shift is independent of the frequency of the incident radiation, the Raman emission signal is inversely proportional to the excitation wavelength. The Raman spectrum will give a unique fingerprint of each specimen.

Long excitation laser wavelengths may be used to decrease the effect of fluorescence, as most samples exhibit a native fluorescence at short wavelengths that obscures the Raman signal [23].

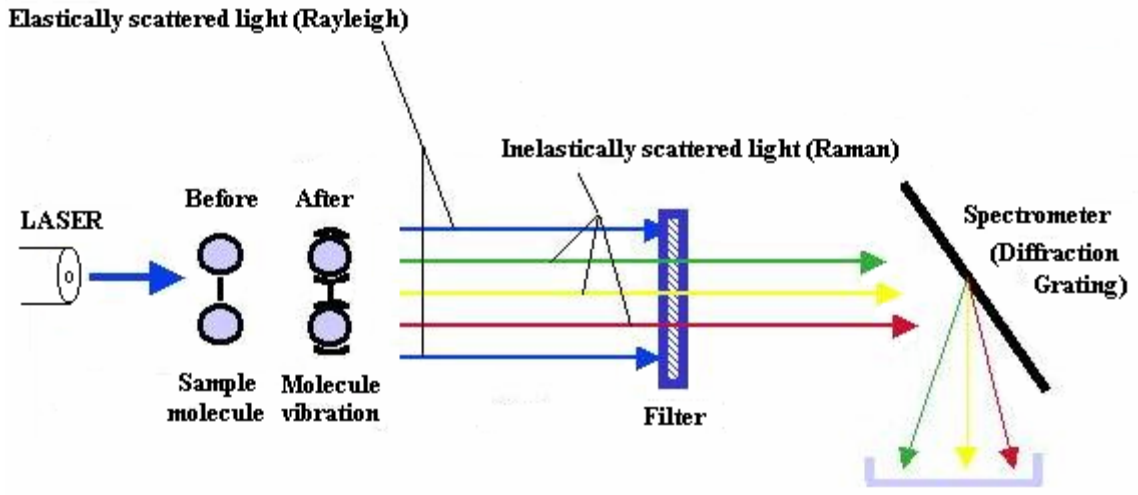

Figure 1.4: Illustration of Raman spectroscopy principle.

The intensities of the scattered radiation are measured by the spectrometer. To eliminate the much stronger Rayleigh scattering, notch filters are typically used. In the spectrometer, a grating can be used to disperse the scattered photons according to their wavelengths.

Optoelectronic devices have progressed dramatically in the past decade as a consequence of major achievements in solid-state technology. As a result, efficient diode lasers are now available from the visible to the infrared and have been demonstrated to work properly with Raman instruments. Moreover, CCD arrays became much more sensitive. Currently, Raman spectroscopy is employed successfully to solve complex analytical problems such as determining chemical structures of inorganic and organic materials. In addition, the remote sensing of contaminants, gases, vapors, aerosols, liquids and solids was also made possible [24]. Due to the successive improvements in optoelectronics and solid state physics, Raman spectrometers have become much smaller, practical and convenient for Martian explorations [25].

Thesis Organization

This thesis explains the development of a Raman and Fluorescence probe for underground exploration. First the fluorescence experimental setup will be introduced, followed by a discussion of the optical criteria important for fluorescence imaging and Raman sampling. For imaging, we will consider a suitable sensor, evaluate aspects of noise, and assess the need for cooling.

In each chapter we will talk about the important results, the technical trade-offs of

our apparatus and assess the performance of our optical design. Later we will show our results, with illustrations of fluorescence imaging and Raman spectra. After demonstrating all aspects of our design on a large scale, a miniature probe will be proposed. Finally, suggestions will be made for future development of the probe.

REFERENCES CITED

[1] M. P. Golombek, "The Mars Pathfinder Mission," *Journal of Geophysical Research*, Vol. 102 No. E2, February 25, 1997, pp. 3953-3965.

[2] H. P. Klein, "The Search for Life on Mars: What we Learned from Viking," *Journal of Geophysical Research*, Vol. 103 No. E12, November 25, 1998, pp. 28463-28466.

[3] G. A. Soffen, "The Viking Project," *Journal of Geophysical Research*, Vol. 82, No. 28, September 30 1977, pp. 3959-3970.

[4] A. Brack, "Why exobiology on Mars?" *Planetary and Space Sciences*, Vol. 44, No. 11, 1996, pp. 1435-1440.

[5] A. Banin, R. Mancinelli, "Life on Mars? The chemical environment," *Journal of Advanced Space and Space Research*, Volume 15, 1995, pp. 163-170.

[6] D. C. Berman, W.K. Hartmann, "Recent Fluvial, Volcanic, and Tectonic Activity on the Cerberus Plains of Mars," *Icarus,* Volume 159, Issue 1, September, 2002, pp. 1-17.

[7] R. Mancinelli, "Accessing the Martian deep subsurface to search for life," *Journal of Planetary and Space Science*, Vol. 48, 2000, pp. 1035-1042.

[8] E. Grin, N. Cabrol, "Overview on the formation of paleolakes and ponds on Mars," *Journal of Global and Planetary Change*, Vol. 35, 2002, pp. 199-219.

[9] P. Coste, V. Gromov, S. Pinna, F. Angrilli, H. Kochan, L. Richter. "Development of the planetary underground tool subsurface soil sampler tool for the Mars Express Beagle2 Lander," *Journal of Advanced Space and Space Research, Vol. 28, No. 8, 2001, pp. 1225-1230.*

[10] S. Pinna, F. Angrilli, H. Kochan, L. Richter, "Development of the mobile penetrometer (MOLE) as sampling tool for the Beagle2 Lander on Mars Express 2003," *Journal of Advanced Space and Space Research*, Vol. 28, No. 8 , 2001, pp. 1231-1236.

[11] A. Ellery, C Welch, A Curley, D. L. Dickensheets, D. D. Wynn-Williams, H. G. M. Edwards, "Design options for a new European astrobiology focused Mars mission – Vanguard," *American Institute of Aeronautics and Astronautics*, Ellery et al. 2002.

[12] R. Mancinelli, "Planetary protection and the search for life beneath the surface of Mars," *Advanced Space Research*, Pergamon, Volume 31, Issue 1, 2003, pp. 103-107.

[13] G.A.Soffen "The Viking Project" *Journal of geophysical research*, volume 82, issue 28, September 1977, pp. 3959.

[14] D. D. Wynn-Williams, H. G. M. Edwards. "Antarctic Ecosystems as Models for Extraterrestrial Surface Habitats," *Planetary and Space Science*, Volume 48, 2000, pp.

REFERENCES CITED-CONTINUED

1065-1075.

[15] D. D. Wynn-Williams, H. G. M. Edwards. "Proximal Analysis of Regolith Habitats and Protective Biomolecules in Situ by Laser Raman Spectroscopy: Overview of Terrestrial Antarctic Habitats and Mars Analogs," *Icarus*, Volume 144, 2000, pp. 486-503.

[16] C. McKay, M.V. Ivanov, P. Boston, "On the possibility of Chemosynthetic Ecosystems in Subsurface habitats on Mars," *Icarus*, Volume 53, 1992, pp.300-308.

[17] G. Horneck. "The microbial world and the case of Mars," *Journal of Planetary and Space Sciences*, Volume 48, 2000, pp. 1053-1063.

[18] R. Tippkotter, "Staining of soil microorganisms and related materials with fluorochromes," Douglas Ed. *Soil Micromorphology: A basic and applied science*, Elsevier. 1990, pp 605-611.

[19] R. Riedel, D. Schlenk ,D. Frankl, B. Costa-Pierce, "Analyses of organic and inorganic contaminants," *Marine Pollution Bulletin,* Volume 44, Issue 5, May, 2002, pp. 403-411.

[20] M. W. Davidson, M. Abramowitz, "Fluorescence: Overview of Excitation and Emission Fundamentals", from <http://www.molecularexpressions.com/primer/lightandcolor/fluoroexcitation.html>, accessed October 25, 2003.

[21] M. W. Davidson, M. Abramowitz, "Fluorescence Microscopy: Basic Concepts in Fluorescence", from <http://www.molecularexpressions.com/primer/techniques/fluorescence/fluorescenceintro.html>, accessed September 25, 2003.

[22] From <http://nobelprize.org/physics/laureates/1930/index.html>, accessed March 25, 2003.

[23] D.S. Moore, "Determination of energetic materials in soils using multivariable analysis of Raman spectra," *Journal of Analytical Chemisty*, Volume 369, 2001, pp. 393-396.

[24] P. F. McMillan, and A. M. Hofmeister, "Infrared and Raman Spectroscopy," *Spectroscopic Methods in Mineralogy and Geology*, F. C. Hawthorne, Edr, Chelsea, Mineralogical Society of America, 1988, pp. 99-151.

[25] D. L. Dickensheets, D. D. Wynn-Williams, H. G. M. Edwards, C. Schoen, C. Crowder, E. M. Newton, "A Novel Miniature Confocal Microscope/Raman Spectrometer

REFERENCES CITED-CONTINUED

System for Biomolecular Analysis on Future Mars Missions after Antarctic Trials," Journal of Raman Spectroscopy, Vol. 31, 2000, pp. 633-635.

CHAPTER TWO

PENETROMETERS AND SENSING TECHNIQUES

Underground explorations represent many challenges, such as detecting, locating, and identifying elements in an inhospitable environment. To achieve this, there is a need for a real-time controllable sub-surface instrument. As we discussed before, looking for Martian bio-signatures would require robust and powerful infiltrating machines. These machines are also needed for monitoring industrial wastes such as fuels, petroleum oils, and solvents which can cause a serious threat to underground waters and ecosystems on earth. Deep infiltration below the surface is a direct and efficient method of sub-terrestrial soil characterization. This method can result in very convincing and relevant information about the soil composition. This chapter will talk about penetrometers and state of the art optical sensing techniques for soil characterization and, finally, propose a multifunctional optical probe that is penetrometer compatible.

Penetrometers

Cone penetrometers have been used for more than a decade, and their effectiveness has been widely proven. Their use was first concentrated in the fields of construction and agriculture and lately for sub-terrestrial explorations and environmental applications. Today a variety of penetrometers are available. These penetrometers come in different sizes and can host a variety of sensors depending on the application. These

penetrometers can be pushed more than 60 meters below the surface [1], with constant speeds in homogeneous soils. The distinction between these penetrometers lies in how the force is applied to them. The penetration can be achieved by electric motor drilling, by hydraulic pressure, or by mechanical hammering [1]. These types of penetrometers do not rely on constant velocities, and their depth increments will depend on the applied energy and the soil hardness. The weight and size of the probe and the cone angle will further influence its velocity. Rocks and other high density elements present serious obstacles to penetrometers, often impeding their performance.

Figure 2.1: Example penetrometer from Broke Ocean Technology, Limited after [2].

Recent advances in sensor technologies have expanded the utilization of cone penetrometers. With the growing human interest in exploration of under-ground resources, the call for more comprehensive and advanced probes increased. Commercial penetrometers can gather important information about soil, such as its humidity, density, salinity, and seismic properties. For example, modern penetrometers are equipped with tracking devices that help to localize the position of the instrument.

Penetrometers with electrical and electromagnetic sensors are used to measure the soil's electrical conductivity. Also, information about soil moisture can also be gathered by evaluating the change in dielectric constant (capacitance) or magnetic permeability (inductance) affected by the composition of tested soil.

Other penetrometers assess the hardness of the soil by measuring the force deployed by mechanical tools. The soil compaction is also measured by pneumatic sensors by assessing their ability to inject air into the soil.

Some penetrometers determine the soil composition, and its moisture, by measuring the time of travel of magnetic or acoustic waves [3]. Electrochemical sensors, such as ion-selective membranes, are also used by penetrometers. These membranes produce a voltage output in response to the interaction with selected ions (H+, K+, NO3−, Na+, etc.) [4]. Although these sensors have been extensively used in various geotechnical applications, their precision and accuracy depends strongly on their calibration.

Optical Sensing Methods

Various optical sensors can be used for underground explorations; however, some of these are not penetrometer compatible. Shocks coming from the hammering, pressure, and vibrations can pose serious problems to some sensors.

Numerous sensors are being tested for the detection of metals, radioactivity, explosives, and specific pollutants [5] [6] [7] [8] [9] [10] [11]. Many fluorescence-based sensors have been tested with penetrometers. UV-induced fluorescence spectroscopy was tested to detect the presence of petroleum hydrocarbons with the help of cone penetrometers [5] [6]. Most of these probes relied on one or many excitation wavelengths from a laser source and its harmonics or from mercury lamps with a grating. The chosen excitation wavelengths depended on the targeted elements.

Fluorescence life time is another effective sensing method. This technique induces fluorescence and measures the time spent between the excitation state and the ground state which is specific for each fluorescing molecular compound. The decay time is on the order of pico to nanoseconds and the measurements can be done either in the time or frequency domain [7]. The advantage of this method is that the fluorescence life time is independent of the specimen concentration, the photo-bleaching and the excitation light intensity [7].

Many other electromagnetic sources were used for underground explorations. X-ray fluorescence (XRF) penetrometers have been developed for the analysis of subsurface heavy metal contamination [8]. This methodology has proved to be effective in detecting elements higher than atomic number 20, including radioactive elements.

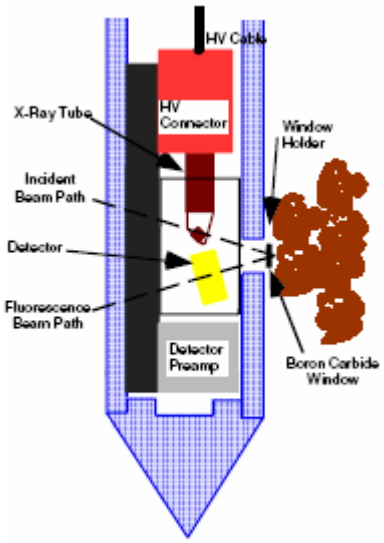

Figure 2.2: Schematic of the XRF penetrometer sensor after [9].

The detection of radioactive waste with gamma rays was also applied to penetrometers [9].

Laser breakdown spectroscopy is another sensing method that has been used with penetrometers. This method relies on a high irradiance infrared laser (above GW/cm^2) to generate a spark on a finite spot [10]. The resulting wavelengths present in the spark serve to delineate the heavy metals in soil. Furthermore, infrared based sensors were also used to trace hydrocarbon contaminants in water and soils based on their absorbance.

A Raman penetrometer probe has also been designed and tested by the U.S. Department of Energy [11] as a way of detecting subsurface toxic materials.

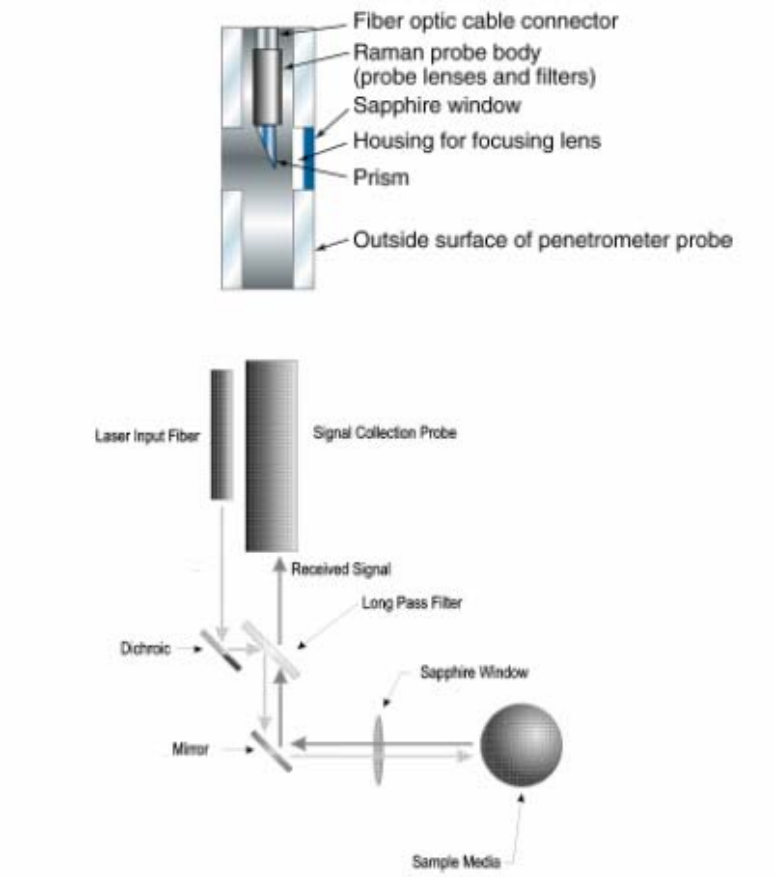

Figure 2.3: Published design illustrations of the Raman probe by the U.S. Department of Energy after [11].

The above drawings roughly illustrate their Raman Probe design; explicit details are not known at this time. Their design has been specifically used and tested in waste

storage tanks. With an excitation wavelength of 785nm, their design has proved to be successful especially for detecting nitrates and other dense non aqueous phase liquids (DNAPL).

In addition, Raman spectroscopy has been previously tested in our lab as a suitable means of detecting bio-signatures and some toxic elements [12]. A miniature Raman probe was built and tested under the supervision of Dr. D. Dickensheets. The probe has proved its capability for detecting organic matter and soil contaminants present on the surface. This thesis is a continuation of that previous work. The proposed design will modify this Raman sensor by adding imaging features to the probe and making it compatible with a penetrometer. These extra sensing techniques will increase the probe capabilities and result in better detection limits.

Multi-functional Probe

This thesis proposes a multifunctional probe that combines real-time and fluorescence imaging with Raman spectroscopy. The principal objective of this probe is to detect contaminants and bio-signatures in the subsurface environment.
Raman and fluorescence techniques have proven their effectiveness; however, not a single method can be used for discriminating between elements. Soil contains a multitude of fluorescing elements. For each element, there exists an optimal excitation wavelength that will give a maximum fluorescence signal. The fluorescence intensity can also tell us about the nature of the element and its concentration.

For example, heavy aromatic hydrocarbons fluoresce when excited with near UV light, while light aromatic hydrocarbons need far UV light to fluoresce. Meanwhile, aliphatic hydrocarbons have little fluorescence. However, their fluorescence properties change when mixed with solvents. Therefore, fluorescence methods cannot prove the presence of a specific hydrocarbon. Furthermore, fluorescence emission wavelengths can be affected by numerous environmental factors or by interaction with other materials or solutions. Hence, to be able to confirm the presence of an element more detection methods are needed. As discussed before, Raman sensing is a very powerful detection tool that gives a unique finger print for each element, helping to identify it, and making up for the inadequacies of fluorescence imaging.

In addition to the benefits of Raman and fluorescence sensing, we can further improve our knowledge of the specimen by adding reflected light imaging feature to the probe. Reflected light imaging will add many capabilities to the probe. Namely, it will help us distinguish the physical properties and the size distribution of elements in the picture and also assist us in observing their morphology. In situ imaging will give information about the soil texture, the soil type, and the grain size. This method will be extremely important to observe fossilized organic materials on the Martian subsurface.

The probe that we are proposing will be divided into three parts. The first section will house the LED circuitry. The electronics will sequentially activate and regulate the timing between various LEDs to switch between fluorescence and reflected light imaging. Another section will be reserved for the imaging electronics. Finally, a section of the probe will house all the optical elements for the Raman, fluorescence, and in-situ

imaging. The Raman signal will be excited by a laser located on a host platform. Optical fibers will route the excitation light to the probe and direct the Raman signal back to the spectrometer.

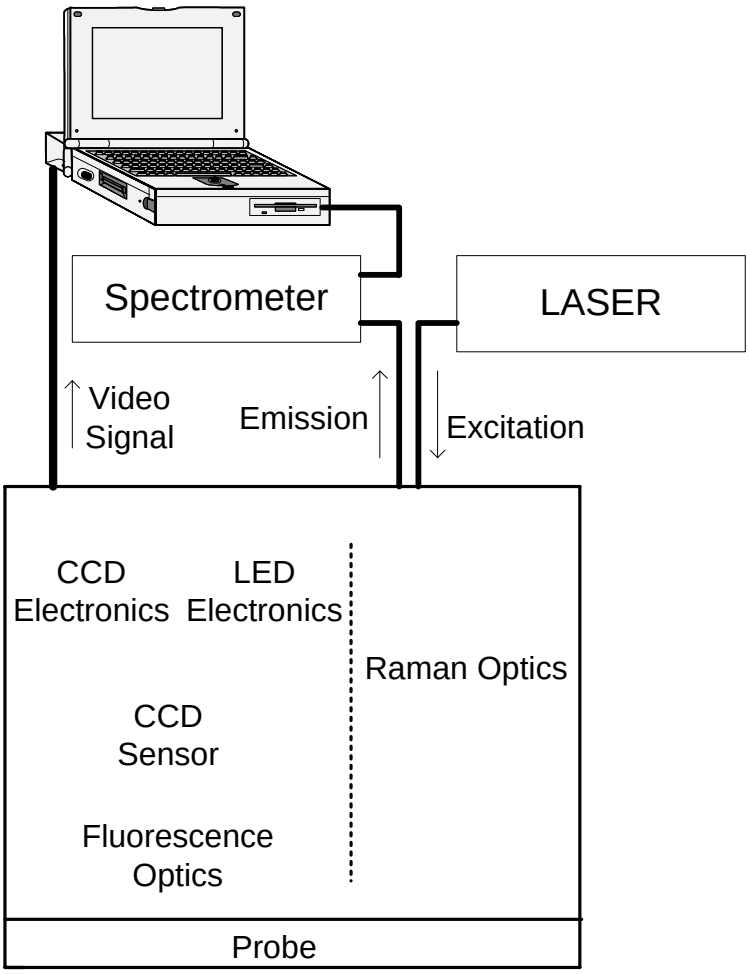

Figure 2.4: General scheme of the proposed probe.

Similarly, a video cable will be attached to the imaging electronics on the probe. It will transmit the fluorescence and color images to a computer through a frame grabber.

The optical elements in the probe will deliver LED light to the sample and focus the Raman excitation laser beam. The scattered visible light will be routed to the imaging sensor while the infrared Raman signal will be directed to the spectrometer. Color and

fluorescence images will give us optical information of all the elements in the field of view of the camera; while, Raman sampling will give a point measurement of a few microns.

Because of the stress and vibrations applied to the penetrometer, a fixed objective lens will be most suitable. Even with a fixed-focus objective lens, images could be obtained with a good depth of focus near a transmission window in the probe.

Penetrometry is a well established technique for the characterization of the subsurface environment. The combination of Raman, fluorescence sensing and real-time imaging will make the penetrometer an even greater and more capable tool for subsurface detection. The next chapter will talk about the optical requirements of our probe to achieve Raman detection, fluorescence, and color imaging.

REFERENCES CITED

[1] R. D. Lorenz, M. Bannister, P. M. Daniell, Z. Krysinski, M. R. Leese, R. J. Miller, G. Newton, P. Rabbetts, "An impact penetrometer for a landing spacecraft Measurement," *Science and Technology*, Volume 5, Issue 9, September 01, 1994, pp. 1033-1041.

[2] Brooke Ocean Technology Limited, 11-50 Thornhill Drive, Dartmouth, Nova Scotia, Canada B3B 1S1, Phone +1 902-468-2928 from
< http://www.brooke-ocean.com/ffcpt-01.html>, accessed Mars 5, 2003.

[3] U.S. EPA, "Field Methods for the Analysis Of
Petroleum Hydrocarbons," *Chapter 16*, March 1997, from
<http://www.epa.gov/swerust1/pubs/esa-ch6.pdf>, accessed May 3, 2003.

[4] K.A. Sudduth, S. T. Drummond, N.R. Kitchen, "Accuracy issues in electromagnetic induction sensing of soil electrical conductivity for precision agriculture," *Computers and Electronics in Agriculture*, Volume 31, Issue 3, May, 2001, pp. 239–264.

[5] S. H. Lieberman, "Direct-push, fluorescence-based sensor systems for in situ measurement of petroleum hydrocarbons in soils," *Field Analytical Chemistry & Technology*, Volume 2, Issue 2, 1998, pp. 63–73.

[6] M.L. Kram, A.A. Keller, S.M. Massick, et al. "Complex NAPL site characterization using fluorescence Part 1: Selection of excitation wavelength based on NAPL composition," *Soil and sediment contamination*, Volume 13, issue 2, 2004, pp. 103-118.

[7] M. Christenson, S. Sternberg, "Fluorescence lifetime imaging microscopy (FLIM) lets biologists study cellular processes," *OE magazine (SPIE),* January 2004, pp 28-30.

[8] B.J. McDonald, C.W. Unsell, W.T. Elam, K.R. Hudson, J.W. Adams, "A cone penetrometer X-ray fluorescence tool for the analysis of subsurface heavy metal contamination," *Nuclear Instruments and Methods in Physics Research*, Section A: Accelerators, Spectrometers, Detectors and Associated Equipment, Volume 422, Issue 1-3, February 11, 1999, pp. 805-808.

[9] J.C. Morgan, J.W. Adams, J.H. Ballard "Field use of a cone penetrometer gamma probe for radioactive-waste detection," *Field analytical chemistry and technology*, volume 2, issue 2, 1998, pp. 111-115.

[10] A. Theriault, S. Bodensteiner, K. Scott, H. Lieberman, "A real-time fiber-optic LIBS probe for the in situ delineation of metals in soils," *Field Analytical Chemistry & Technology*, Volume 2, Issue 2, 1998, pp. 117-125.

[11] K. R. Kyle, E. S. Weeks, J. Bello, S. B. Brown, U.S. Department of Energy, "Raman Probe", *Innovative technology*, Prepared for U.S. Department of Energy, July 1999, from <http://web.em.doe.gov/doclistb.html>, accessed April 10, 2003.

REFERENCES CITED-CONTINUED

[12] D. M. Crowder, “A confocal microscope and Raman spectroscopy probe for Mars exploration”. Master’s Thesis, Montana State University, April 2002.

CHAPTER THREE

TABLETOP EXPERIMENTAL SETUP

Before designing the probe, tests were conducted in the lab using a large-scale version of the instrument. These experiments were done to simulate the conditions for the miniature probe, which will be introduced later. In this chapter, we will talk about the experimental apparatus and the optical design for fluorescence experiments. The discussion will address all the important optical criteria that are essential for the success of Raman detection, fluorescence, and color imaging.

Our research has the following objectives: to generate high-quality real-time images, to ensure efficient light collection for the Raman and fluorescence signal, and to combine the design in a small and efficient probe. As we discussed before, the Raman laser and the spectrometer will be remote from the probe. The probe will be composed of filters to separate Raman and fluorescence signals and an imaging sensor will be used within the probe for fluorescence and real-time imaging. Finally, LEDs will be incorporated in the probe to induce fluorescence and generate illumination for color imaging. Only the optical characteristics will be discussed in this chapter, while the next chapter will assess the requirements of the imaging sensor.

Fluorescence and Color Imaging with LEDs

What distinguishes our design is the use of LEDs for inducing fluorescence. Typically, fluorescence excitation is achieved with intense light sources such as lasers, laser diodes, and Mercury or Xenon lamps. These light sources have a very broad coverage of visible and invisible light, which can excite numerous fluorescing specimens. These powerful light sources have the advantage of producing a high flux of photons, which is of great use especially when the fluorophore has low quantum efficiency. For imaging, the use of incoherent light such as Xenon or Mercury lamps or LEDs has the advantage of eliminating speckles and can results in modestly higher spatial resolution.

The emission spectrum of Mercury or Xenon lamps is unevenly spread between the UV and the Infrared. Mercury and Xenon lamps are ideal for lab experiments; however, they present some disadvantages for remote applications. In fact, these expensive lamps are quite big, hot, and energy consumptive (50 to 150 Watts). Moreover, the lifetime of Mercury and Xenon lamps is only around 200 hours. These lamps cannot be turned on and off for short periods of time, which is inconvenient for fast switching between fluorescence and real time imaging of soil. Due to reasons of portability and power consumption, ultra-bright light emitting diodes will be more adequate for our needs.

The LED choice became possible because of the advances in research in semiconductor materials in the past few years. Currently, ultra-bright LEDs with thousands of millicandelas became available at a very low price. These LEDs are robust, bright (optical power of 30mW), have a lifetime of more than 100,000 hours, and are very easy to replace. LEDs are the most energy efficient means for producing narrow-

band light. Currently, LEDs generate enough light to excite fluorescence. LEDs' external quantum efficiency has attained high performances such as 60 to 70 % for the visible and 32 % for the UV LEDs [1]. Today, LED wavelengths cover all the visible spectrum and parts of the ultraviolet and infrared. Research is being conducted to get more peak wavelengths in the far UV, which will make the LED a more powerful excitation source for detecting fluorescing elements. Because LEDs have a narrow spectrum compared to Xenon and Mercury lamps, the use of a band pass filter is sometimes unnecessary. LED-based microscopes have been increasingly present in the past years. LED induced fluorescence has been used in the medical field for capillary and skin examinations, for the diagnosis of tumors and for the detection of proteins and enzymes [2][3][4][5]. The introduction of LEDs has made the conception of low volume and portable fluorescence sensors possible. These factors make the LED a viable tool for future Martian explorations.

Illumination for In-Situ Imaging

Figure 3.1 illustrates the conditions in which the fluorescence and reflected light imaging was done. As illustrated the figure, the reflected light illumination may be provided as either brightfield or darkfield illumination. These two illumination approaches are quite different and the use of both will reveal more details of the specimen.

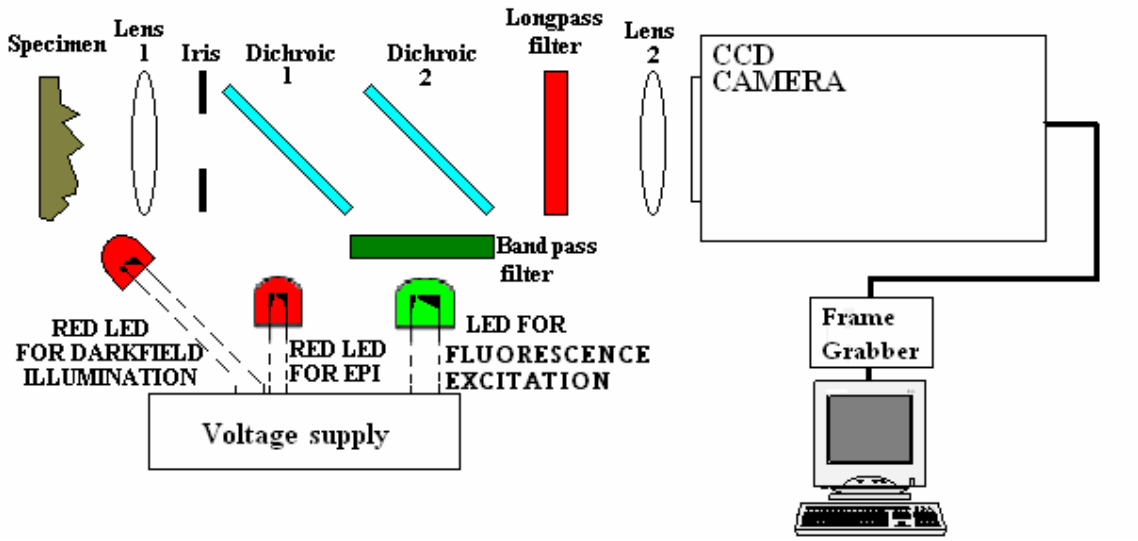

Figure 3.1: Experimental apparatus used for fluorescence and reflected light imaging.

Darkfield illumination, also known as oblique illumination, produces more contrast which provides better details of the object, making shapes easier to distinguish. This type of illumination is very advantageous for imaging rough surfaces such as soil. In brightfield (epi-illumination), the excitation light is parallel to the optical axis. This way the objective lens will collect direct reflections from the sample, which will make brighter images. In Epi-illumination, the collection of Rayleigh scattering is more efficient. Also, the fluorescence imaging will be done with epi-illumination, as it proves to be the most effective for detecting fluorescence. Since fluorescence emission is omni-directional, epi-illumination remains the best only if it delivers more excitation light to the sample. This will depend on the efficiency of the dichroic and other optical elements, but epi-illumination is generally best because the objective lens provides a concentration of the illumination at the sample.

The next illustrations (figure 3.2 and 3.3) give a visual comparison between the two types of illumination for reflected light imaging. These pictures were taken with the same diode current, and without changing the depth of focus.

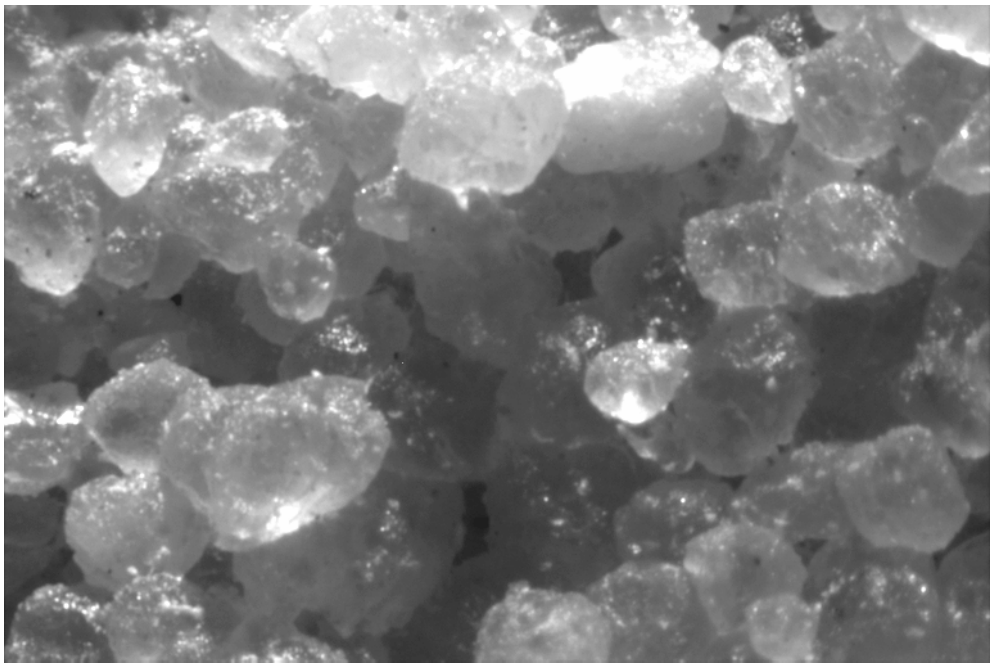

Figure 3.2: Darkfield image of soil with a field of view of 4.85 mm by 3.23 mm.

Figure 3.2 gives an example of darkfield soil imaging. As seen, darkfield images allow more contrast and give a three dimensional view of the sample. Figure 3.3 shows the epi-illumination image of the same spot. As we can see, epi-illumination demonstrates higher brightness, even illumination of the sample, but lower contrast.

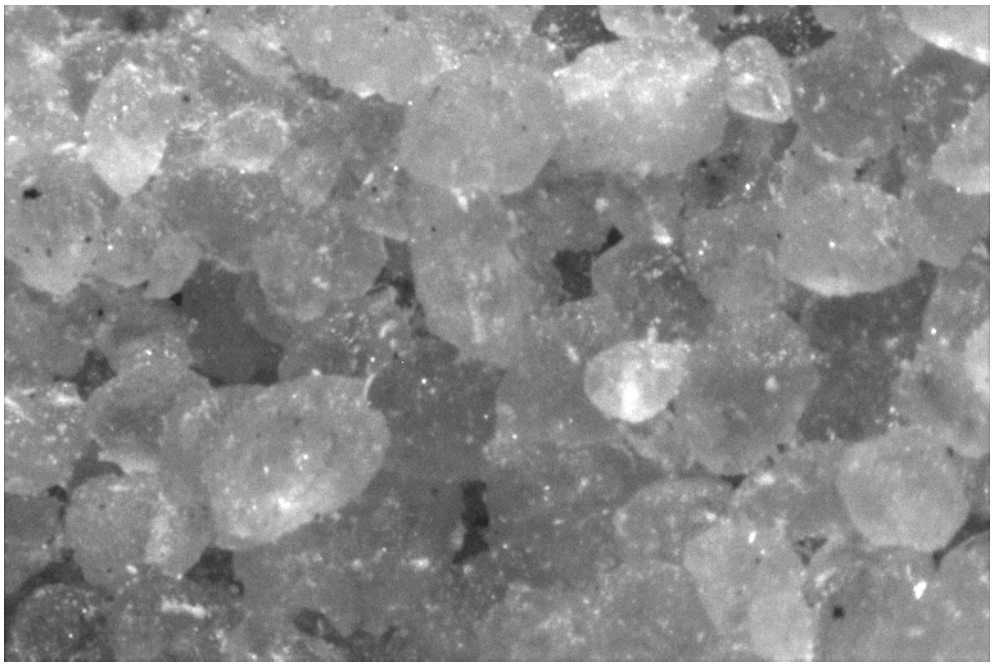

Figure 3.3: Brightfield image of soil with a field of view of 4.85 mm by 3.23 mm.

The epi-illumination gives a more planar view and an even illumination of the sample; however, the shape of the rocks is less perceptible. Employing both illumination schemes will give us a better visual description and understanding of the underground environment.

Optical Criteria

Soil presents many differences in structure, color, and texture. Numerous optical factors should be considered to gather all these important details. In the following paragraphs, we will discuss the important elements along the optical path and discuss their specifics. For reflected light and fluorescence microscopy, the optical system should image the sample onto the CCD detector. Two achromatic lenses were used for fluorescence imaging. Achromats were used because they offer better focusing capabilities for a good portion of the visible wavelengths. Because the refractive index of

the lens differs with the incident wavelength, single lens elements suffer from chromatic aberration. In fluorescence, the stoke's shift can be as high as 200 nm. Hence, without achromats short wavelengths will have a shorter focal length than long wavelengths. Moreover, achromats give a better monochromatic performance. Their use results in a tighter focus and creates a high fidelity image.

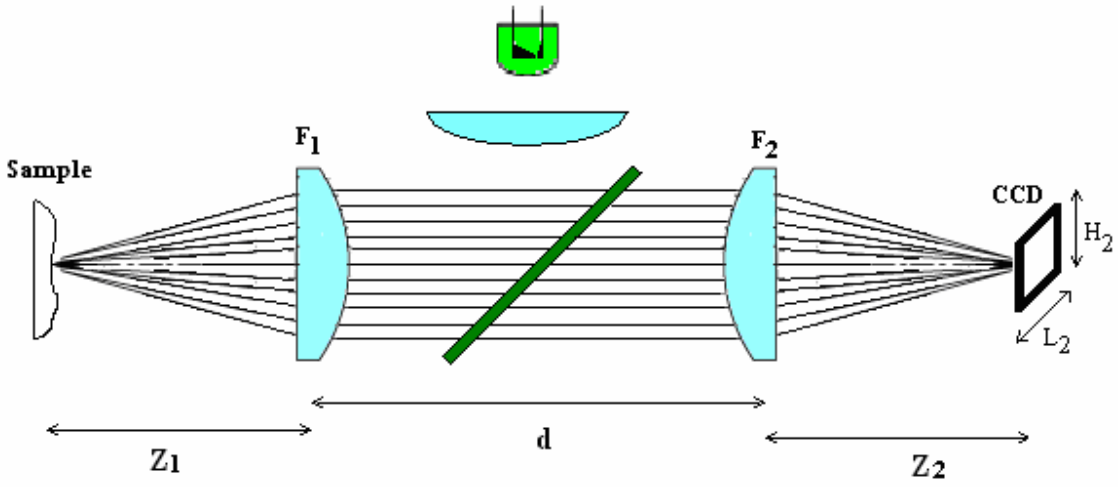

Figure 3.4: Image and object conjugates for the imaging optics.

Our optical system had a magnification M as described by the following equation, where H_2 and H_1 represent the image and object size respectively.

$$M = \frac{-Z_2}{Z_1} = \frac{-F_2}{F_1} = \frac{H_2}{H_1}. \quad (3.1)$$

The objective lens used in the table-top experiment had a focal length of 30 mm, while the image lens had a focal length of 50mm. For the same set of lenses and the same magnification M, the ratio of the sensor size (H_2 x L_2) to the field of view (H_1 x L_1) was equal to the magnification squared. Different image sensors, with different dimensions, were tested with this setup. A smaller imaging sensor will be proposed for the miniature probe, and the choice of lenses will depend on the size of the image sensor.

Magnification is needed for a better analysis of soil particles, however too much magnification reduces the effective field of view. For our setup a magnification of 1.67 was chosen, which was adequate for imaging our samples. In general, the desired magnification will depend on the size of the sample and, on the nature of the target. A high magnification is needed for observing specimens with small fluorescing particles such as individual bacteria, while a low magnification is preferred to image full grains of soil and sample a larger area.

The choice of lenses is very important for the success of the fluorescence imaging. Lenses are characterized by the numerical aperture (NA), which depends on the focal length f and, the diameter D of the lens as follows:

$$NA = \sin\left[\arctan\left(\frac{1}{2\ f\ /\#}\right)\right] \quad (3.2)$$

$$f\ /\# = \frac{f}{D} \quad (3.3)$$

The numerical aperture characterizes the ability of a lens to gather light. Therefore, the bigger is the aperture and the larger is the amount of light that can be captured. Since fluorescence light is usually very weak, maximizing the NA is in our advantage. For our optical system we used an NA of 0.38 for the objective lens.

The f-number of a lens determines three important factors: the depth of field, the brightness of the image and the resolution of the lens. Having a high NA is sometimes inconvenient because it can result in high brightness of the image, which can cause pixel saturation. Saturated pixel charge can overflow to the adjacent pixels and cause blooming. This problem is more specific to the charged coupled device (CCD), and is resolved by adjusting the LED light intensity.

To get good images of soil we need to bring various elements of the picture into focus by increasing the depth of field. The depth of focus determines a distance range in which all details will appear with a good resolution and with minimal blur. As described by the following equation, diffraction and the geometric defocus are the factors that dictate the limit for the depth of field [6],

$$D = \frac{\lambda\, n}{NA^2} + \frac{n}{M\ NA}\, p \quad (3.4)$$

, where n is the index of refraction and p the pixel size.

The depth of field *D* is inversely proportional to the NA of the objective lens; and, sensors with large pixel area result in higher depth of field at the expense of lateral resolution. To have direct control of the depth of focus, we have decided to place an iris in the light trajectory. The iris will dictate the size of the numerical aperture of the objective lens, and will therefore control the depth of focus of the image. Hence, an objective with a high NA will collect more light but will provide a smaller depth of focus. For the final design, this iris needs to be automatic and fully opened for fluorescence imaging and reduced for reflected light imaging to improve depth of focus.

One other important factor that depends on the NA is the diffraction limited resolution R. A small resolution will let us distinguish between very small elements in the picture.

$$R \approx \frac{\lambda}{2.NA} \quad (3.5)$$

The diffraction limited resolution does not depend on the magnification. If the geometric projection of the sensor pixels on the sample are larger than R, then the resolution will be determined by $\frac{p}{M}$. Because these tradeoffs are crucial to the success of

the application, the objective NA must be chosen carefully. Even with a moderate objective NA of 0.38, the resulting images gave good imaging performance. The iris placed at a distance of 5 cm behind the objective lens, helped changing the effective NA of our system. This gave us the opportunity to experiment with the limits and assess the importance of the numerical aperture. Consequently, for the final design we will be aiming for an objective NA higher than 0.5.

	Iris diameter	Effective NA	Magnification	Geometric Resolution	Diffractive Resolution at 600 nm	Depth of field at 600 nm
Fluorescence	12 mm	0.58	1.67	7 μm	0.5 μm	47 μm
Reflected light	2mm	0.12	1.67	7 μm	2.5 μm	765 μm

Table 3.1: Optical values used in our system with a CCD pixel of 11.8x13.6 μm for fluorescence and reflected light imaging.

Fluorescence Optical Filters

As discussed in the introduction, the primary fluorescence of many organic and biological materials can be excited with blue-green light; whereas, the primary fluorescence of the aromatic molecules can be excited with near UV light. Based on this, we selected UV and bluish green LEDs, with their corresponding longpass filters. In fluorescence detection, the choice of filters is critical for suppressing all the undesired wavelengths. The success of the probe will depend on the proper choice of LEDs, and on the filters' performance. The optical characteristics of the filters were chosen based on the LED spectra. The longpass filter has to ensure an absolute blocking of the excitation light and transmit only the fluorescence light with minimal attenuation.

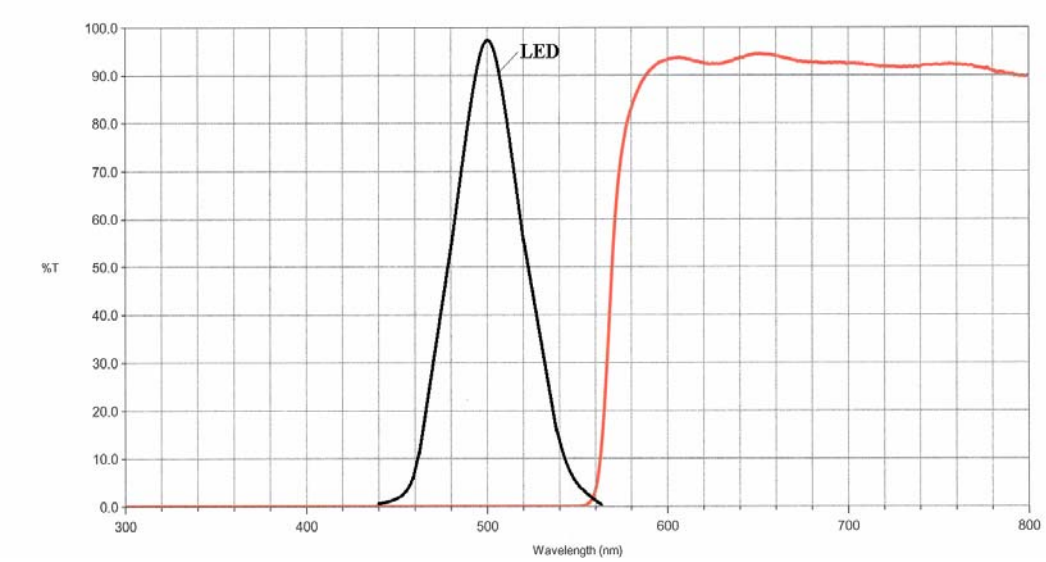

Figure 3.5: Longpass filter for green/blue fluorescence excitation with the approximate LED spectrum. (LED#1052 from B.G. Micro, Filter #E570lpv2 Chroma Technologies, Inc).

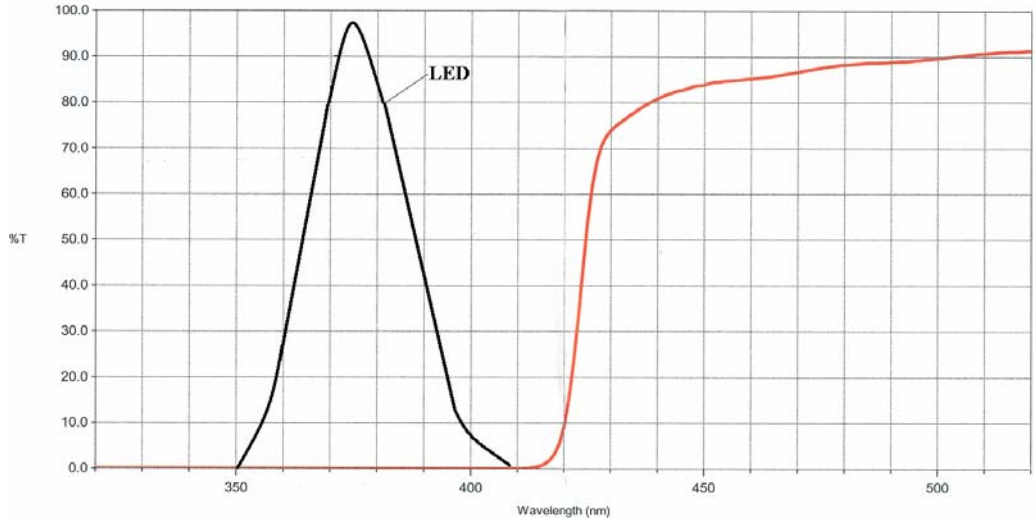

Figure 3.6: Longpass filter for the UV fluorescence excitation with the approximate spectrum of the LED. (LED#BP200CUV750-250 from LEDTRONICS, Filter # E570lpv2 Chroma Technologies, Inc.).

In addition to the LEDs and filters, fluorescing and non-fluorescing beads were purchased. These beads will allow us to test the efficiency of the filters. The excitation and emission wavelengths of the fluorescing beads were selected to match the LED and filter spectra. The testing procedure and the imaging results with these beads will be

presented in chapter five. Our filters were also tested with our camera setup, on the optical spectrum analyzer and on the microscope. Unexpectedly, when illuminated with bluish-green LED light, the Rayleigh scattering from non-fluorescing beads was discernible through the long-pass filter. Hence, we decided to measure the LED spectra with an optical spectrum analyzer. Surprisingly, the spectral width of the LED was found to be larger than we thought, causing an overlap with the spectrum of the long-pass filter. Unfortunately, the sensing range of our optical spectrum analyzer did not cover the UV wavelengths. Therefore, only the manufacturer's spectrum of the UV LED is presented.

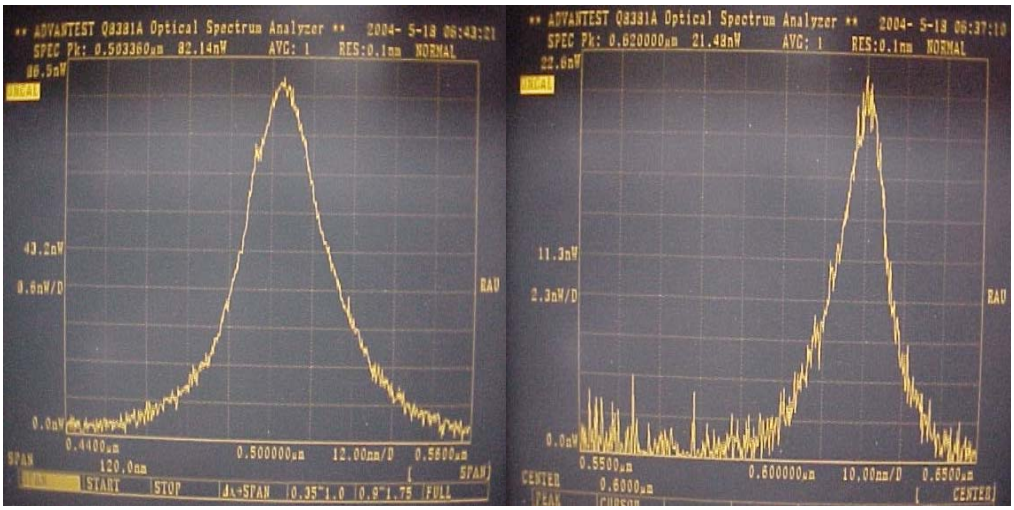

Figure 3.7: Spectral width of the green and red LED. The scale of the right spectrum is 10 nm per division while the left one is 12 nm per division.

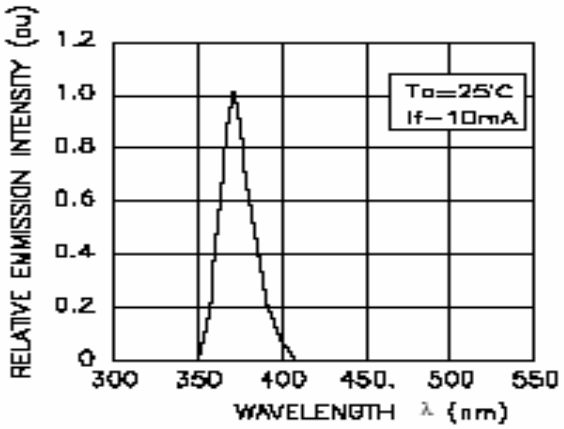

Figure 3.8: Spectral width of the UV LED from the manufacturer data sheet (BP200CUV750-250 from LEDTRONICS).

The optical spectrum of the LED stretched for more than 60 nm causing an overlap with the long pass filter. Hence, band pass filters where needed to suppress any overlap and make sure that no excitation light goes through the longpass filter.

Figure 3.9 shows the spectra of band-pass filters that were also purchased from Chroma technologies Inc. They were chosen to have a maximum transmission for the peak wavelength of our bright LEDs.

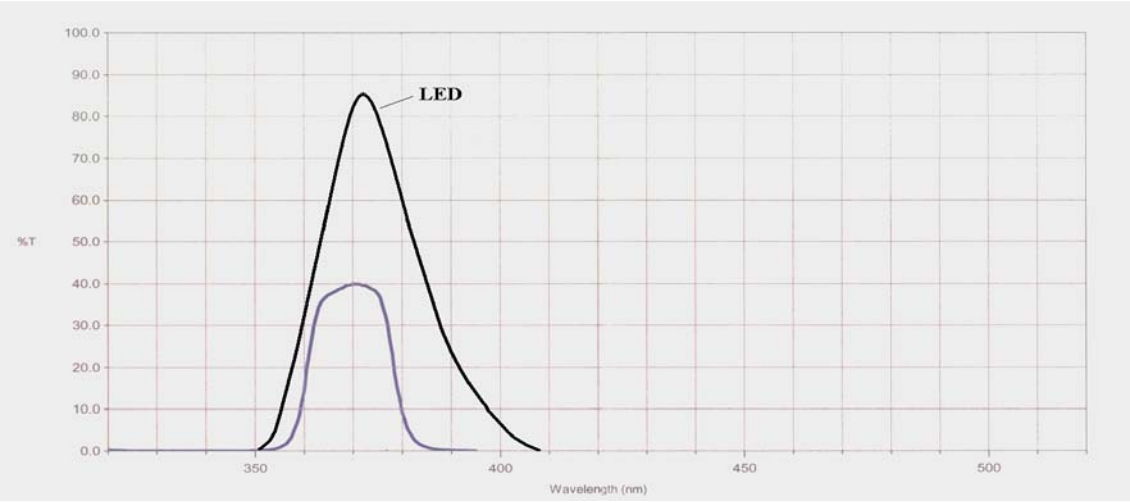

Figure 3.9: Bandpass filter D370/20 from Chroma Technologies, Inc. used for the UV LED centered at 370 nm with 20 nm of FWHM.

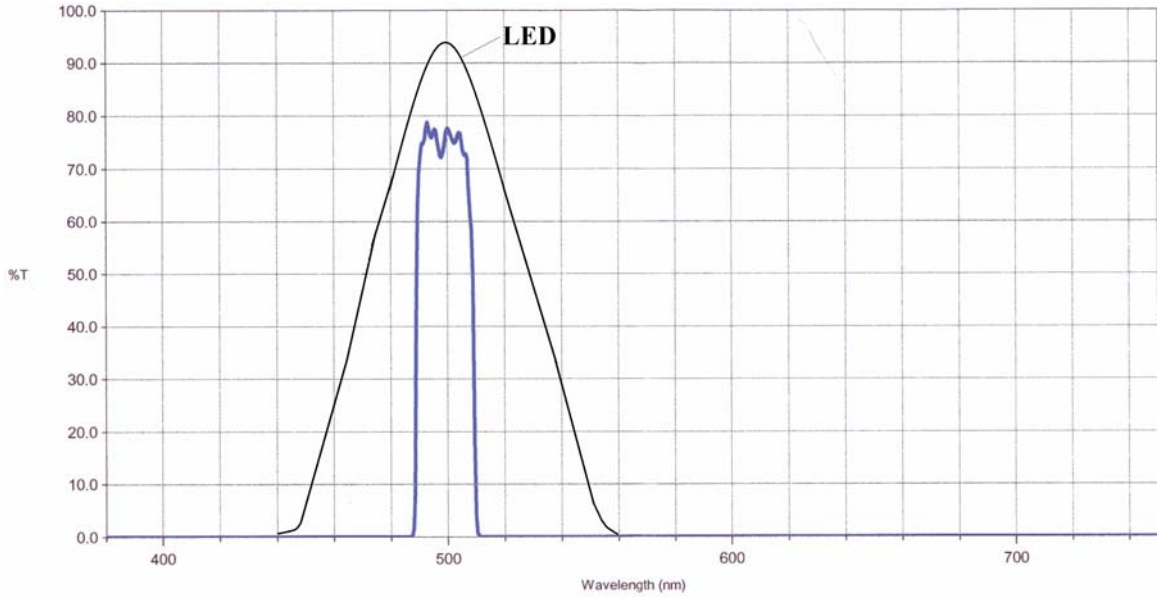

Figure 3.10: Bandpass filter E500/20 from Chroma Technologies, Inc. used for the bluish green LED centered at 500 nm with 20 nm FWHM.

We were not quite satisfied with the filter transmission, especially the UV bandpass that could only transmit 40% of the LED light. Still, this filter has proved its capability and good performance. However, for better LED power utilization, a filter with lower reflection should be incorporated into the final probe. In conclusion, the fluorescing and non-fluorescing beads and the optical spectrum analyzer confirmed the proper working of our filters.

Light Emitting Diodes

Our LEDs were chosen based on their color, their spectral width, their angular distribution, and their luminous intensity. LEDs exist under two main configurations: the surface emitting LED and the edge emitting LED. Surface emitting diodes have a large emitting area with almost Lambertian radiation and have higher output power than edge

emitting LEDs. The radiation pattern of the LED depends on the epoxy lens shape that covers it. LEDs with parabolic or hemispherical shaped epoxy lenses have a narrow angular spread; whereas, planar epoxy lens have a larger one. For our experiments our LEDs were driven with a moderate current well below the saturation region. In this region, LEDs did exhibit a linear relationship between the optical output and the forward current.

We measured optical power using an optical power meter (OPM, Newport 1830-C) with 6mm detecting aperture placed in contact with the LED. The results are presented in figures 3.11, 3.12 and 3.13.

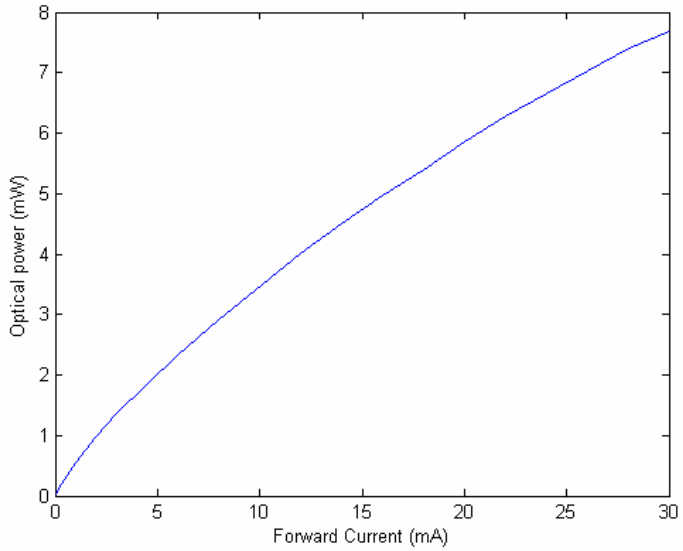

Figure 3.11: Output optical power versus forward current for the bluish-green LED.

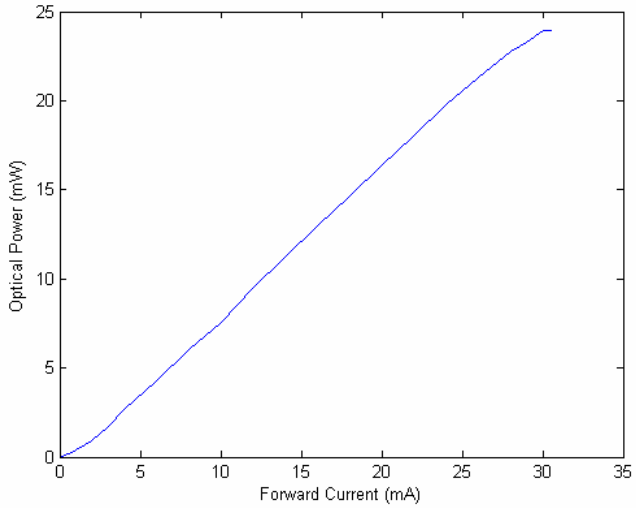

Figure 3.12: Output optical power versus forward current for the red LED.

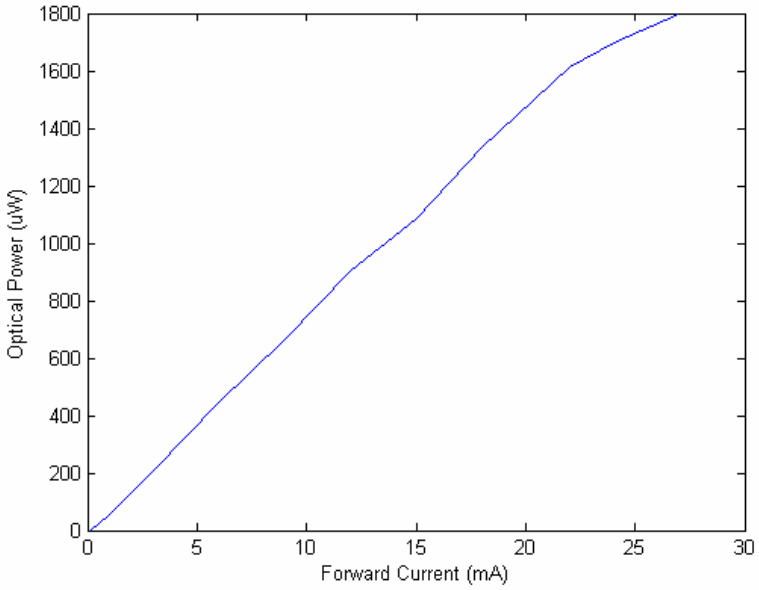

Figure 3.13: Output optical power versus forward current for the UV LED.

Because our LEDs had narrow emission angles, most of their radiation was collected by the OPM. The viewing angle is defined as the full angle at which brightness is half of the

central peak. In our case, the viewing angle of the LED was chosen between 10 and 15 degrees; which was needed to maximize the irradiance on our samples.

The wall plug efficiency was about 16% for the red LED, 12 % for the bluish green LED and 10% for the UV LED. LEDs with higher quantum efficiency are available on the market, but our LEDs were capable enough to induce fluorescence and provided sufficient light flux. The fluorescence signal is be proportional to the LED irradiance. In chapter five, the fluorescence yield will be estimated for various fluorescing samples based on the imaging sensor sensitivity. From these results, we will choose a fixed forward current to run each LED.

For 10 mW of LED light, the light budget estimation of our fluorescence optical system will be $3.8x10^6$ x η photon per pixel per second for the bluish-green excitation and $3.2x10^6$ x η photon per pixel per second for the UV excitation. This estimation comprises the transmission efficiency of our filters and lenses. These numbers will further be attenuated by the fluorescence efficiency η of the targeted sample.

	UV Longpass	UV Bandpass	Bluish- green Longpass	Bluish-green Bandpass	Lenses
% Transmission	85% at 450 nm	40% at 370 nm	93% at 600 nm	76% at 500 nm	$\approx(96\%)^8$

Table 3.2: Transmission values of some elements in the optical path.

Furthermore, LEDs did show some temperature dependency that affected their peak wavelength and their internal quantum efficiency. These variations will be explored later.

The performance of our system can also be enhanced by improving the spot size illumination. The illuminated spot in the sample should be big enough to cover all the field of view imaged by the sensor. For better reflected light images and complete fluorescence detection, the illumination of our target should be uniform on all the elements in the picture. The next chapters will show the results of our optimized design and demonstrate these concepts in greater detail.

The Raman Spectrometry Optical Design

Although both sensing techniques will share the same objective lens, the optical requirements for the fluorescence imaging are quite different from the Raman optics. For the Raman sensing, we want to obtain an image of the sample that shows the laser spot. This way the user will find the targeted Raman sample region in the image.

In the field, the Raman signal will be generated by a laser on a host platform. The laser beam will be carried by an optical fiber to the miniature probe. The excitation beam will pick up some Raman scatter within the fiber, which will interfere with the Raman signal of the sample. To suppress that light, a bandpass filter will be used to clean up the Raman excitation signal.

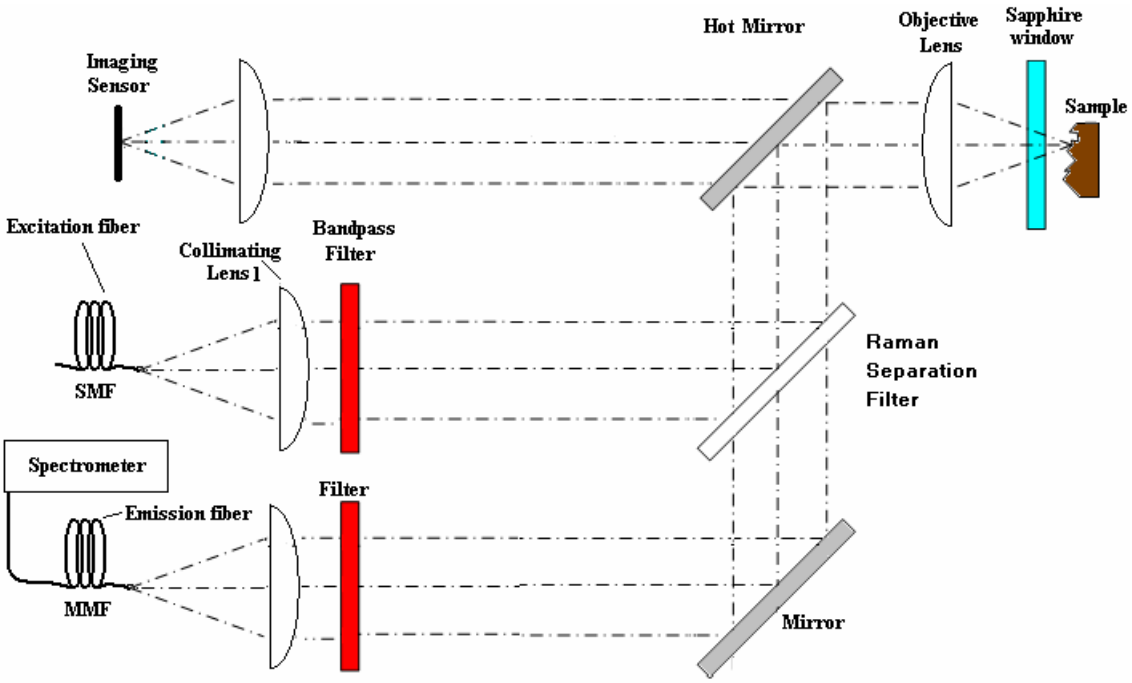

Figure 3.14: Raman detection apparatus.

The numerical aperture of the collimating lens will be chosen to match the numerical aperture of the excitation fiber. In the scheme shown in figure 3.14 a plano-convex lens is used for collimating the incoming laser beam. A quarter pitch graded-index or GRIN lens can be used instead to replace that lens.

Because the intensity of the Raman signal is inversely proportional to the fourth power of the excitation wavelength, it is more advantageous to use shorter excitation wavelengths. However, excitation wavelengths in the UV or visible can also induce the primary fluorescence of the specimen. The fluorescence signal is many orders of magnitude higher than the Raman signal, and can easily overwhelm it. For Raman spectroscopy, the fluorescence signal can be avoided by using longer-wavelengths in the near-infrared. Based on that, a near infra-red laser light would be the most appropriate to

excite Raman signal. Signal attenuations will be negligible for moderate depth measurements, especially if fiber bending is avoided.

The Raman spot will be visible if the chosen excitation wavelength is within the sensitive region of the imaging sensor. We will use a near infrared excitation wavelength of 1064 nm or below satisfying this requirement of silicon sensors. The use of achromats to reduce the chromatic aberration will be unnecessary, provided that the collection fiber core will be large enough to gather all incoming wavelengths. The 45 degree Raman separation mirror serves as a low pass filter; it will reflect the Raman excitation light and pass the emitted Raman light. Another bandpass filter will be used to remove the remaining excitation laser signal from the Raman signal.

The full NA of the objective lens is preserved for Raman collection to maximize light sensitivity, and the MMF fiber NA is high enough to accept all the collected NA.

In the next chapters, the capability of fluorescence detection will be tested. The results of these optical setups will be presented and discussed.

REFERENCES CITED

[1] K. Tadatomo, H. Okagawa, Y. Ohuchi, T. Tsunekawa, H. Kudo, Y. Sudo, " High Output Power Near-Ultraviolet and Violet Light-Emitting Diodes Fabricated on Patterned Sapphire Substrates Using Metalorganic Vapor Phase Epitaxy," *Journal of Light & Visual Environment*, Volume 27, Issue 3, December 2003, pp.140-145.

[2] G. Hilger, A. Ingrid, K. Leistner, N. Yvonne, A. Berndt, L. Alexander "Near-infrared fluorescence imaging of HER-2 protein over-expression in tumor cells," *European Radiology*, Volume 14, Issue 6, June, 2004, pp. 1124–1129.

[3] S. Hillebrand, J. R. Schoffen, M. Mandaji, C. Termignoni, et. al, "Performance of an ultraviolet light-emitting diode-induced fluorescence detector in capillary electrophoresis," *Electrophoresis*, Volume 23, Issue 15, No. 15, August 2002, pp. 2445 – 2448.

[4] K. Van Den Berg, A.W. Petra, L. Widengren, K. Jerker, A. Mark, "Fluorescence correlation spectroscopy of flavins and flavoenzymes: photochemical and photophysical aspects," *Spectrochimica Acta, Part A: Molecular and Biomolecular Spectroscopy*, Volume 57, Issue 11, September 2001, pp. 2135–2144.

[5] A. Delgado, S. Stolik, L. Anasagasti, **"**Feasibility of UV and Blue LEDs for Skin Lesions Fluorescence Diagnosis," *AIP Conference Proceedings*, Volume 724, Issue 1, September 2004, pp. 63-65.

[6] S.Inoué, R Microscopes, In *Handbook of Optics*, Vol III, 2nd Ed. Bass, M., Ed.; Mc Graw Hill; 1995.

CHAPTER FOUR

IMAGING HARDWARE

The choice of the appropriate imaging device is one of the key elements for the success of fluorescence detection. Today, most electronic imaging systems depend on two different technologies: the CMOS (Complementary Metal Oxide Silicon) and CCD (Charged coupled Device). Since their invention, these two chips have reached a high level of perfection. Even though the CCD has been the dominant technology in the past decades, CMOS has taken the lead in some specific areas. This chapter will first introduce these two types of sensors and then compare their performance. The performance will be judged mainly on noise issues. Based on noise performance, this chapter will also assess the need for cooling the image sensor.

The Charged Coupled Device or CCD

The concept of the CCD imager was born in 1970 in Bell Laboratories as a result of the research conducted by W. Boyle and G. Smith [1]. Since then, this detector has reached a high level of perfection and its use become very broad, from scientific use to popular distraction. Essentially, the CCD converts the light energy in photons to an electrical energy in electrons. The CCD technology is based on a rectangular array of metal oxide semiconductor capacitors or pixels. The energy of the incident photons can make electrons in the semiconductor go from the valence band to the conduction band

where they are free to move. The gathering of electrons takes place under the positively charged gate of each pixel. After a chosen exposure time, the charge is shifted around and the readout starts. The shifting of electrons is done by a sequential control of adjacent gate voltages that make the electrons move towards the most positively charged gate. Hence, the charge is transported vertically and horizontally to a node where the electron-to-charge conversion and amplification take place.

CCD Architectures

The readout procedure directly affects the CCD speed and depends on the CCD architecture that dictates the way the charge is transferred between the pixels. Currently, there are three types of CCD architectures: the full frame CCD, the frame transfer CCD, and the interline transfer CCD. The full frame CCD design was the first to be made and has the simplest architecture. The classical full-frame CCD design employs a single register in which all charges are transferred successively. To control the exposure and block light during the readout a mechanical shutter is used. This method results in a high quantum efficiency (QE) and resolution, but long read-out periods. One of the cameras used for our experiments was the Sensys from Roper Scientific Inc. This cooled camera is equipped with a Kodak Kaf-0401E full transfer CCD [2].

The second type of architecture is the frame-transfer CCD. In the frame-transfer architecture, the CCD is divided into two distinct areas: the image array, where the image is captured, and the storage array (not exposed to light), where the image is temporarily stored prior to the readout. This design allows a continuous readout and eliminates the

use of the shutter. Finally comes the Interline transfer CCD, which we also used in our experiments with the JAI CV-M300 camera equipped with a Sony ICX422AL CCD [3]. In the interline transfer CCD, one column of pixels collects light charge and transfers it to the next column that serves as a register. The register readout then proceeds in normal CCD fashion. The interline transfer CCD reveals a low resolution and a poor photosensitivity because a large portion of the CCD serves as a register and does not collect light. Currently, this type of CCD architecture now uses an array of micro lenses that focus the light to the sensitive part of the pixel. The JAI interline camera does not use micro lenses array. Even though the interline transfer CCD suffers from a moderate fill factor and low quantum efficiency, this type of architecture is very efficient time-wise and can allow very high frame rates. The choice of the appropriate CCD architecture will depend on the application and objectives. For low light detection and for the same pixel area, the full frame CCD architecture will have the best quantum yield [4].

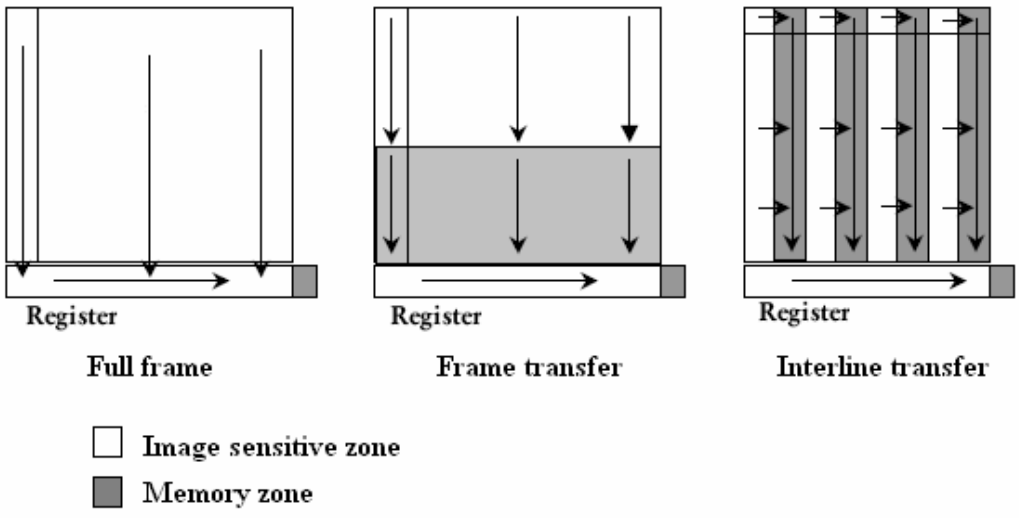

Figure 4.1: CCD architectures.

In these previously cited architectures, the gate is present on the top of the substrate, blocking some photons from reaching the pixel and, therefore, reducing the quantum efficiency. To remediate that, the back illuminated CCD was introduced. This CCD is mounted upside down on the camera with a much thinner substrate. This way, there is no obstacle between the photons and the substrate. So far, the back illuminated CCD has proved to be the most ideal for capturing low light [5]. We did investigate the back-illuminated sensors, and our light budget did not demand this ultimate level of sensitivity.

CCD Versus CMOS

Both CCD and CMOS image sensors are made of similar semiconductor materials, which make them have a comparable sensitivity in the visible light and the near IR. Moreover, both sensors rely on a pixels organization. The procedure is the same for both sensors; first, a photon-to-electron conversion takes place, followed by an electron-to-voltage conversion; the resulting voltage is then amplified and digitalized. However, the differences in CCD and CMOS architectures and circuit integration make these chips dissimilar in capability and performance. The main advantage of CMOS is the high level of electronics integration within the pixel. This contribution can make CMOS cameras smaller than CCD cameras. In fact, the detection, the charge-to-voltage conversion and amplification are all done at the pixel. CMOS offers direct and faster accessibility to each pixel and prevents blooming. In fact, CMOS can access any pixel or region of interest arbitrarily like a photosensitive DRAM. Concerning power

consumption, CMOS is more advantageous, as it consumes only 20-50 milliWatts compared to 1.5-5 Watts for the CCD [6].

Because each CMOS pixel has its own amplifier, and because of wafer irregularities, images taken with CMOS cameras lack uniformity. Therefore, the response of different pixels under the same illumination conditions will be different. This is called fixed-pattern noise.

Because a large portion of the CMOS pixel area is used for electronics and does not collect light, the quantum efficiency of this sensor is very low compared to the CCD. The quantum efficiency can be improved by using micro-lenses to direct light to the sensitive region of the pixel. For a CCD, most of the electronics are implemented in secondary chips, which make the CCD camera electronics bigger.

CCD offers more pixels per area and a larger photosensitive surface. Sensors with a bigger pixel area benefit from a large full well capacity (FWC) and high signal levels. These factors will improve the dynamic range and increase the level of saturation and make the CCD sensor less susceptible to noise. Table 4.1 and 4.2 shows the CCD and CMOS specifications compiled from today's leading manufacturers.

CCD	**Atmel**	**Kodak**	**SITe**	**Sony**	**Thomson**
	TH7899M	**KAF-1001E**	**SIA502AB**	**ICX422AL**	**THX7899M**
Array (pixels)	2048x2048	1024x1024	512x512	768x494	2048x2048
Pixel Size (µm)	14	24	24	11.6x13.5	14
FWC (e^-)	270,000	87,000	300,000	60,000	150,000
Dynamic Range	80dB	79dB	86dB	59dB	74dB

Table 4.1: CCD sensors specifications [1][7][8][9][10].

In table 4.1, the dynamic range values were measured at 298 K. The table indicates that in general the dynamic range improves significantly with higher full well capacities and larger pixels. For our cameras, the dynamic range at room temperature was 59 dB and 74 dB for the Sony and the Kodak CCDs respectively. The dynamic range disadvantage of the Sony CCD will let us understand the imaging detection limits and requirements for low light detection.

CMOS	**Fillfactory** IBIS5-1300	**Agilent** ADCS 2021	**Omnivision** OV9121	**Micron** MT9V011	**Kodak** KAC 1310
Array (pixels)	1280x1024	640x480	1280x1024	640x480	1280x1024
Pixel Size (µm)	6.7	7.4	5.2	12.0	6.0
FWC(e^-)	120000	68000	78000	63000	40000
Dynamic Range	60-66 dB	65 dB*	60 dB*	60dB	>54 dB

* Dark shot noise not included [11][12][13][14][15].
Table 4.2 CMOS sensors specifications.

Table 4.2: shows that the dynamic ranges of the CMOS are significantly lower than those of the CCD sensors. This difference is due to smaller pixel sizes and smaller FWC.

Noise is the most important criteria for our experimental imaging. Because of less circuitry on the chip, the CCD has significant noise advantages over the CMOS imagers at the pixel level. However, readout noise is bigger for the CCD because of the clocking signals. Moreover, more noise is picked up in the longer charge transfer trajectories in the CCD.

Because CCDs produce the best signal-to-noise ratio, they remain more appropriate for low light applications and for long time integration. Both CCD and CMOS imagers are reliable. However, the CCD offers a superior image quality at the expense of the system size [16]. The CMOS technology uses a higher level of integration but with higher noise figures. Therefore, the CCD remains the technology of choice for detecting fluorescence light [17]. For these reasons, we have decided to test the fluorescence imaging with a full frame cooled CCD and an Interline transfer CCD. The next paragraphs will be devoted to testing the noise performances of our cameras and comprehending the imaging requirements and the detection limits.

Noise Analysis

When dealing with low light applications, noise must be minimized; otherwise, it can obscure the signal. To be able to do so, one should understand the origins of noise and its behavior. The image can be corrupted by noise from a variety of sources, some of which can be overcome and some of which is unavoidable because of the nature of light and current.

The signal, or the grey value of each pixel will depend on C_E, C_D and C_N. C_E, the signal from light exposure, will be proportional to the light intensity and to the time of exposure. This proportionality factor will be dependent on the sensitivity and the adjustments of the analog to digital converter. C_D represents the electrons excited with the dark current, in dark conditions. C_N represents signal from all noise sources. Signals C_E and C_D are deterministic while C_N is a random signal.

$$C_{tot}=C_E+C_D+C_N \quad \text{(eq 4.1)}$$

The noise associated with the light exposure C_E is called the photon shot noise. The shot noise is due to the random arrival of photons in the pixel and to the random transfer of energy from photons to electrons. This noise power is proportional to the irradiance (the number of electrons excited *S*), and the time of exposure *t*. The shot noise amplitude is provided by the following formula derived from Poisson statistics theory [18]:

$$N_{shot}=\sqrt{S} \qquad (4.2) \qquad N_{shot}\alpha\sqrt{t} \quad (4.3)$$

Similarly, the dark signal C_D will generate the dark shot noise N_{DShot} which is also proportional to the square root of the time of exposure. The dark current is also dependant on temperature:

$$C_D \ \alpha \ T^{1.5}e^{\frac{-E_g}{2kT}} \quad (4.4)\ [17]$$

, where *k* is the Boltzmann's constant, T the temperature and E_g the band gap.

The reset noise N_R is another component of C_N which takes place at the CCD output, where the charge-to-voltage conversion is achieved [18]. This noise is due to the uncertainty of the sense capacitor and also related to the temperature *T* by:

$$N_{reset}=\frac{\sqrt{kTC}}{q} \quad (in\ electrons) \quad (4.5)$$

where *k* is the Boltzman's constant. Then, comes the thermal noise which is generated by the amplifier's resistance and the multitude of resistive elements in the camera circuitry. This thermal noise, also called Johnson noise, is expressed as

$N_{thermal}=\sqrt{4kTBR} \quad (Volts)$ (4.6), where *B* is the bandwidth and *R* the effective

resistance. The bandwidth *B* is inversely proportional to the exposure time *t*.

$$C_N \alpha \sqrt{(N_{RESET})^2 + (N_{DARK\ SHOT})^2 + (N_{THERMAL})^2 + (N_{SIGNAL\ SHOT})^2} \alpha \sqrt{t} \quad (4.7)$$

The thermal noise is an important indication of the CCD quality; it refers to the number of electrons that reach the conduction band with thermal excitation. As we will see this noise increases considerably with temperature. Thermal noise will be examined later on to assess the need for cooling the imaging sensor. Thermal noise takes place in various part of the imaging hardware. For the CMOS case, these previously cited noises take place at the pixel level.

The CCD read noise comes at a later stage; it is mainly composed of flicker noise in addition to thermal noise. The flicker noise is inversely proportional to the frequency and, the 1/f corner at which the noise stabilizes determines the noise floor. At low read-out rates, this noise can greatly take part in the overall noise.

Operating the CCD requires clock signals to transfer the charge from the pixels to the register. The generation of these clock signals induces the clocking noise.

Spatial noise includes the photo response non uniformity and dark current non-uniformity also called fixed pattern noise [19]. The photo response non-uniformity is more noticeable in CMOS because of the differences in gain between the pixels due to the uncertainties of the manufacturing process. Since spatial noise depends on manufacturing defects, this noise is difficult to eliminate. On the other hand, temporal noise can be removed with a variety of techniques. As demonstrated in equation 4.7, increasing the exposure time increases the signal-to-noise ratio (if the signal does not reach saturation). Moreover, temperature related noise can also be attenuated by cooling the CCD and the camera circuitry.

Need for Cooling

Our challenge is to produce images in situations where only a few photons are available without being bothered by noise. Generally, fluorophores have a low quantum efficiency, which makes the number of photons reaching the CCD very small. When the excitation light is limited, long time integration remains the only way for detecting these fluorophores.

First, cooling will attenuate the thermal noise, the reset noise the dark current and its resulting shot noise. Secondly, when performing long time integration with a CCD, it is necessary to consider the effects of dark current on the image. At very short exposure time, such as 30 frames per second, the amount of dark current per frame is so small that it can generally be neglected. However, during low light imaging, when a single frame can be extended well beyond a second, charge due to dark current accumulates rapidly and the image quality degrades. The dark current can significantly damage the image clarity. In most cases, the benefits of cooling come from its ability to reduce the dark current generated by the camera.

This raises a critical question. When does a cooled camera become necessary? The answer will depend on the ambient temperature and on the total dark current noise generated due to temperature, exposure time and on the expected photon flux. CCDs can be cooled either with thermoelectric (TE) coolers or liquid nitrogen to reduce the thermal noise. Therefore, the need for cooling the CCD will depend on the noise performance of the CCD chip (SNR) and the conditions in which the experiment takes place. In our

application TE cooling could be used, but increases power dissipation and complexity. We hope to avoid cooling if possible.

Experimental CCD Performance

Two types of CCD cameras were used for the fluorescence imaging apparatus. These two cameras were used to assess the need of a cooled camera and to quantify the noise generated by each one of them. The first camera was a Roper Scientific Sensys cooled CCD camera. The second one was a commercial uncooled analog CCD camera from JAI.

Sensitivity is a key parameter in determining the quality of a photo-detector. It refers to the minimum light power that the photodetector can detect. For our application, a good sensitivity from the violet to the red was important for fluorescence detection. Due to the nature of our fluorescence system, not all the visible light was used for detecting fluorescence. For the detection of hydrocarbons and biologic specimens, the CCD photosensitivity should be satisfactory in the violet and in the green-red portion of the visible spectrum. Moreover, the reflected light imaging was done only with a red LED. For these reasons, a monochromatic CCD was chosen instead of a color CCD. Figure 4.2 and 4.3 show the sensitivity of the CCD cameras used for this study.

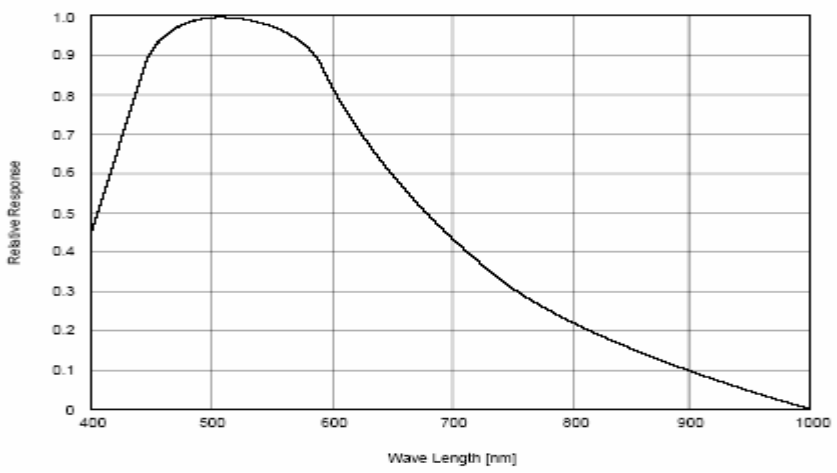

Figure 4.2: The Sony ICX422AL CCD relative sensitivity used in the JAI camera [3].

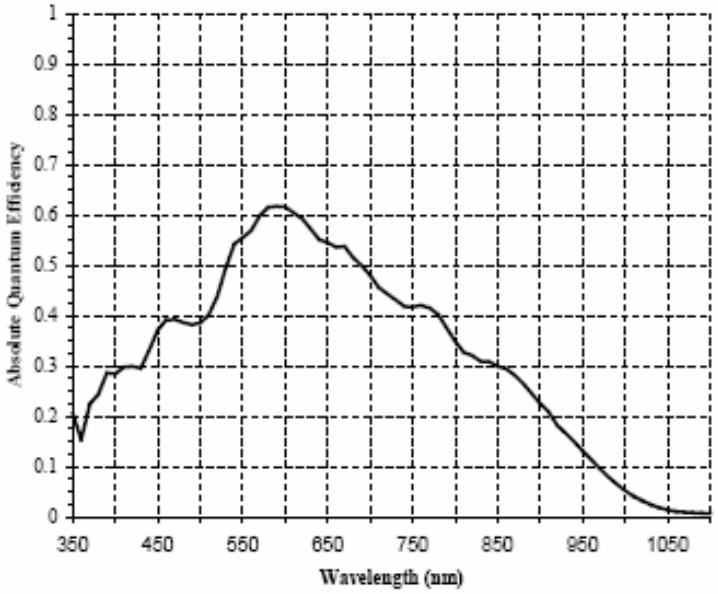

Figure 4.3: The KAF-0401E CCD sensitivity, used in the Sensys camera [2].

The sensitivity is not homogeneous in the entire spectrum and that depends on the nature of the semiconductor.

Long Time Integration

To measure fluorescence signals with low QE fluorophores, one needs to integrate for longer periods of time. Long time exposure improves the detection capabilities of the camera and is extremely useful for low light applications. Since the signal is proportional to time and the shot noise is proportional to the square root of time, longer exposure periods result in better SNR.

To be able to study the behavior of the noise versus the time of exposure, we need to change the exposure time of the camera. Our two cameras had the possibility of long time exposure. The Sensys camera came with that option. However, the JAI analog camera needed some modification on its circuit board and some external input signals.

The analog uncooled camera was connected to a computer through a frame grabber by National Instruments. The video signals had to follow the NTSC standard (National Television System Committee), which consists of 525 horizontal lines per picture. The NTSC system frequency is set to 30 frames per second or 15750 lines per second. The video output of the camera consists of a composite signal that contains a vertical signal VD (vertical drive) and a horizontal signal HD (horizontal drive).

To change the exposure time, the camera had to be driven by the input signal VD and horizontal drive HD. The duty cycle of these signals had to follow the manufacturer's requirements. These signals' specifications were first measured with help of a SYNC separator chip that splits the composite video signal. The exposure time is controlled by the time between the VD pulses, and for each VD pulse the resulting two fields will be read. These pulses were synchronized with the video output of the camera.

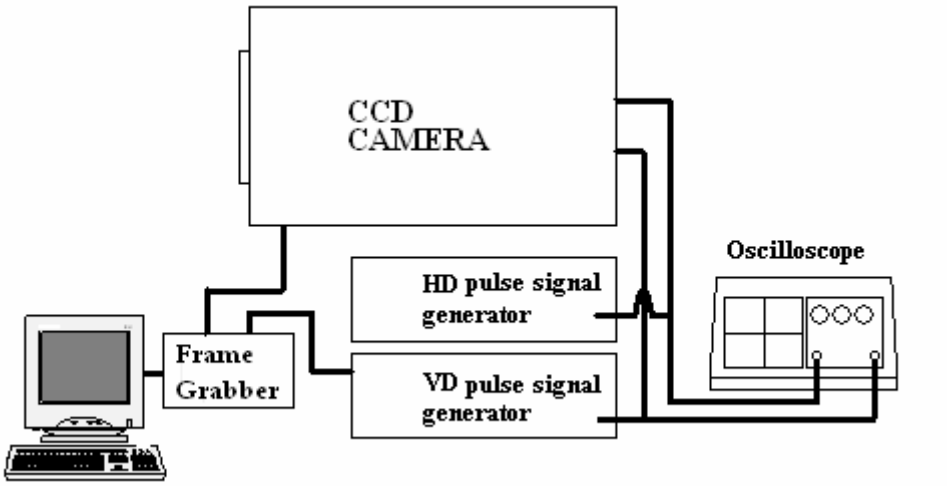

Figure 4.4: Hardware setup for the long time exposure mode.

The frame grabber on the computer was controlled by a LABVIEW program. This program was made to synchronize between the signals and to acquire pictures.

Sensitivity

To test the sensitivity of our CCDs, the camera was exposed to a laser beam. The beam irradiance was attenuated by using neutral density filters. The intensity or pixel charge was measured with MATLAB and expressed in grayscale as a number from 0 to 256. The digital scale depends on the camera's analog to digital converter ADC.

An important characteristic of the CCD system is the linearity in response to incident light, particularly when applied for quantitative photometric or radiometric analysis. Both CCDs gave a quite linear response, and for the same wavelength the current generated was proportional to the number of photons received.

Figures 4.5, 4.6 and 4.7 will be used to assess the fluorescence intensity emitted by our samples.

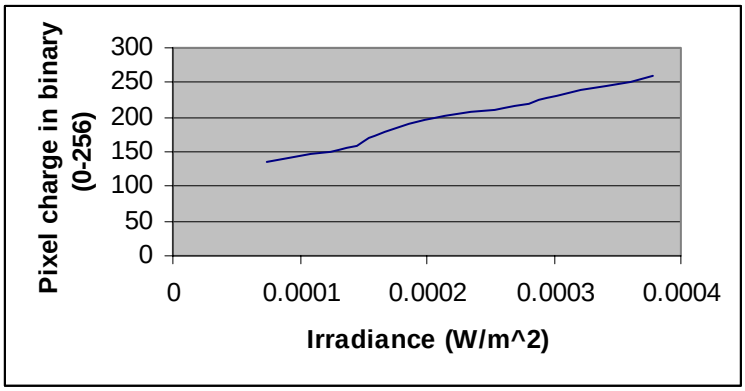

Figure 4.5: Pixel charge versus the irradiance for one second of exposure time, at 500 nm and 25 ºC for the JAI camera.

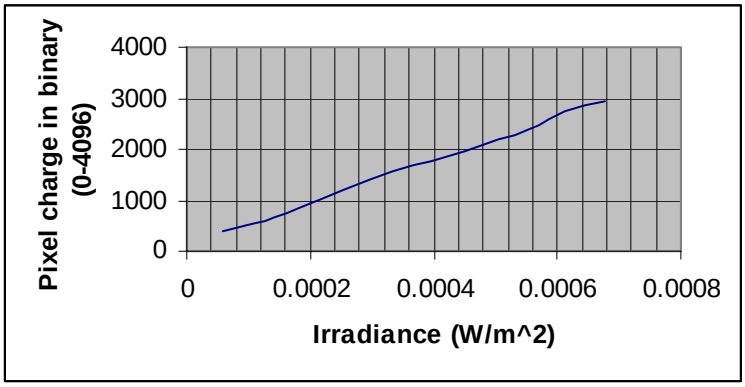

Figure 4.6: Pixel charge versus the irradiance for one second of exposure time, at 500 nm and 10 ºC for the Sensys camera.

For each exposure, the grayscale level was proportional to the irradiance and to the time of exposure *t*.

The linear sensitivity is a characteristic of the CCD detector that is not available on the CMOS sensor. CMOS actual sensitivity tends to be more logarithmic which can be advantageous for observing objects with large brightness variations.

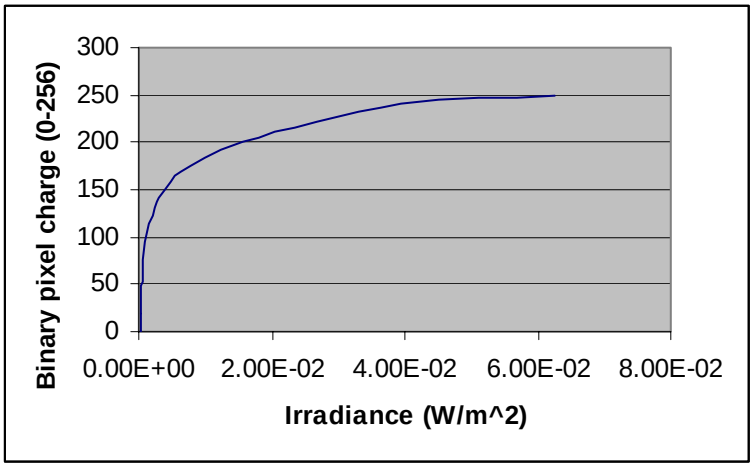

Figure 4.7: Pixel charge versus the irradiance for 1/100 second of exposure time, at 632nm nm for the IC-Media 515_E CMOS [20].

The graph in figure 4.7 was measured with a standard CMOS sensor from IC Media, Inc [20]. Other manufacturers choose to hide this non linearity by altering the amplification and charge-to-voltage conversion. Unfortunately, this CMOS sensor could not be driven for longer exposure periods.

Noise Measurements

The noise behavior was analyzed with the help of an oscilloscope and with MATLAB. The following picture shows the oscilloscope reading in one field and the VD signal below that enables the frame's read out process.

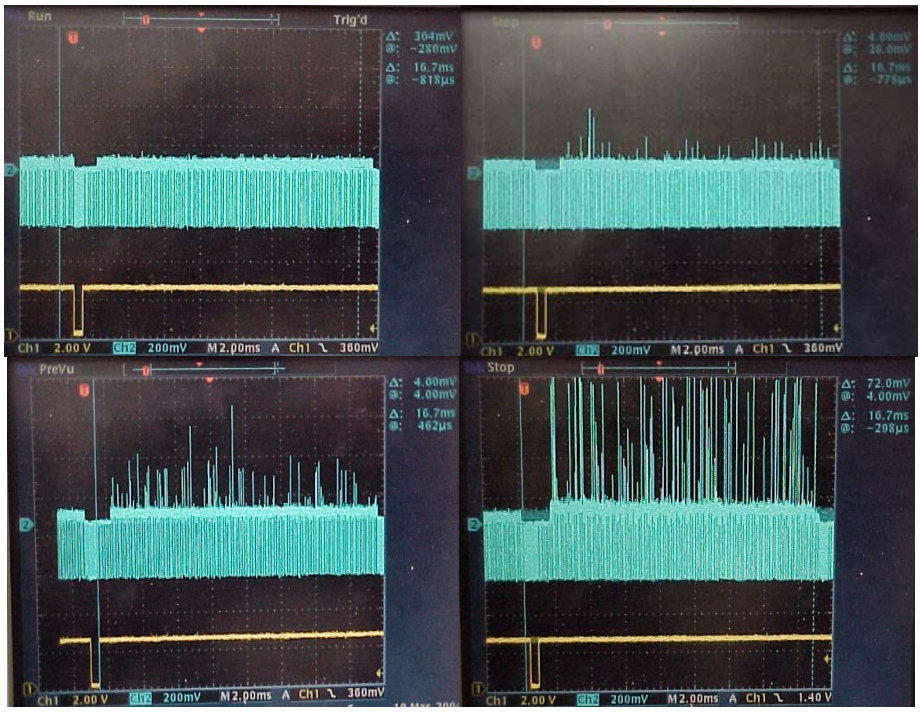

Figure 4.8: Oscilloscope noise readings for 1, 10, 20 and 30 seconds of exposure time for the uncooled camera.

Figure 4.8 shows the video signal of the uncooled camera. The portion seen represents one field. Each peak represents the total noise in one line of the field (640 pixels). The uncooled camera has exactly 525 lines. As we can see, the noise in each line increases with the exposure time.

Not all the pixels have the same behavior. Due to CCD irregularities, some pixels suffer more than others from dark current. The graphs in figure 4.9 were realized with the help of MATLAB in dark conditions. The integration time was set to 1/100 seconds for both the CMOS (ICM-515_E) and the uncooled CCD. For that exposure time, noise was very noticeable for the CMOS and almost non existent for the CCD. The average binary dark noise was about 0.05 out of 256 for the CCD and 0.4 out of 256 for the CMOS.

Figure 4.9 shows the random distribution of pixel noise for the CMOS and uncooled CCD camera.

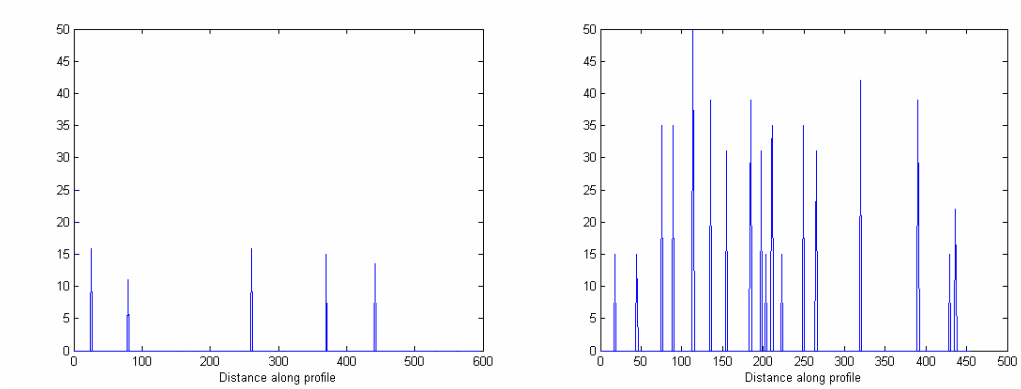

Figure 4.9: Random pattern noise for the CCD (left) and CMOS (right) at 1/100 second of exposure.

Even at low exposure time, the pattern noise is very abundant and intense for the CMOS camera and almost non-existent for the uncooled CCD. Unfortunately, the CMOS camera from IC-Media could not be driven for longer exposure times.

Exposure time	Number of saturated pixel	Pixels with over half the FWC
0.5	0	0
1	5	21
10	31	1556
20	107	2984
30	1308	4520
Total number of pixels	307200	

Table 4.3: Pixel statistics on the uncooled CCD in dark conditions.

The illustration below shows the grayscale changes due to long exposure noise.

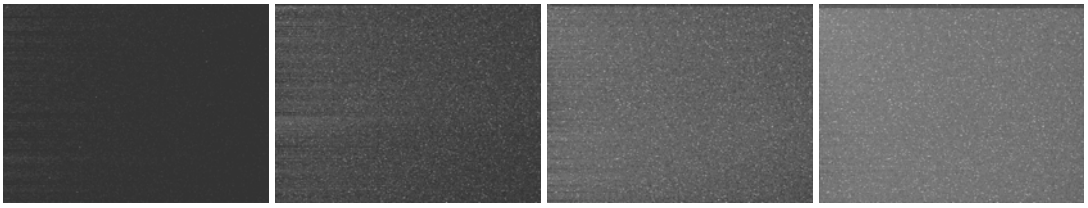

Figure 4.10: Pictures of dark noise at 1, 10, 20, and 30 seconds with the uncooled CCD camera at 25 ºC.

Figure 4.11 illustrates the total dark noise of the uncooled CCD camera versus the exposure time. The measurements were taken with a closed shutter. Data were gathered by dividing the total image noise charge in binary over the total number of pixels at room temperature. Again, this dark noise is the addition of the thermal noise, the dark shot noise, the reset noise, the flicker noise, and the fixed pattern noise. In general, the overall noise follows a square root behavior. Figure 4.11 shows that for the same temperature and exposure time, the average picture noise had many variations.

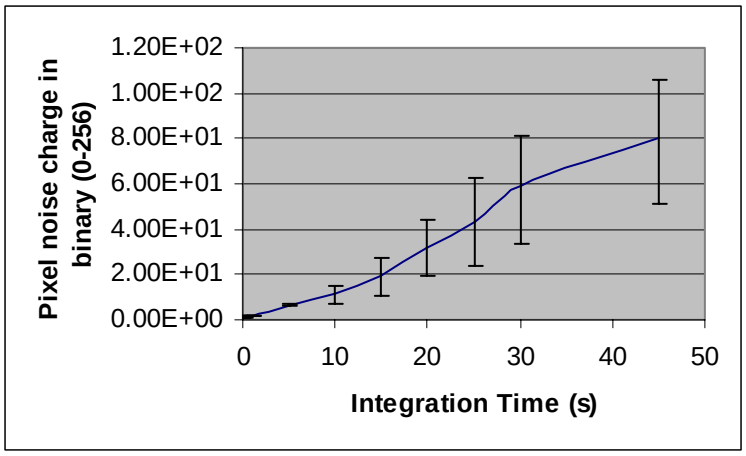

Figure 4.11: Average pixel noise charge variations versus the exposure time for the uncooled CCD camera.

The error bars in figure 4.11 show the average noise variations for he same exposure time. These variations were smaller than 1% of the total binary charge for an

exposure times less than 5 sec. For an exposure time of 5 seconds, the dynamic range is of 35 dB compared to 50 dB at 0.1 seconds.

To understand the effect of thermal noise, the camera was exposed to high temperatures. Again, the images were taken with the uncooled CCD camera at dark conditions and with one second of exposure. The approximate temperature was measured by a thermo-electric sensor. The histograms in figure 4.12 show that the charge of a significant number of pixels increases with a temperature change of 10 K.

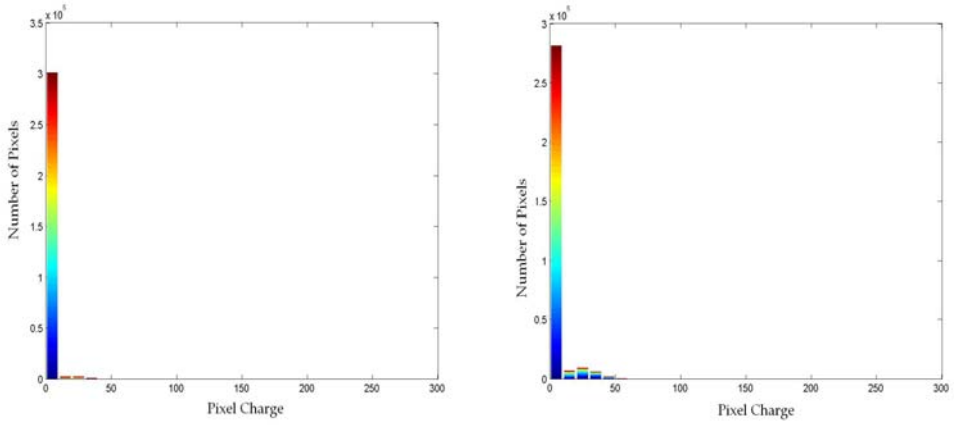

Figure 4.12: Histogram of pixel noise distribution at 298 and 309 K for the uncooled camera.

These variations were quantified, and the graph below shows that the average pixel charge due to dark noise doubles approximately every 5 K.

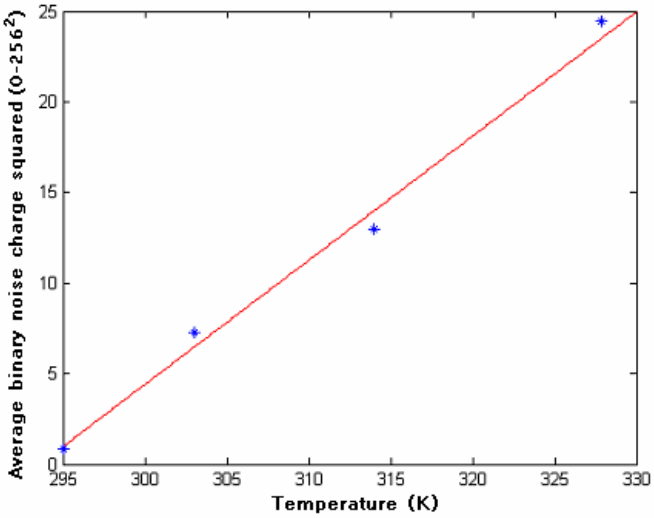

Figure 4.13: Dark noise intensity squared versus temperature for the uncooled camera at 1/10 seconds of integration time.

As illustrated, the dark noise behavior followed a square root of temperature relationship just like the thermal noise equation predicted. Exposing the cooled camera to different temperatures was not possible. The manufacturer specifications indicate that the Sensys CCD generates a dark noise of 25 electrons per pixel per second at room temperature and only 1 electron per pixel per second when cooled at 10^{o}C. Without cooling, the dark noise of the Sensys camera doubles every 6 K.

The following histograms show the pixel noise charge with no illumination for the cooled and uncooled camera. The total number of pixels is about 373K and 359K for the cooled and uncooled camera, respectively.

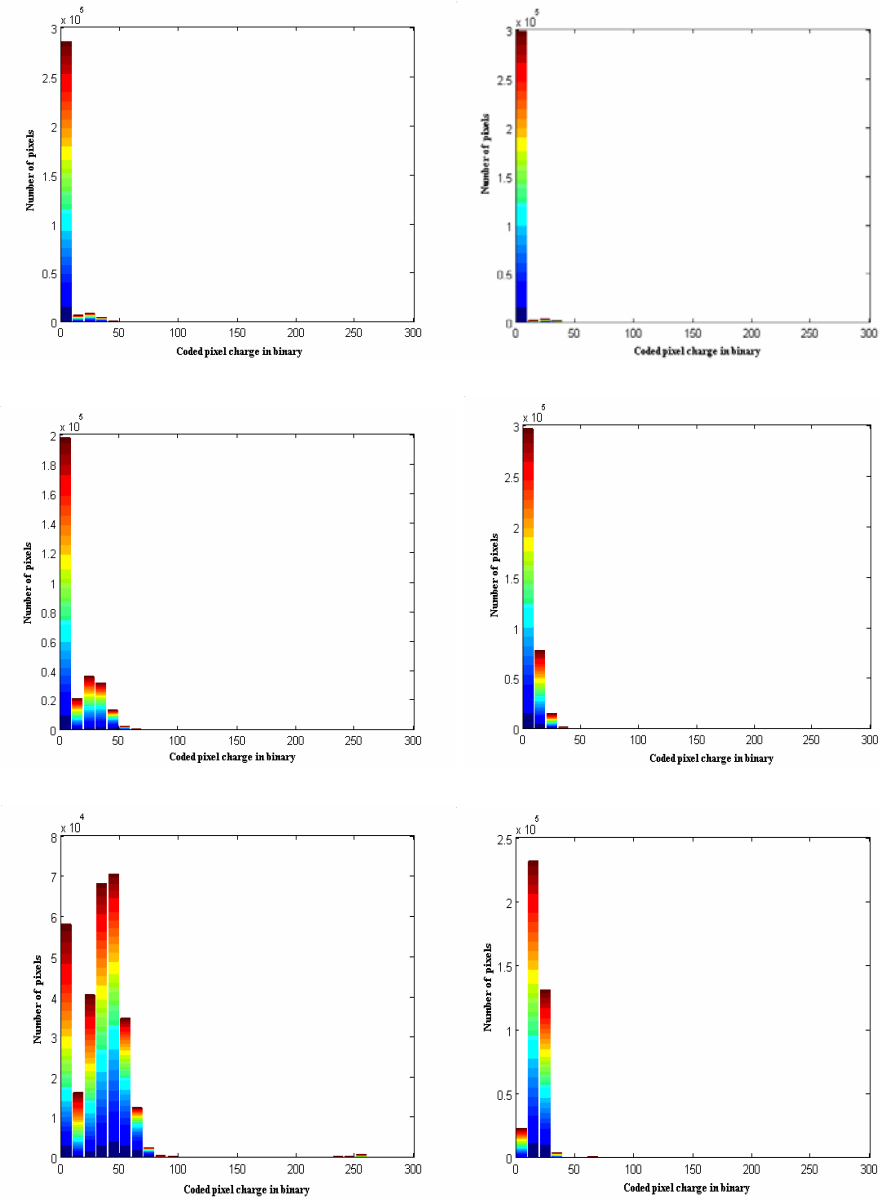

Figure 4.14: Noise generated in a cooled camera (right) and the uncooled camera (left) for one, fifteen, and thirty seconds of exposure time.

At room temperature and for short exposure periods, the noise behavior of the uncooled camera is quite similar to the cooled camera. At thirty seconds of exposure time, the hot pixels generated with the uncooled camera are very numerous, while no pixel saturates for the cooled camera.

In general, CCDs with a high well capacity are less affected by noise. At room temperature our CCDs generate similar amounts of noise, 36 to 39 electrons per pixel. Our cameras had a full well capacity of 60000 and 87000 electrons per pixel for the JAI and Sensys CCD respectively [2] [3]. Consequently, the size of the full well makes a considerable difference in the signal-to-noise ratio. Without cooling, the noise performances of the Sensys CCD remain better than the ones of the JAI CCD.

The choice of the right CCD sensor is very important and will depend on the experimental objectives. The histograms above show clearly the advantages of cooling. The cooling clearly enhances the quality and clarity of the images. However, due to the aspiration of miniaturization the cooling process could be neglected. Frame transfer or interline transfer CCD with micro-lenses are preferred since they do not rely on a shutter. Cooling can be substituted by high signal-to-noise ratio CCD chips.

In the next chapter, fluorescence pictures will be presented and investigated. The need for cooling will be determined, depending on the exposure time needed to observe the fluorescence of each sample. However, field experiments and the outside temperature will assess the ultimate need for cooling. From our experimental results, at room temperature, the uncooled CCD had a good noise performance until 5 seconds of exposure. In addition, the noise floor and the hot pixels could be detected and canceled with some image processing. The randomness and the sparse distribution of noise might not be as well perceived by the eye.

REFERENCES CITED

[1] *"George Smith and Willard Boyle Win C&C Prize for Charge-Coupled Device,"* from <http://www.bell-labs.com/news/1999/september/20/1.html>, accessed April 5, 2003.

[2] Eastman Kodak Company, Image Sensor Solutions, Rochester, New York 14650-2010, June 26, 2000,from <http://www.fli-cam.com/downloads/kaf0401e.pdf> accessed January 15, 2003.

[3] JAI PULNiX Inc, 1330 Orleans Drive, Sunnyvale, CA 94089, Phone +1 949 472-5900, from <www.jai.com/db_datasheet/cvm300db.pdf> accessed January 15, 2003.

[4] M. Abramowitz, K. R. Spring, J. C. Long, K. I. Tchourioukanov, M. W. Davidson *"Concepts in Digital Imaging Technology,"* from <http://www.olympusmicro.com/primer/digitalimaging/concepts/concepts.html>, accessed February 2, 2003.

[5] K. R. Spring, M. W. Davidson, Quantum Efficiency, from <http://www.olympusmicro.com/primer/digitalimaging/concepts/quantumefficiency.html>, accessed February 2, 2003.

[6] CMOS Advantages, from <http://www.micron.com/products/imaging/technology/advantages.html>, accessed January 2, 2003.

[7] Eastman Kodak Company, Image Sensor Solutions, Rochester, New York 14650-2010, Image Sensor Solutions, from <http://www.kodak.com/global/en/digital/ccd/>, accessed June 3, 2003.

[8] SITe, 10500 SW Nimbus Avenue Tigard, OR 97223-4310, Phone 503.431.7100, from <http://www.site-inc.com/products.html>, accessed July 7, 2003.

[9] Apogee Instruments, Inc, 11760 Atwood Road, Auburn, California 95603, Phone: 530-888-0500, from <http://www.apogee-ccd.com/ap-specs.html.>, accessed June 1, 2003.

[10] Atmel Corporation. 2325 Orchard Parkway, San Jose, Ca 95131, 1 (408) 441-0311, CCD Image Sensors- Datasheets, from <http://www.atmel.com/dyn/products/datasheets.asp?family_id=614>, accessed June 3, 2003.

[11] Eastman Kodak Company, Image Sensor Solutions, Rochester, New York 14650-2010, *"CMOS Image Sensor Family Overview,"* from <http://www.kodak.com/global/en/digital/ccd/products/cmos/cmosMain.jhtml>, accessed July 7, 2003.

REFERENCES CITED CONTINUED

[12] Agilent Technologies, Inc. 5301 Stevens Creek Blvd, Santa Clara, CA 95051, Phone: 1 (800) 235-0312, Image Sensors, from <http://cp.literature.agilent.com/litweb/pdf/5988-8616EN.pdf/>, accessed June 3, 2003.

[13] FillFactory nv, Schaliën hoeved reef, 20BB-2800 Mechelen, Belgium, Phone: +32.(0)15.446.333, from <http://www.fillfactory.com/htm/products/htm/ibis5/ibis5.htm>, accessed June 3, 2003.

[14] OmniVision, Inc. 1341 Orleans Drive, Sunnyvale, CA 94089, Tel: +1 408 542 3000, from <http://www.ovt.com/pdfs/ds_9630.pdf>, accessed July 7, 2003.

[15] Micron Technology, Inc. Micron Technology, Inc. 8000 South Federal Way, Post Office Box 6, Boise, ID 83707-0006, from <http://download.micron.com/pdf/datasheets/imaging/MT9V011.pdf>, accessed July 7, 2003.

[16] M. Pierre. "Detection of visible photons in CCD and CMOS: A comparative view" *Nuclear Instruments and Methods in Physics Research,* Section A: Accelerators, Spectrometers, Detectors and Associated Equipment, Volume 504, Issue 1-3, May 2003, pp. 199-212.

[17] J. Janesick, "Lux transfer: complementary metal oxide semiconductors versus charged-coupled devices," *OE Magazine*, Volume 41, Issue 6, June 2002, pp.1203-1215.

[18] B. Saleh, M.C. Teich, *Fundamentals of optics*, Chapter 17, John Wiley, 1991.

[19] H. Helmers, M. Schellenberg, "CMOS vs. CCD sensors in speckle interferometry," *Optics and Laser Technology*, Volume 35, Issue 8, November 2003, pp. 587-595.

[20] IC Media Corporation, 5201 Great America Pkwy, Suite 422, Santa Clara, CA 95054, Tel: 408-213-2000, from <http://www.ic-media.com/products/documents/ICM110U_product%20brief.pdf>, accessed May 3, 2003.

CHAPTER FIVE

IMAGING AND RESULTS USING THE DEMONSTRATION SYSTEM

After talking about our optical design and the imaging sensors, our discussion will continue with an analysis of the detection apparatus performance. This chapter will introduce the imaging results obtained with the table-top demonstration. We will search for evidence of biological traces that exhibit fluorescence using bluish green LED illumination. The detection of fluorescence from polycyclic aromatic hydrocarbons (PAHs) will be performed with a UV LED using the same optical setup. Finally, the Raman spectra of PAHs and biological samples taken from the literature will be presented.

Biological Samples

Several specimens were used to prove the efficacy of our optical system for the detection of biological traces. Biological samples were provided to us from the British Antarctica survey. The samples collected in Antarctica consisted of rocks and lichens. Those samples represent microbial communities that live under extreme temperatures and intense UV radiation, which could have analogues in Mars. The samples obtained were Xanthoria, Cyanobacteria, Acarospora, endolithic bacteria, and Nostoc. Some of our specimens are epilithic; they live on the surface of the rocks such as lichens that rely on UV protective pigments for their survival. Others are endolithic bacteria that live in the

interior of rocks were they are well protected from the severe environment. Cyanobacteria, also known as blue-green algae, are one of the oldest living organisms on earth; they are one of the candidate micro-organisms that could be found on Mars [1]. Cyanobacteria are characterized by their use of chlorophyll as a photosynthetic pigment and also its use of carotenoids as a photo protective pigment [1].

Xanthoria and Acarospora are types of lichens that we had in our possession. Lichens represent a kind of symbiotic life form. The majority of lichens are composed of fungal filaments and algal cells, usually from cyanobacteria [2]. Nostoc is an aquatic form of cyanobacterium that can be found on moist rocks and on the bottom of lakes. Nostoc also makes use of pigments for photosynthesis [3].

Fluorescence Spectra

Before we started testing the fluorescence of our samples with the bench-top system, tests were conducted with a fluorometer. This enabled us to obtain the emission and excitation spectra of our samples and assess their fluorescence efficiency. We found for each sample an optimal excitation wavelength. First, absorbance spectra were obtained, followed by the fluorescence emission for each sample. It turned out that most of these samples could give a significant fluorescence emission for green or blue wavelength excitation. However, to simplify our optical probe one excitation wavelength had to be selected. Therefore, we decided to use a bluish-green LED with a middle wavelength of 500 nm and with a 20 nm wide bandpass filter.

The following results were conducted on a Spex Industries, Inc "Fluorolog." The y-axis scale is proportional to the number of photons that reach the sensor, scaled by the magnification of the photomultiplier. The experiment procedures and calibrations were made according to Dr P. Callis recommendations.

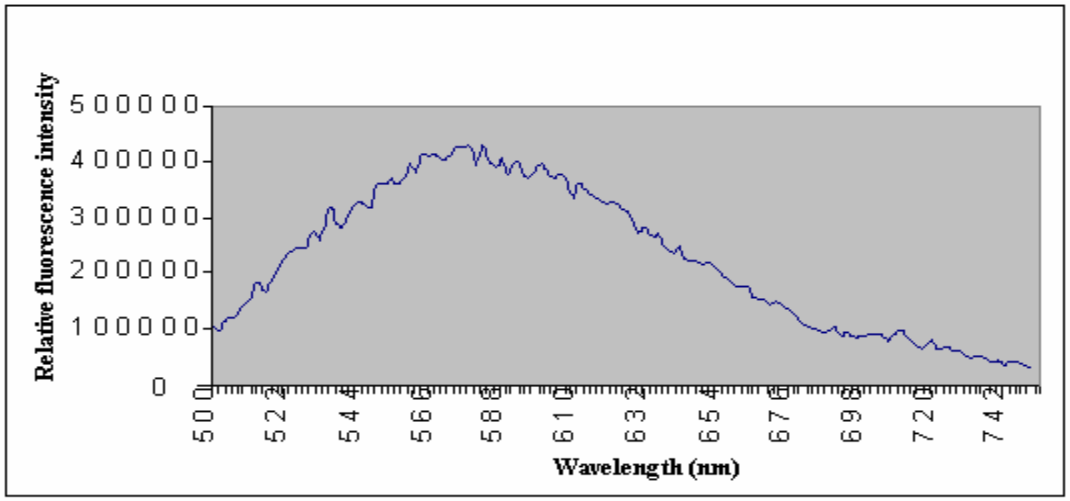

Figure 5.1: Fluorescence emission spectrum of Acarospora excited at 470 nm.

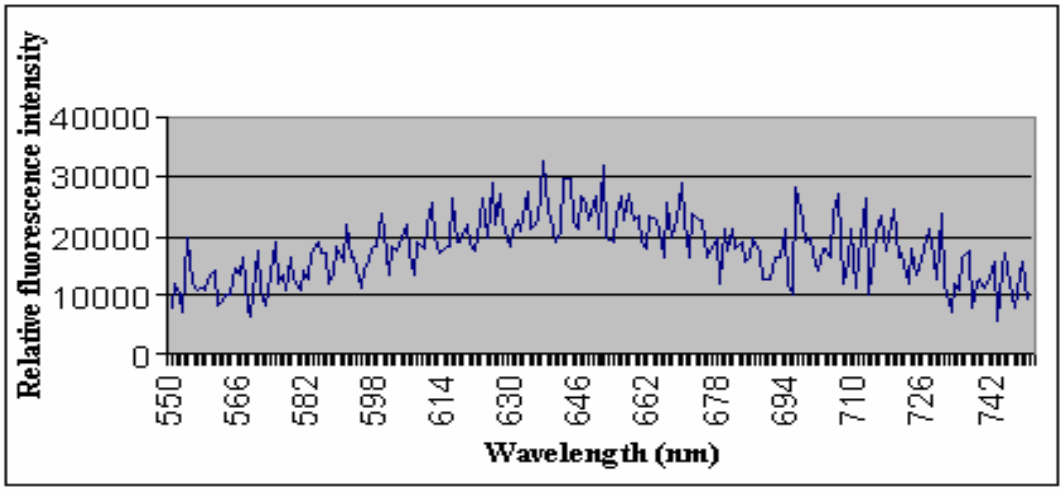

Figure 5.2: Fluorescence emission spectrum of Xanthoria excited at 500 nm.

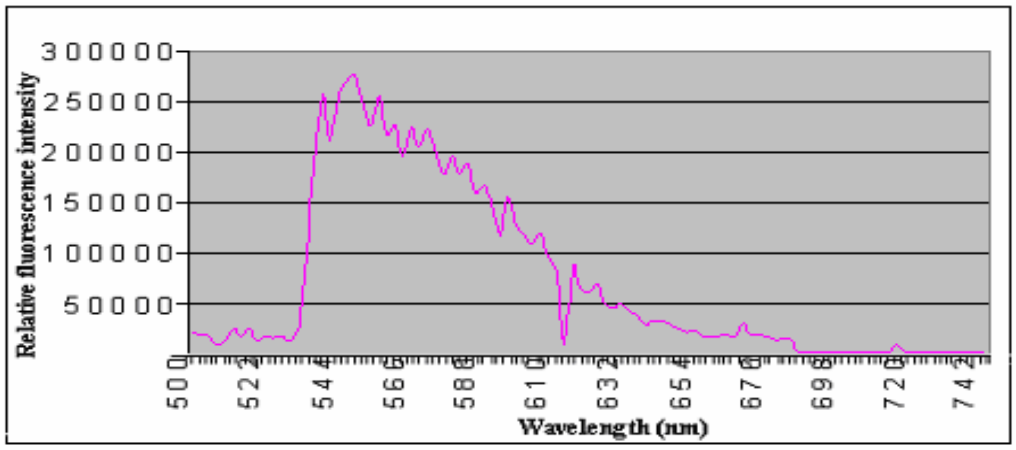

Figure 5.3: Fluorescence emission spectrum of endolithic bacteria excited at 480 nm.

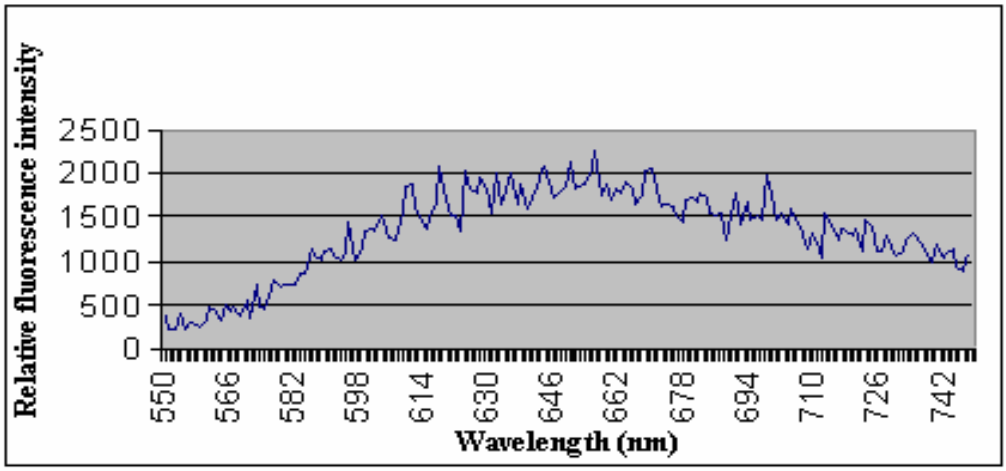

Figure 5.4: Fluorescence emission spectrum of Nostoc excited at 510 nm.

The excitation light of the fluorometer was generated with a high intensity Xenon lamp. The samples were excited at various finite wavelengths; these wavelengths were selected with a grating surface. The excitation wavelengths were further reduced with the use of narrow slits. Only a limited surface of the sample was exposed to light. As illustrated, the fluorescence response of each sample was very distinctive. Because of the diffuse reflections from our rough samples, different intensities were obtained for the

same sample with the fluorometer. The results were depending on the orientation and the position of the sample. Of these samples, Nostoc had the least primary fluorescence.

The same tests were conducted with poly-aromatic hydrocarbons. These hydrocarbons are known to exhibit an abundant fluorescence with the far UV excitation. However, the farthest UV LED that we could get had a peak emission of 370 nm with a spectral width of 50 nm. Figures 5.5 and 5.6 illustrate the fluorescence emission of gasoline and diesel. Even at the short UV wavelengths the fluorescence of PAHs remains very strong.

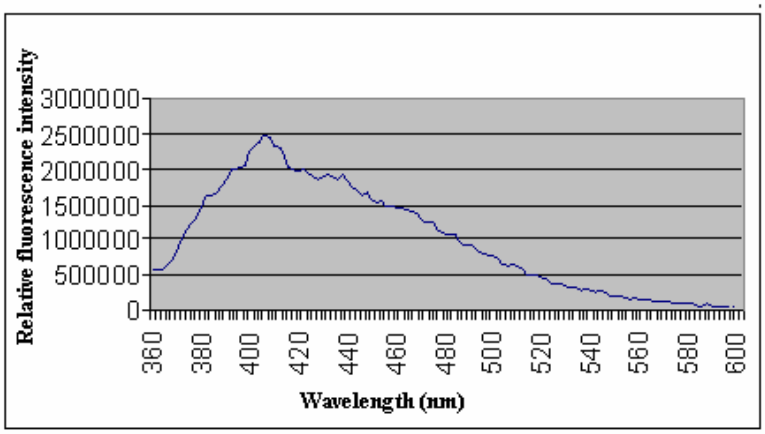

Figure 5.5: Fluorescence emission spectrum of gasoline excited at 350 nm.

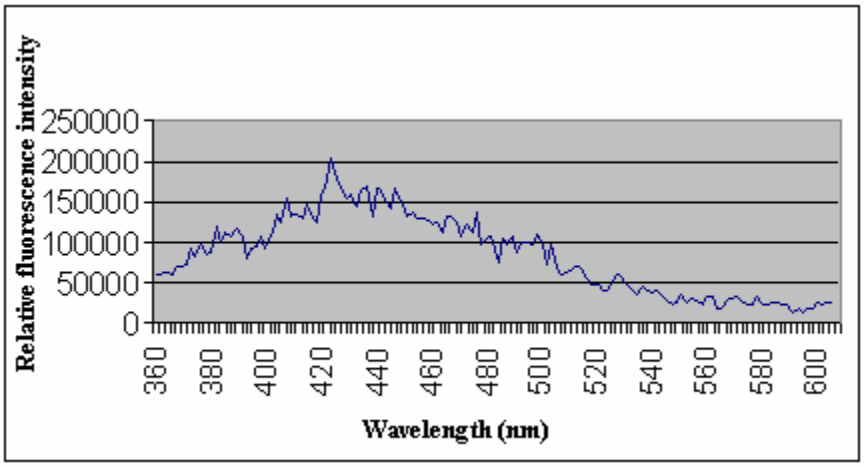

Figure 5.6: Fluorescence emission spectrum of diesel excited at 350 nm.

Diesel and Gasoline contain aromatic hydrocarbons at different concentrations and varieties, with more poly-aromatic hydrocarbons in diesel [4]. These aromatic molecules are responsible for the fluorescence of these fuels. Benzene, toluene, and xylene are examples of PAHs hazardous to the environment. The absorption wavelength of the aromatic hydrocarbons decreases as the number of rings of the aromatic hydrocarbons increases [5].

Imaging Results

To test the efficacy of our filters, fluorescent beads were purchased from Molecular Probes, Inc. The fluorescence/emission wavelengths of these beads were chosen to match the wavelengths of our filters. The spectra of our filters shown in figure 5.7 were obtained with an Advantest optical spectrum analyzer. The FWHM of the bandpass filter was 25nm; the spectrum shows no overlap between the filters.

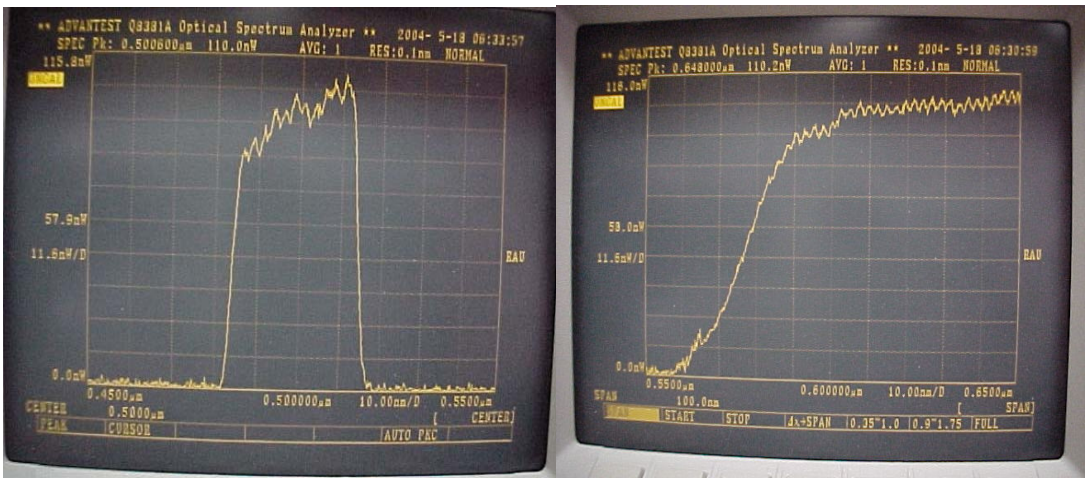

Figure 5.7: Spectra of the Long-pass and band-pass optical filters used for the micro beads detection, on a 10 nm per division scale.

Figure 5.8 shows the manufacturer's specifications of the emission spectra our beads when excited at 488 nm.

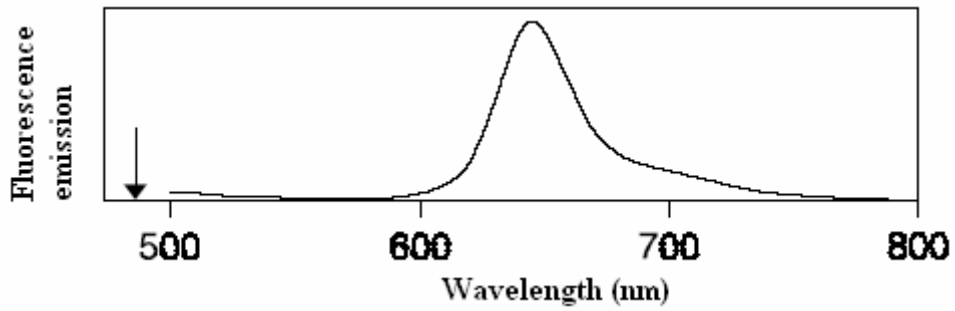

Figure 5.8: Fluorescence spectrum of the 1µm carboxylate microspheres [6].

Non-fluorescing Polystyrene beads of the same size were also purchased. This will let us distinguish between the beads by their emission wavelengths. To test the proper working of our filters, non-fluorescent beads were placed on a microscope slide and illuminated with the bluish-green LED at very high intensity. These beads were not detected by the CCD, which proved that there was no overlap between the long pass filter and the LED with the bandpass filter. The testing was also done visually on a microscope by shining high intensity white light through the bandpass filter.

A solution was prepared containing both types of beads and placed on a microscope slide. Fluorescence images were taken with a fully opened iris (effective NA=0.58); while, the black and white images were taken with a small aperture to adjust the scattered light intensity. All the coming pictures were taken with monochromatic cameras. With the help of MATLAB, black and white images were converted into color images based on green and red color. The red color represents the scattered light, while the green color shows the fluorescence emission intercepted by the CCD.

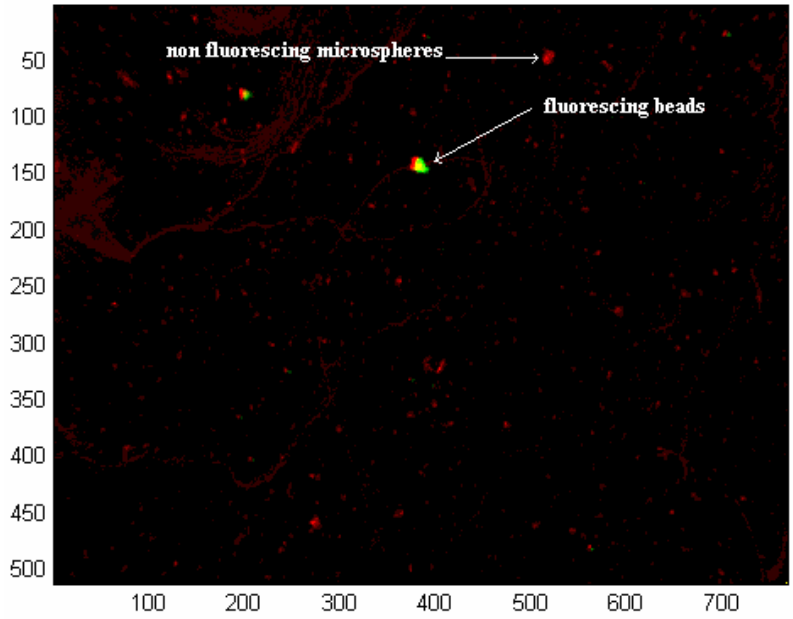

Figure 5.9: MATLAB color processed image of fluorescing beads and micro-spheres. This image was taken with the cooled camera with one second of exposure at 10 ºC.

In figure 5.9, big fluorescing spots represent clusters of beads; individual fluorescing beads could also be observed. The images where taken with the cooled camera, with a magnification of 1.42X. The area enclosed within the field of view is 4.85 mm by 3.23 mm.

Detection of Bio-Signatures

After verifying our fluorescence optical design using beads, we started testing the fluorescence of the Antarctica samples. Figures 5.10 and 5.11 illustrate the fluorescence and black and white image of Nostoc followed by the color MATLAB processed image showing the fluorescence in green. The low fluorescence signals of NOSTOC detected by

the fluorometer can be due to a bad positioning of the sample. The black and white imaging reveals that only few elements of NOSTOC sample are fluorescing.

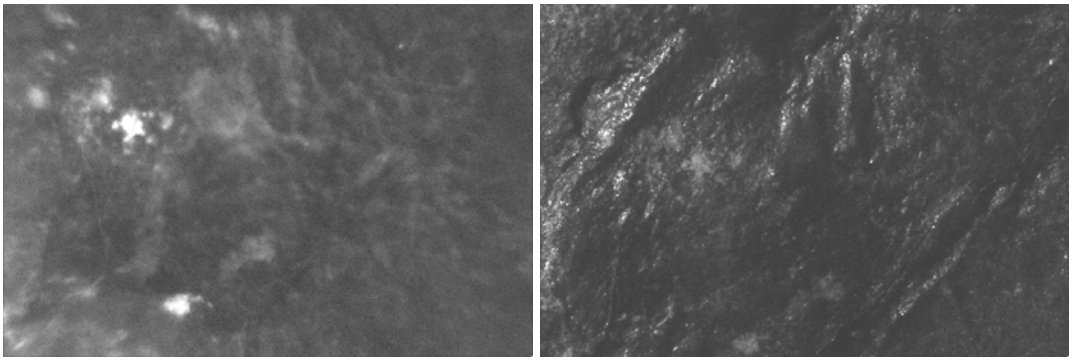

Figure 5.10: Fluorescence (left) and black and white image (right) of Nostoc. These images were taken with the cooled camera with one second of exposure at 10 ºC (LED current of 13 mA).

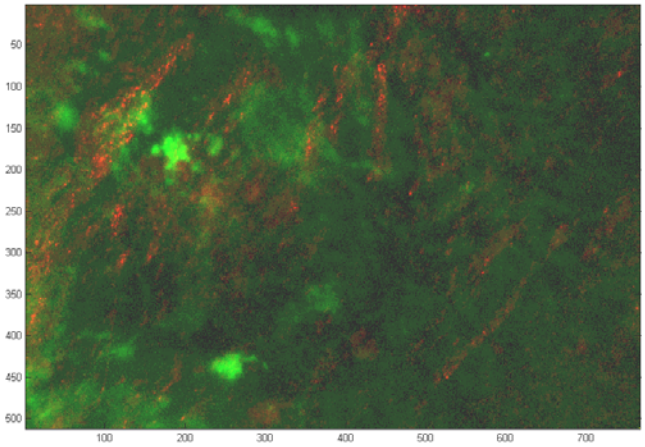

Figure 5.11: MATLAB processed color image of Nostoc fluorescence.

Similar imaging procedure was adopted with Acarospora lichens.

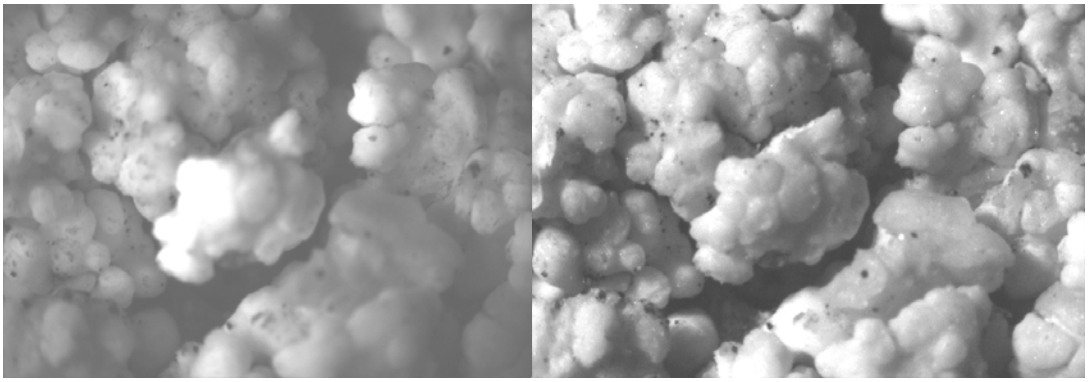

Figure 5.12: Fluorescence (left) and black and white image (right) of Acarospora. These images were taken with the cooled camera with one second of exposure at 10 ºC (LED current of 4 mA).

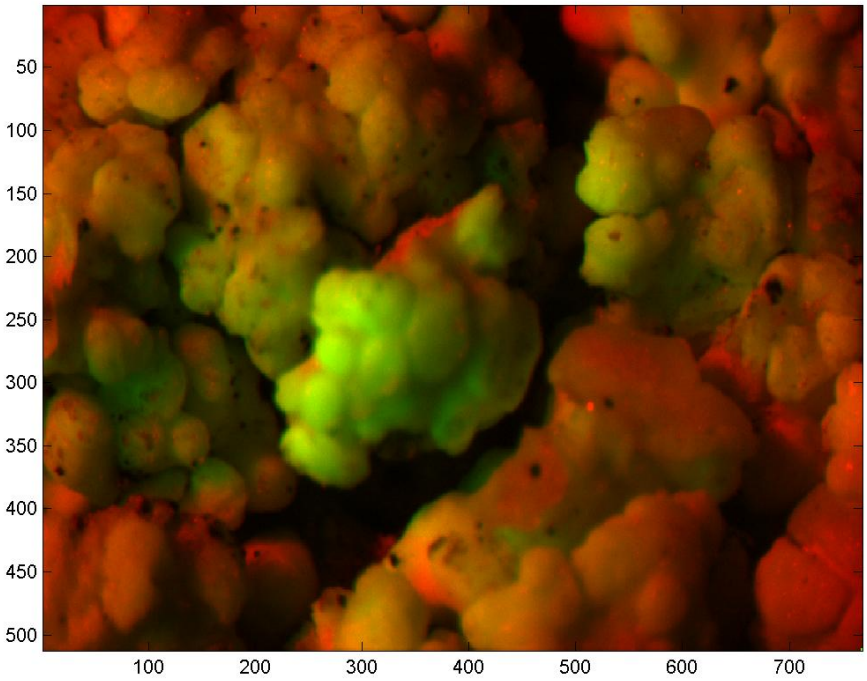

Figure 5.13: MATLAB processed image of fluorescing Acarospora.

Figure 5.14, is the fluorescence image of Xanthoria. This image was taken with the same optical setup with an uncooled camera, with an LED current of 3 mA. That camera had a bigger CCD sensor that gave a bigger field of view of 6.19mm by 4.64mm.

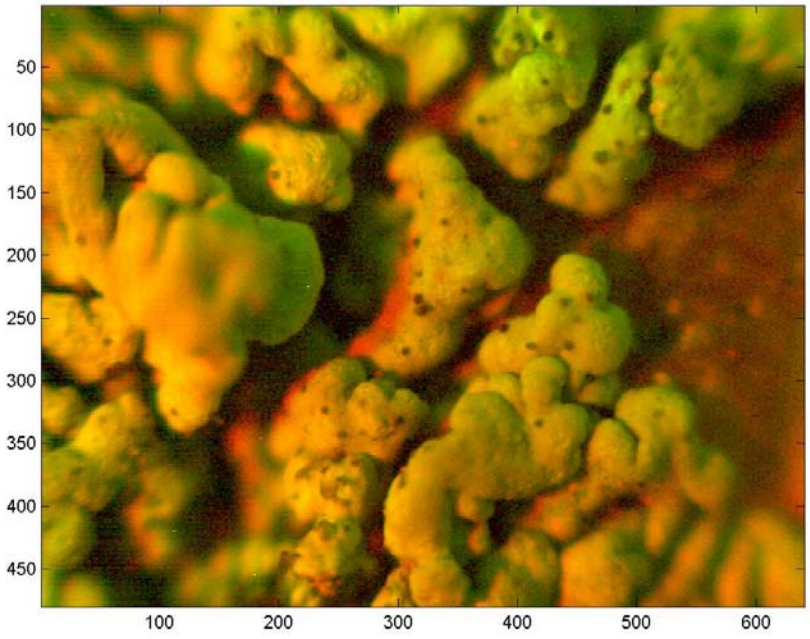

Figure 5.14: Color processed image of fluorescing Xanthoria. This image was taken with the uncooled camera with one second of exposure at 25 ºC (LED current of 3 mA).

Figure 5.14 was taken with one second of integration time. The image shows some traces of hot pixels, and its clarity was not as good as the one from the cooled camera. However, the fluorescence is still very well detectable with the uncooled camera. The SNR approximation of fluorescence images taken with the uncooled camera will be evaluated later for different samples.

Endolithic biological traces can be detected with their distinct layer of bacteria with black and white imaging together with a large field of view and a good depth of field. Details will be brought out further with the use of dark and epi-illumination. The reflectance imaging gives considerable details of the rock by showing the surface structure and its morphology. Figure 5.15 shows the reflected light image of an Antarctica rock taken with an uncooled camera with darkfield illumination.

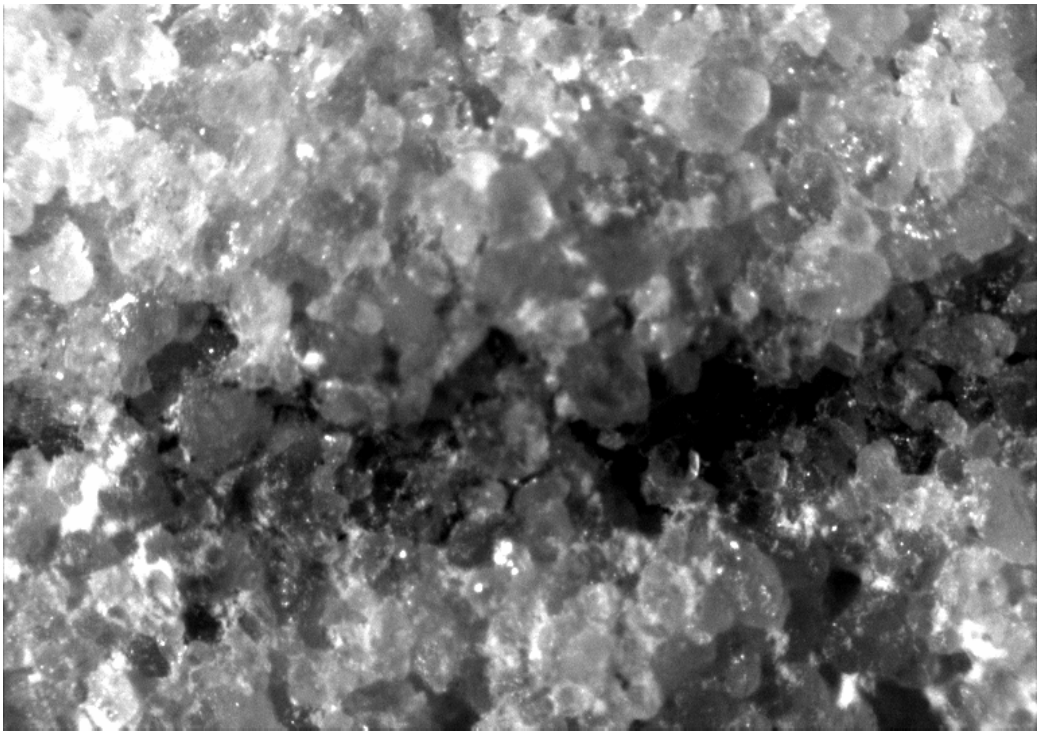

Figure 5.15: Monochrome image an Antarctica rock with an endolithic bacteria layer. This image was taken with the uncooled camera with one second of exposure at 25 ºC.

Illumination in red light reveals a different reflectivity of endolithic communities. A good depth of field and a good contrast can let us distinguish the endolithic layer in three dimensions. Although color imaging will show the color difference between the layers, black and white imaging remains sensitive to color inhomogeneities. The camera also had a good dynamic range which gave enough grayscale levels on the image. Figure 5.16 shows the fluorescence response of the same spot with the bluish green LED epi-illumination, with an LED current of 8 mA.

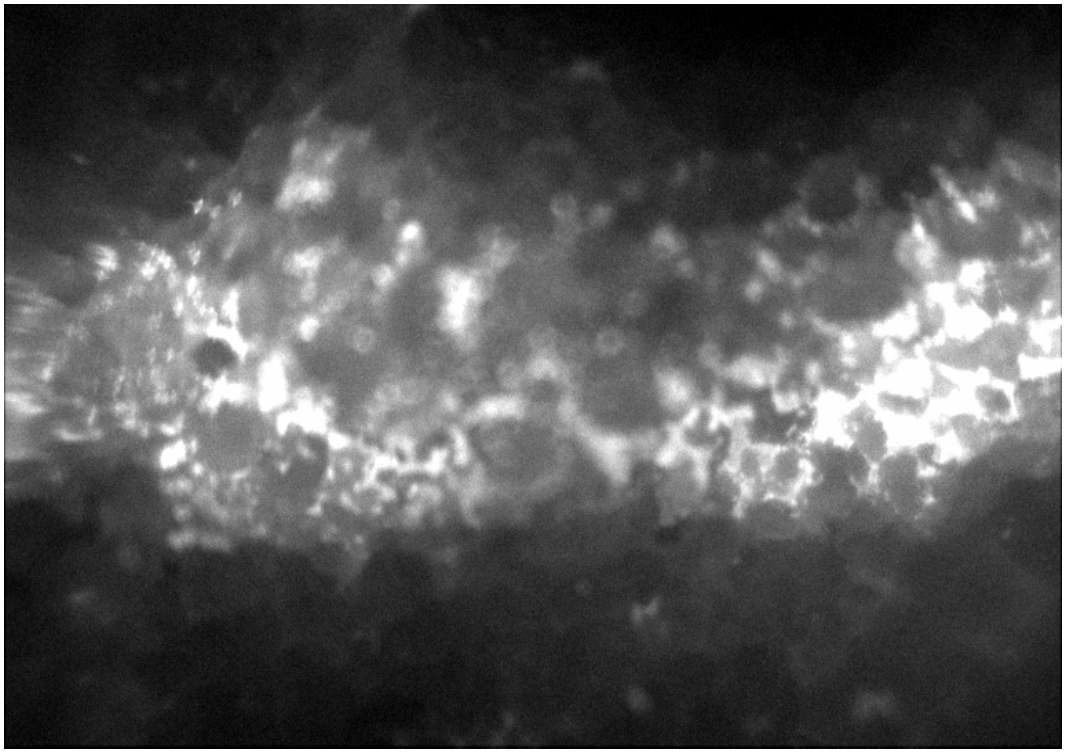

Figure 5.16: Induced fluorescence of an endolithic microbial community. This image was taken with the uncooled camera with one second of exposure at 25 ºC, with an LED current of 8 mA.

The image revealed a strong native fluorescence signal generated by the endolithic bacterial layer that was specific to the biomaterial in the rock.

Detection of PAHs

The same optical system was used to detect the presence of PAHs with a UV LED centered at 372nm. A 420nm long pass filter and a bandpass filter centered at 375 nm and 20 nm wide were also used.

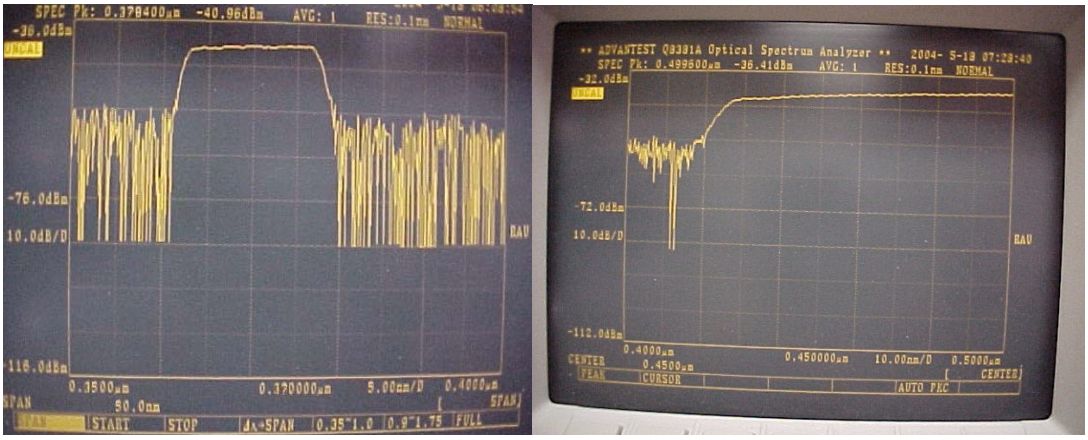

Figure 5.17: Spectra of bandpass and long-pass filter used for short UV fluorescence excitation. The left spectrum is on a 5nm per division scale, while the right spectrum in on a 10 nm per division scale.

Gas and diesel did exhibit a stronger fluorescence than the previous samples and their detection was much easier. These solutions were put on a square beaker to be imaged. Figure 5.18 shows the fluorescence of soil immersed in diesel. For the same irradiance, the fluorescence signal will change depending on the concentration of the PAHs and the dryness or humidity of the soil. In general, dry soils give a higher fluorescence intensity of the sample [7]. Even though PAHs constitute 0.2% to 0.5% of gasoline they dominate the fluorescence signal [8].

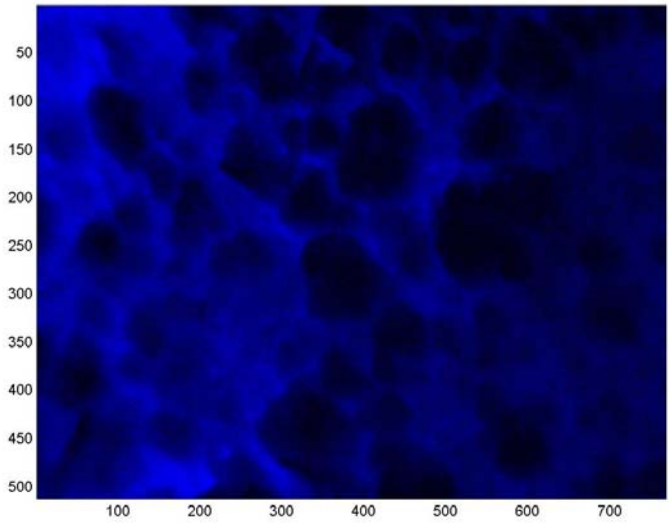

Figure 5.18: MATLAB color processed image of fluorescing diesel. This image was taken with the uncooled camera with one second of exposure at 25 ºC (LED current of 8 mA).

The next images were realized by depositing droplets of gasoline on water in a beaker. The fluorescence and black and white images were done on the same spot. The visible disks on the left hand side demonstrated strong fluorescence when exposed to UV light.

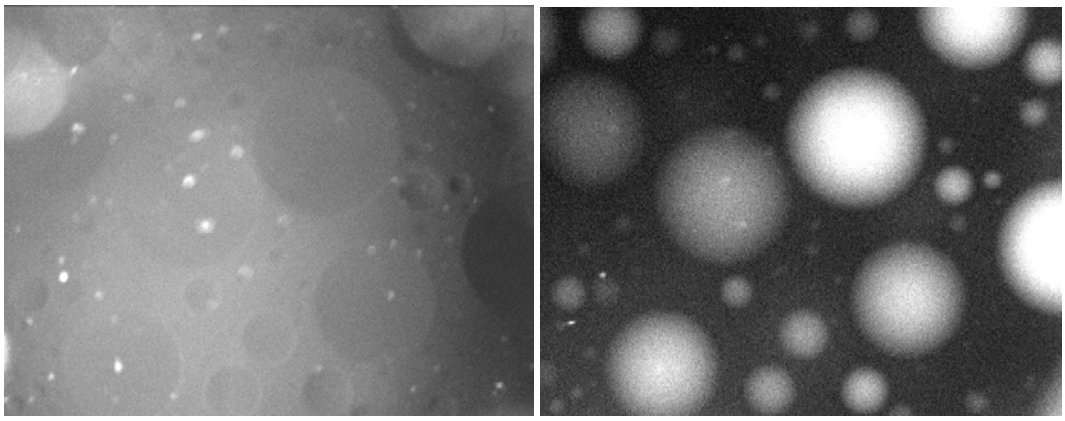

Figure 5.19: Black and white image of gasoline drops on water (left) and its corresponding UV fluorescence image (right). These images were taken with the cooled camera with one second of exposure at 10 ºC (LED current of 10 mA).

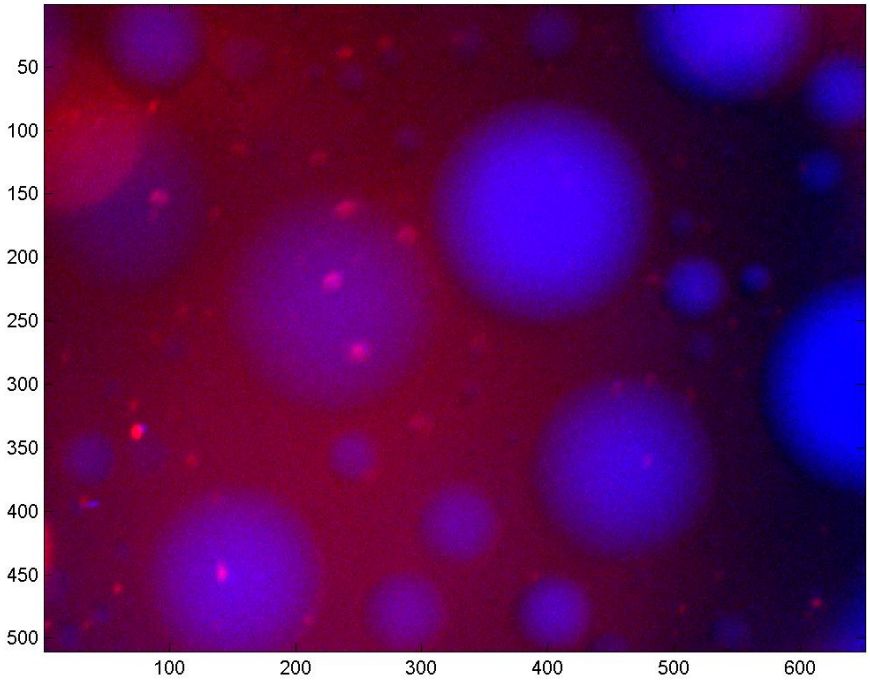

Figure 5.20: MATLAB color processed image of fluorescing gasoline.

Fluorescence Analysis Based on CCD Sensitivity

For any specimen, the intensity of fluorescence emission depends on its concentration, the excitation light intensity, and the fluorescence quantum efficiency. For each sample, there is a minimal light source irradiance that will make the fluorescence visible on the camera. Long exposure periods and high quantum efficiency of the CCD also help achieve a better detection.

The fluorescence intensity of our samples was measured with MATLAB's "improfile" function. The "improfile" function generates pixel intensity values along a chosen line of interest in the picture.

The LED irradiance was measured at the focal plane of our bench-top probe. The average irradiance on the sample was measured by fitting the sensing area of the optical power meter to the "evenly" illuminated spot. Since the LED is not a point source and because the light intensity on the sample is not homogeneous, it is more correct to talk about average irradiance. The fluorescence detection was done with an uncooled camera.

In the example below, a cross section is shown from the fluorescence of the endolithic bacteria. In this case, the necessary average irradiance to provoke a fluorescence level of 90 (on a scale of 0-256) of the endolithic bacteria was 2.49 W/m^2. The picture on the right of figure 5.21 shows a fluorescence saturated pixel intensity with an irradiance 6.86 W/m^2 at the sample. These images were taken with one second of integration time and fully opened iris using the uncooled CCD camera.

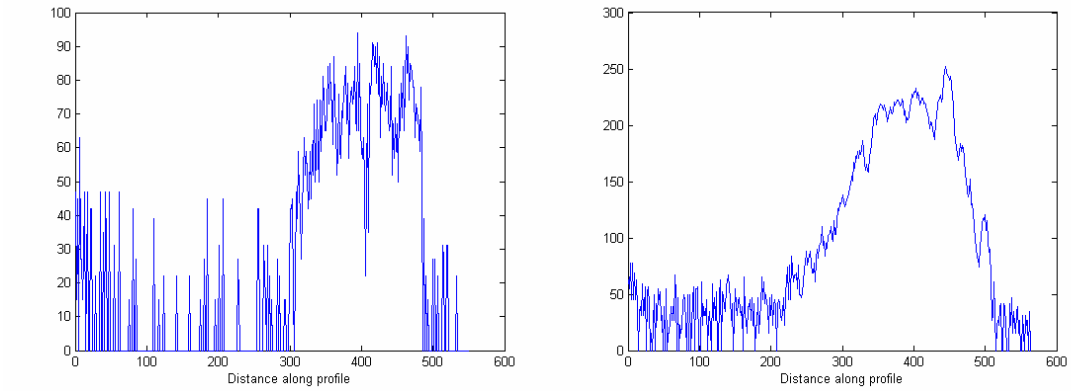

Figure 5.21: Fluorescence intensity profile of endolithic bacteria layer at 70 W/m^2 (left) (LED current of 5mA) and 150 W/m^2 (right) (LED current of 13 mA).

The next histogram in figure 5.22 shows the average irradiance necessary to saturate the pixel charge of the uncooled camera. The average irradiance was measured with the optical power meter sensor placed at a distance of 1cm from the LED. Data were gathered with a fully opened iris and at one second of integration time.

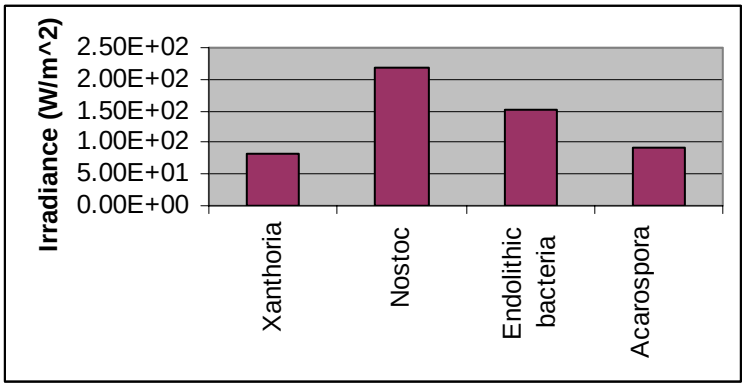

Figure 5.22: Necessary irradiance needed at the sample (λ=500nm) to induce sufficient fluorescence to saturate the pixel charge at one second of integration time.

The same tests were conducted on the PAHs with the uncooled CCD camera. The histogram in figure 5.23 shows the irradiance needed at one second of exposure time to saturate the pixel charge of the uncooled camera.

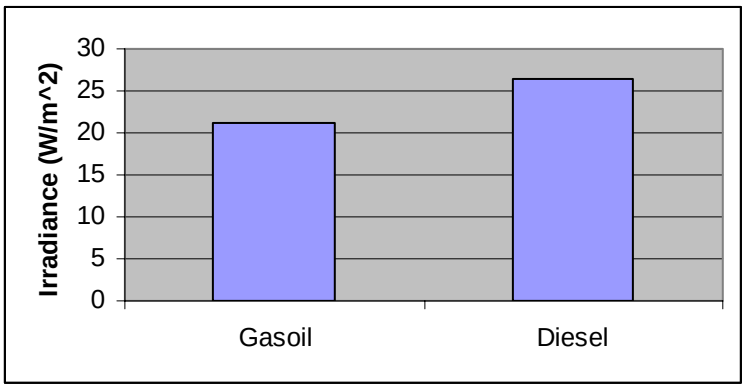

Figure 5.23: Necessary irradiance at the sample (λ=370nm) to induce fluorescence needed to saturate the pixel charge of the uncooled CCD camera at one second of integration time.

Based on the CCD sensitivity measurements described in chapter 4, the fluorescence yields of these samples are presented below. The fluorescence yield was measured by dividing the fluorescence intensity at the CCD sensor by the illumination intensity measured at 1 cm behind the LED. These yields depend on the quantum

efficiency of the sample and on the light collection efficiency and transmittance of the optical elements in our system. These efficiencies also depend on the NA, on the transmittance of our optical elements, and on the level of LED light homogeneity at the sample.

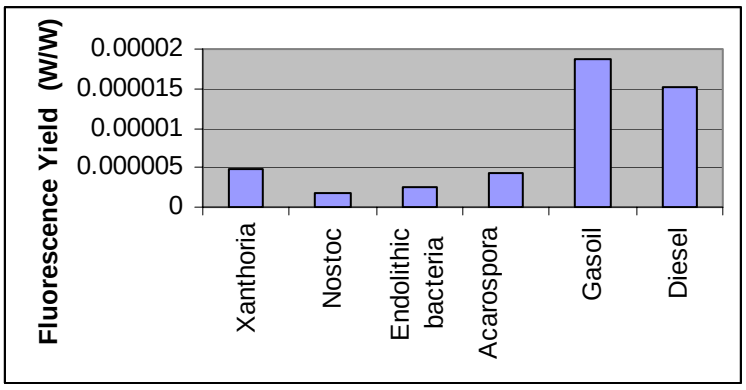

Figure 5.24: System fluorescence emission efficiencies based on CCD sensitivity at one second of exposure.

Sample	Fluorescence Yield (W/W)
Xanthoria	4.91E-06
Nostoc	1.82E-06
Endolithic bacteria	2.63E-06
Acarospora	4.35E-06
Gasoil	1.88E-05
Diesel	1.51E-05

Table 5.1: Obtained fluorescence yields with our fluorescence detection apparatus.

Illumination Uniformity

Uniform sample illumination is very dependent upon proper alignment of all the optical components, including the illumination source.

Two types of epi-illuminations techniques are possible: Kohler and critical illumination. For critical illumination, light emitted from the LED goes through a

collimating lens then gets focused with an objective lens, producing a magnified image of the LED source in the specimen plane. The magnification will depend on the location of the virtual image of the LED set by the LED's epoxy lens. In Kohler illumination, the image of the source is formed at the back focal plane of the objective lens. The spot illumination on the sample will be the Fourier transform of the image formed at the back focal plane of the objective lens. With Kohler illumination the illuminated field is more uniform.

The picture below shows the chlorophyll fluorescence of a leaf using Kohler illumination. For good fluorescence results, the leaf is supposed to be evenly fluorescing in the whole field of view. Reasonable uniformity is observed in this image.

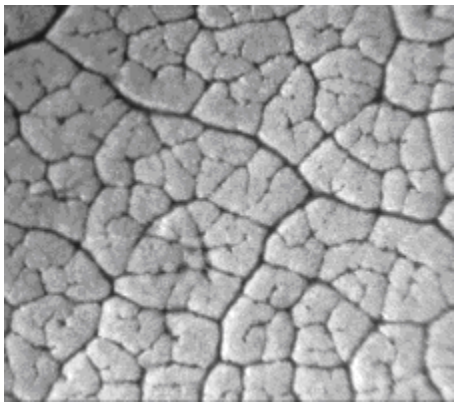

Figure 5.25: The uniform fluorescence illumination emission of a leaf.

LED Irradiance and Color Temperature Dependence

The optical characteristics of our LEDs were slightly susceptible to temperature changes. In outdoor applications, the LEDs can be exposed to extreme temperatures. Changes in temperature affect the peak emission wavelength of the LED and also its

intensity. In all circumstances, the peak wavelength of the excitation LED has to be contained within the working range of the band pass filter. The graphs in figure 5.26 and 5.27 show an example of the temperature dependence of the bluish green LED. This LED has been submitted to hot and cold temperatures. The influence of the temperature depends on the band gap and on the thermal properties of the semiconductor.

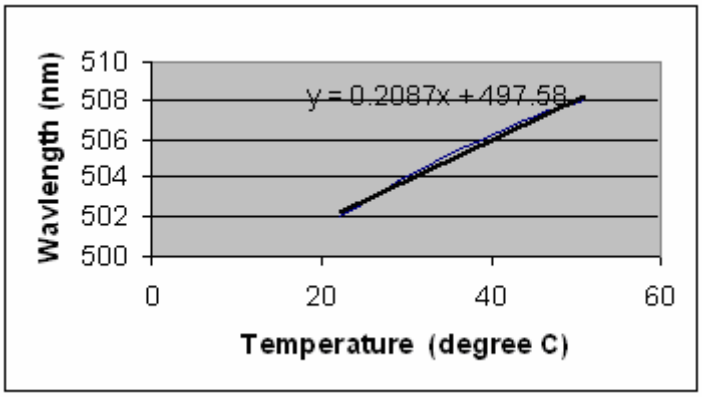

Figure 5.26: The center wavelength versus temperature change for the bluish-green LED.

The graph shows a moderate peak wavelength variation of 6nm over a 30 K range. However, the light intensity seems to be significantly attenuated at high temperatures, with a drop of 12 W/m^2 every 10 ^oK.

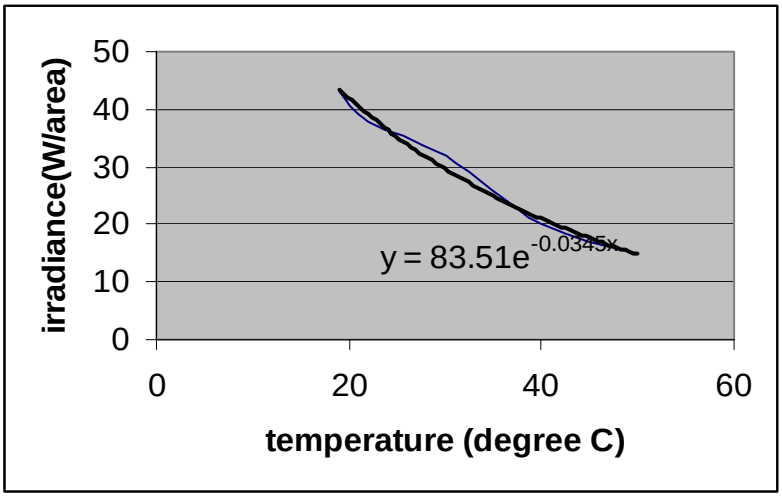

Figure 5.27: The irradiance versus temperature change for the bluish-green LED.

Once in the penetrometer, the probe's LEDs will depend on the underground temperature and on the field test conditions.

Raman Spectroscopy

In addition to fluorescence imaging, our miniature probe will also include Raman spectroscopy for sample identification. Fluorescence emission is useful for locating possible regions within the image where there might be biotic materials. To identify the nature of that material, Raman spectroscopy gives a more specific diagnostic tool. In our instrument we will accommodate a single-region Raman sample that is registered within the image for morphological context. Figure 5.28 shows an example of Raman excitation on soil. The spot was created with a 632 nm laser light for this illustration. For this illustration, the spot size diameter shown on the picture is approximately 220 μm.

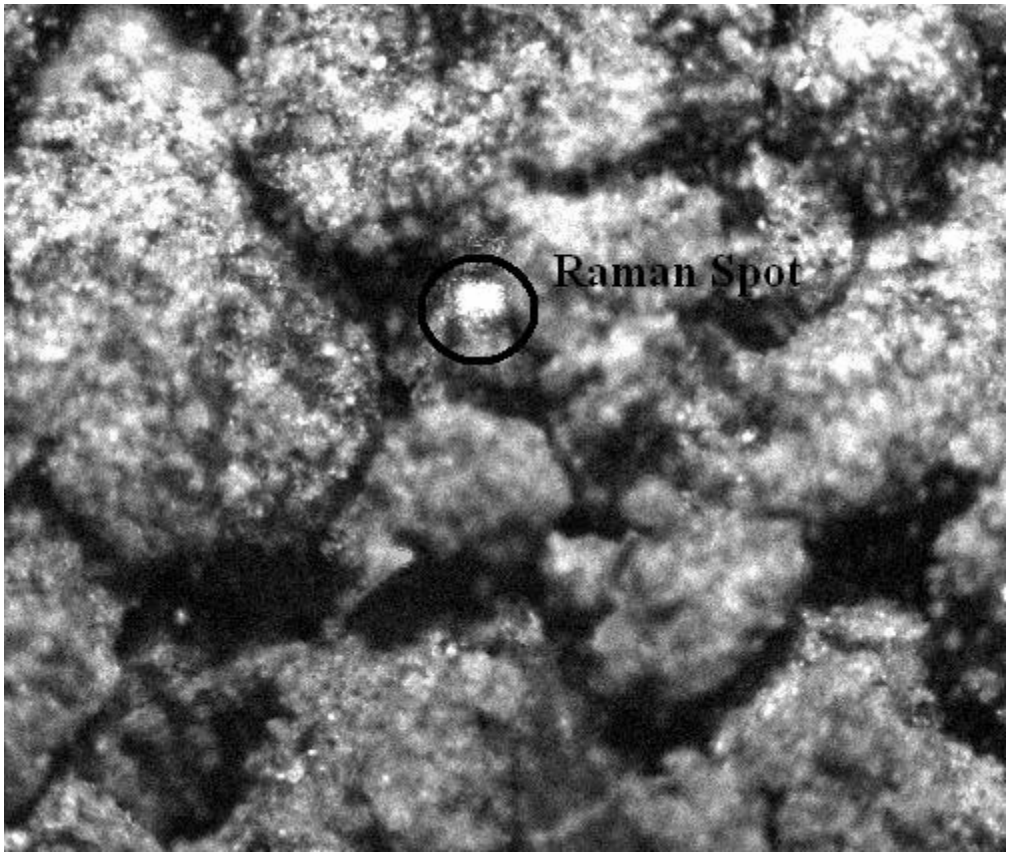

Figure 5.28: Image of soil with a centered Raman spot.

For this thesis no Raman experiments were conducted. However, prior work in our laboratory and elsewhere has illustrated the use of reflectance Raman spectroscopy to identify compounds in ground pollutants such as Benzene [9]. Also Raman has successfully identified pigments such as *Chlorophyll*, *Carotenoids*, *Scytonemin* and *Phycocyanin* [10] that may have Martian analogs, such as the Antarctic samples imaged in this thesis. The proposed probe design is fully compatible with reflectance Raman sampling for chemical identification of the imaged material.

Conclusion

With the help of a penetrometer, the LED based fluorescence probe can effectively search for the presence of underground biological traces and PAHs. Obtaining the pictures was a delicate task that required many adjustments. This will be much more complicated in the field. Because we have no knowledge of the focus position and because of surface roughness, an autonomous iris should be used to adjust the depth of field and bring all elements in the field of view in focus.

In addition to that, Raman spectra give unique fingerprints of the targeted sample. Raman signals can be difficult to obtain with the interference of fluorescence, especially for biological samples, making near IR excitation appealing.

REFERENCES CITED

[1] D. D. Wynn-Williams, H. G. M. Edwards, "Proximal Analysis of Regolith Habitats and Protective Biomolecules in Situ by Laser Raman Spectroscopy: Overview of Terrestrial Antarctic Habitats and Mars Analogs," *Icarus*, Volume 144, 2000, pp. 486-503.

[2] R. Scott, "Lichens," Chapter 10, Volume 1, pp 216-219, from <http://museum.gov.ns.ca/mnh/nature/nhns/t10/t10-11.pdf>, accessed May 5, 2003.

[3] M. Kluge, "A fungus eats a Cyanobacterium: the story of the *Geosiphon Pyriformis* Endocyanosis," *Biology and Environment*, Proceedings of the Royal Irish Academy, Volume 102B, Issue 1, 2002, pp. 11–14.

[4] U. Mathis, M. Mohr, A. M. Forss, "Comprehensive particle characterization of modern gasoline and diesel passenger cars at low ambient temperatures," *Atmospheric Environment,* Volume 39, Issue 1, January, 2005, pp. 107-117

[5] J. W. Cook, R. Schoental, E. J. Y. Scott, "Relation between Bond Structure and the Longest Ultra-violet Absorption Band of Polycyclic Aromatic Hydrocarbons," Chemistry Department, University of Glasgow, 28th November 1949.

[6] Molecular Probes, Inc. 29851 Willow Creek Road, Eugene, OR 97402, Phone: (541) 335-0338, from <http://www.probes.com/handbook/>, accessed May 17, 2003.

[7] M.L. Kram, A. A. Keller, "Complex NAPL site characterization using fluorescence Part 2: Analysis of soil matrix effects on the excitation/emission matrix," *Soil sediment and contamination*, volume 13, issue 2, 2004, pp. 119-134.

[8] ML Kram, AA Keller, SM Massick, et al, "Complex NAPL site characterization using fluorescence Part 1: Selection of excitation wavelength based on NAPL composition," *Soil sediment and contamination*, volume 13, issue 2, 2004, pp. 103-118.

[9] D. M. Crowder "A confocal microscope and Raman spectroscopy probe for Mars exploration". Master's Thesis, Montana State University, April 2002.

[10] D.D. Wynn-Williams, H.G.M. Edwards, E.M. Newton, J.M. Holder, "Pigmentation as a survival strategy for ancient and modern photosynthetic microbes under high ultraviolet stress on planetary surfaces," *International Journal of Astrobiolog,* Volume 1 Issue 1, May 2002, pp. 39-49.

CHAPTER SIX

DESIGN FOR COMPACT PENETOMETRER OPTICAL MODULE WITH IN-SITU AND FLUORESCENCE IMAGING AND RAMAN SAMPLING.

This chapter describes the optics of our probe design. This design is informed from our table top apparatus. We considered the following parameters that we considered when making this design: miniaturization, light collection, and filter efficiency. New elements on our optical design will be introduced. Due to their minimal size and efficiency these elements will help in reducing the size of the probe. In addition to that, more efficient filters will be proposed to maximize the excitation light transmission.

Probe Configuration

As discussed before, the probe will be divided into three compartments. Our design recommendations will only focus on the optical side of the probe.

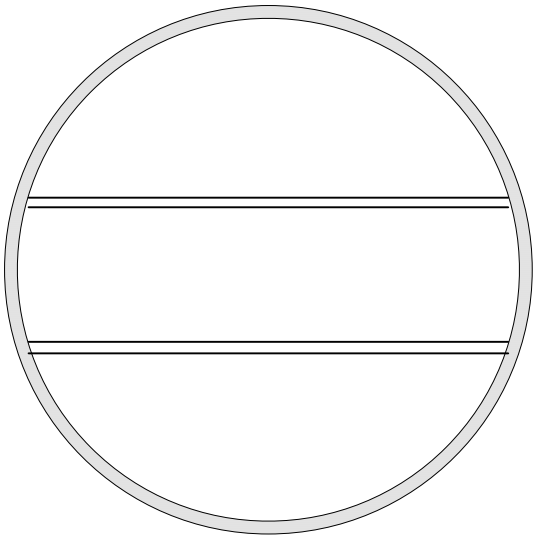

Figure 6.1: Cross section view of the probe.

Figure 6.1 shows the cross section image of a penetrometer; existing penetrometers' diameter ranges from an inch to two inches. After many drawings and modifications, we agreed on a final design for our probe. The next illustration shows the setup of the suggested probe.

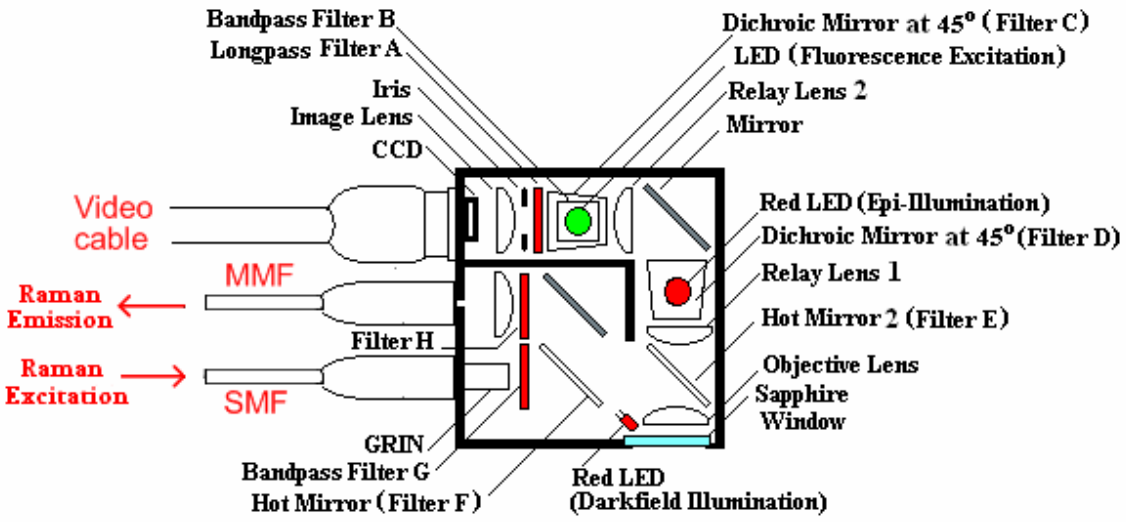

Figure 6.2: Probe design of the Raman and fluorescence probe.

This design is very similar to the table-top design used in our experiments. For the fluorescence apparatus, a few modifications were made such as the addition of relay lenses and the use of a different spatial organization.

For fluorescence and reflected light imaging we have decided to use the R47-146 aspheres from Edmund Optics [1] with a lens outer diameter of 6.325 mm and a clear aperture of 4.8mm. Identical aspheres will be used for the objective and image lens. With a focal length of 4mm, the objective asphere will offer a high NA of 0.6.

The plano-convex relay lenses were introduced to increase the field of view by minimizing the distance between the objective lens and the first relay lens. The two relay lenses are identical and separated by the sum of their focal lengths which will result in unit magnification. For a large field of view with no vignetting, large diameter relay lenses are desirable. The field of view should have the minimum size of the CCD sensor.

The thickness of the sapphire window will be chosen to match the characteristics of the asphere. For ideal lens matching and minimal aberrations, a similar glass window can be used with the CCD imaging aspheric lens.

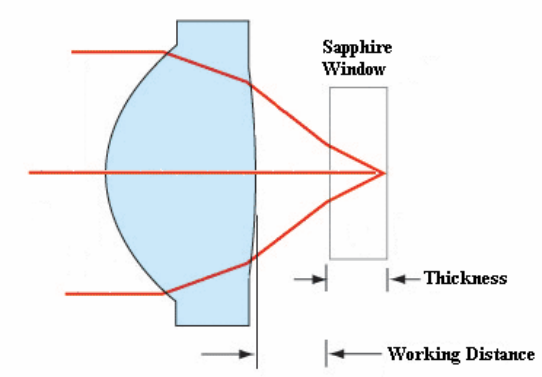

Figure 6.3: Scheme of the aspheric lese used as an objective lens.

Our aspheric lens is designed to work with a1.20 mm thick glass window with a working distance of 1.53 mm. To withstand the scratching associated with soil

penetration, our design will replace the glass window with one made of sapphire. The refractive index of the sapphire window is 1.755; this change will require a window thickness of 1.04 mm.

Two mirrors are used in our design; their coating will ensure maximum reflectivity for the UV/visible and IR for fluorescence and Raman respectively. The next figure shows a 3D image of the probe.

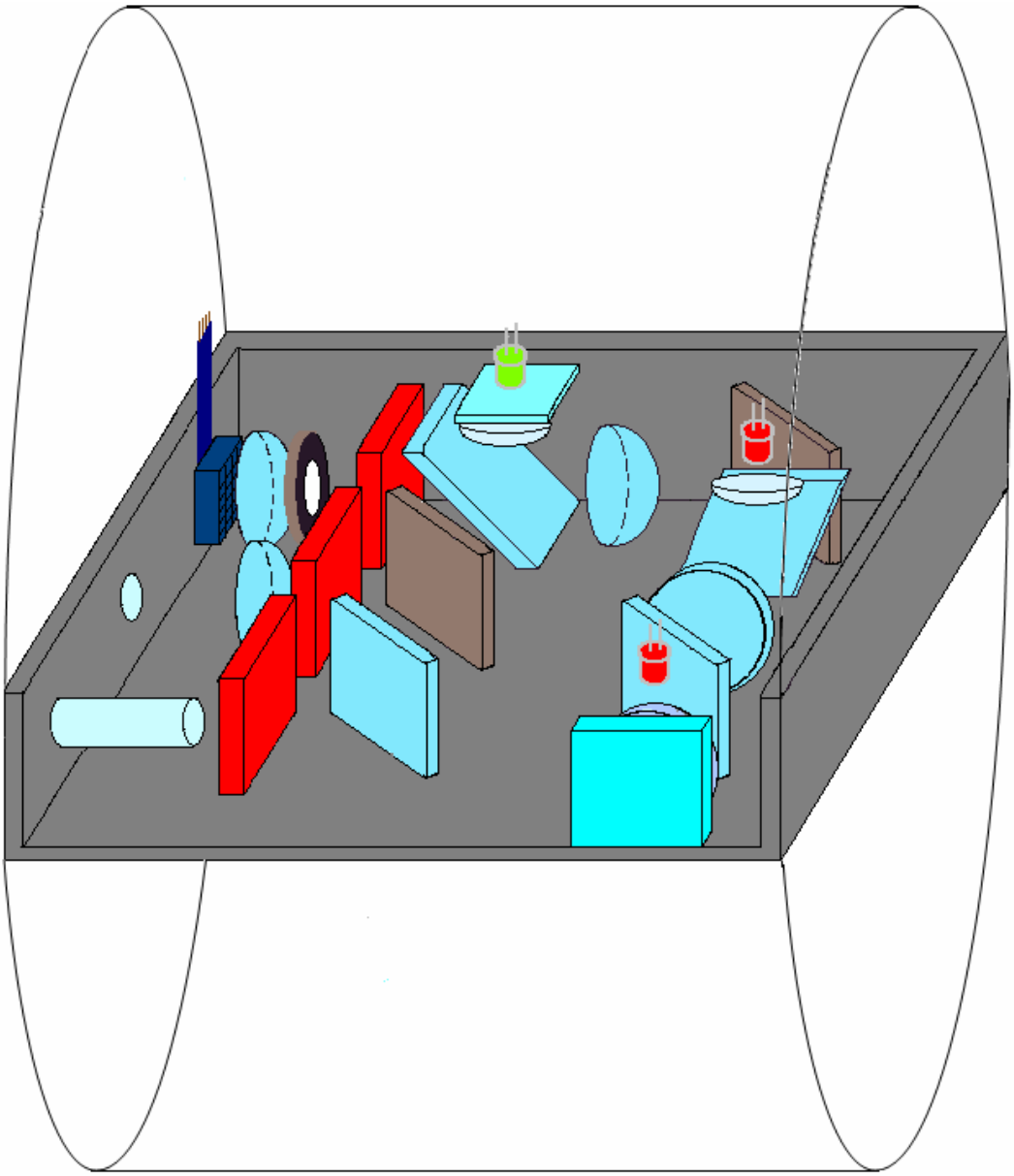

Figure 6.4: A 3D view of the final probe design.

Figure 6.5 shows the proposed Panasonic CCD sensor for the probe design. This quarter inch CCD sensor is one of the smallest available on the market and offers an acceptable signal to noise ratio of 55dB. Due to its small size, this CCD can easily be incorporated into the probe. The sensing area of this CCD camera is 3.65 by 2.74 mm. Due to this small CCD size, no magnification will be used; therefore, the imaging and objective lens will be similar.

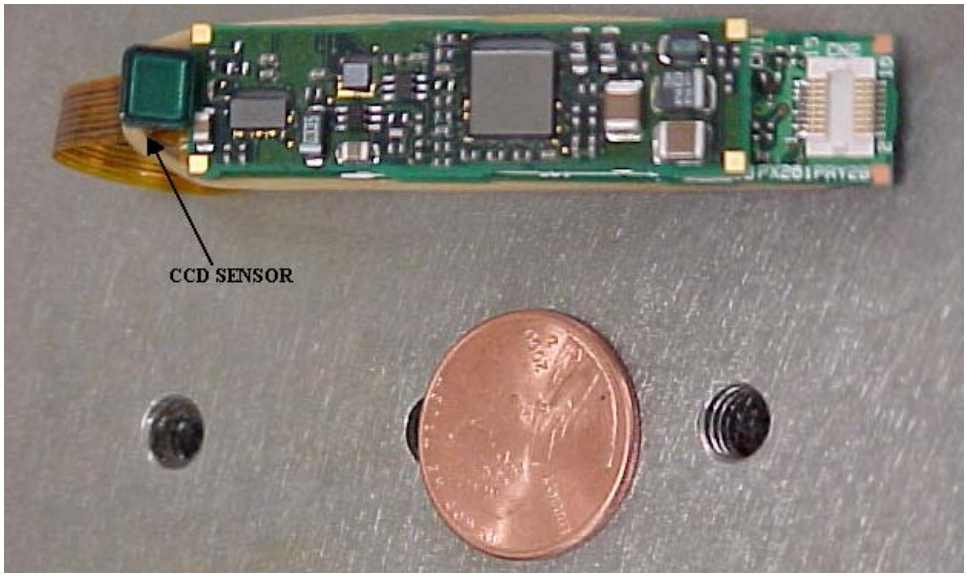

Figure 6.5: Black and White Panasonic ¼" CCD.

The Panasonic GP-KS462 CCD sensor has square pixels of 4.75 um [2]. By choosing the same focal length for the objective and CCD lens, the resolution of the CCD will be almost equal to its pixel size.

The spectra of the filters used in the above design are described in the next sections. These spectra were obtained from Omega Optical, Inc [3] and Chroma technologies, Inc [4].

Fluorescence Filters

In this section the filters used for fluorescence application will be introduced by starting with the bluish-green induced fluorescence. These filters should ensure a good transmission of LED light with the lesser attenuation possible. For miniaturization purposes, bandpass filters can be omitted by choosing LED with narrower spectrum. However, their use will ensure a finer selection of the excitation wavelengths.

The long pass filter (Filter A, OG540) will suppress the bluish-green LED excitation wavelengths that reach the CCD from internal reflections within the probe and Rayleigh scattering from the sample. Together, the dichroic (Filter C, 535DCLP80) and long pass filter will result in a better blocking of the scattered light. The criteria of the filters are chosen in order to eliminate any overlap between the longpass and the bandpass filter (Filter B, 500DF25) and to achieve a high cumulative attenuation of O.D 5.69 at 530nm. Figure 6.6 shows the spectra of the chosen bandpass filter with 25 nm at FWHM.

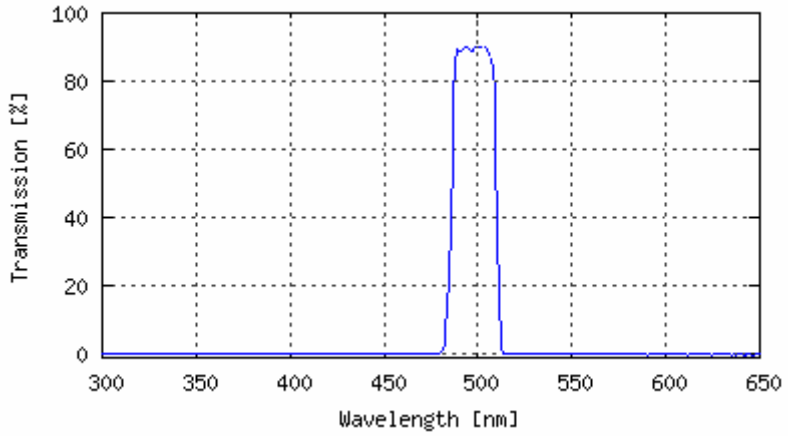

Figure 6.6: Spectra of the bandpass excitation filter (Filter B, 500DF25) from Omega Optical, Inc. used with bluish green LED.

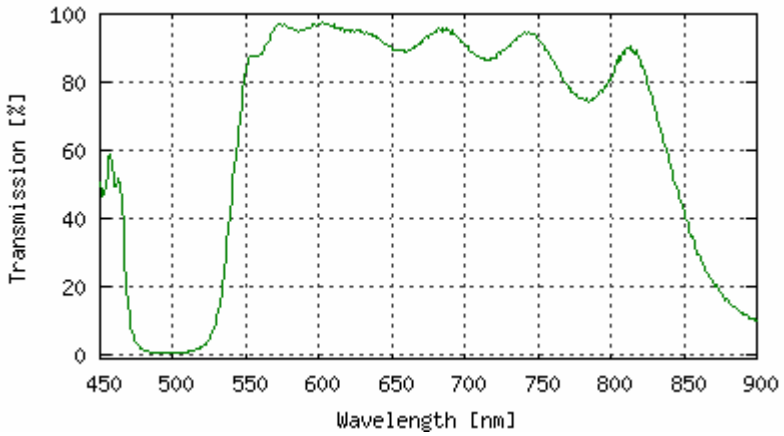

Figure 6.7: Spectra of the 45 degree dichroic (Filter C, 535DCLP80) from Omega Optical, Inc. used with bluish green LED.

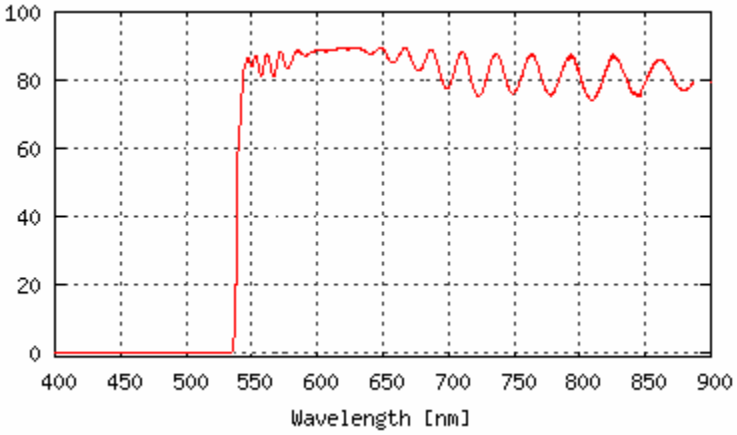

Figure 6.8: Spectra of the longpass filter (Filter A, OG540) from Omega Optical, Inc. used with bluish green excitation.

The filters' spectra were obtained from Omega Optical, Inc. They come in different shapes and with a minimal thickness of 1 mm.

The filters used for the UV induced fluorescence are presented below.

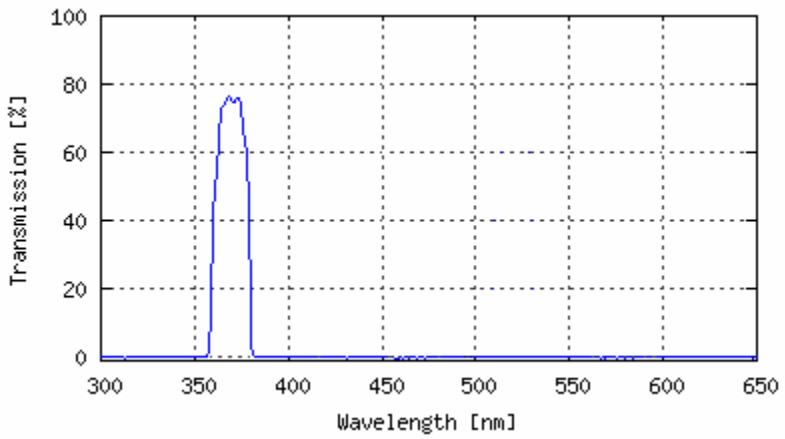

Figure 6.9: Spectra of the Omega Optical filters used for UV excitation. A bandpass excitation filter (Filter B, 370DF15).

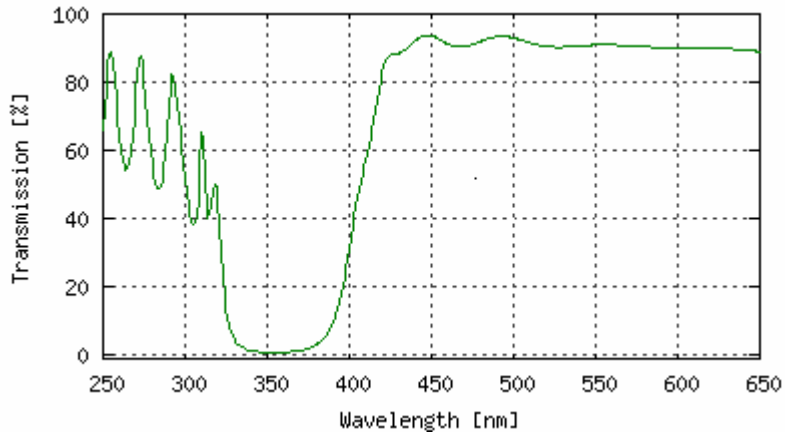

Figure 6.10: Spectra of the Omega Optical 45 degree dichroic (Filter C, 355DCLP80) used for UV excitation.

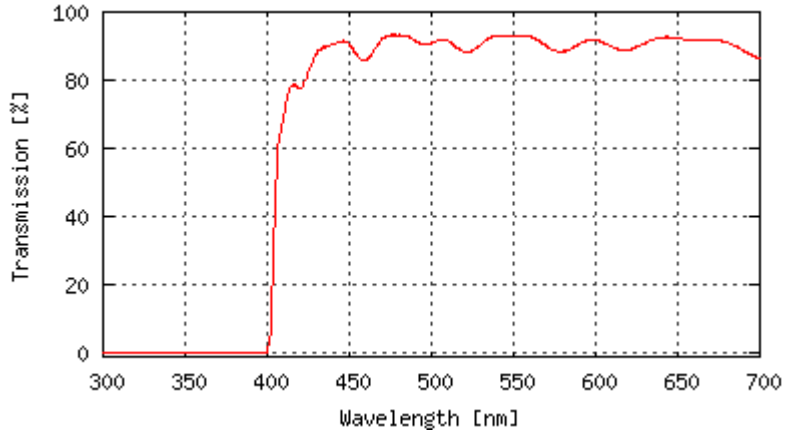

Figure 6.11: Spectra of the Omega Optical longpass filter (Filter A, OG405) used for UV excitation.

With the filters used for UV induced fluorescence, RGB color imaging becomes possible.

Black and white imaging will be done with epi and darkfield illumination using red light. The dichroic (Filter D, 290DCLP) used for the epi-illumination will to have a high transmission and low reflection as presented below.

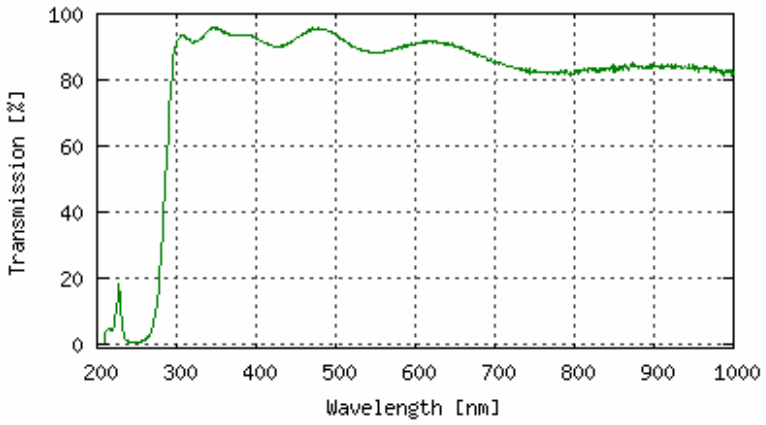

Figure 6.12: Spectra of the 45 degree dichroic used for epi-illumination (Filter D, 290DCLP) from Omega Optical.

A 90 % transmission on the visible spectrum will maximize the collection of fluorescence, while allowing enough light for illumination to do reflected light imaging. For a good lighting on the sample, the LED used for epi-illumination will be driven at high currents to compensate for the low reflectivity of the dichroic.

With the previously demonstrated filters, light will experience a 51% transmission (round-trip) for the UV induced fluorescence, compared to 28% for the bench top system. For the bluish-green induced fluorescence, light will experience a 61% transmission (round-trip), compared to 49% for the bench top system. This change will result in higher

light capture efficiency. More light will be captured by the Panasonic GP-KS462 CCD sensor which will partially make up for its lower signal-to-noise ratio of 50 dB.

Raman Setup

A single mode fiber will be used to deliver the laser light to the Raman part of the probe; whereas, a multimode fiber will route the detected signal back to the spectrometer. Because single mode fibers have a lower core diameter, their use will result in tighter Raman spots on the sample. A multimode fiber will be used to achieve better light collection efficiency.

In the probe, the Raman excitation light will be collimated by a quarter-pitch GRIN, also known as graded index lens. The GRIN will be cemented to the excitation single mode fiber. Several GRINs can be used depending on the desired width of the collimated beam. In general, the length of the GRIN lens is below 5mm and their diameter ranges from 0.25 to 3.0mm. The GRIN diameter will determine the beam width. The laser beam width will stay almost constant between the GRIN and the objective lens. A larger Raman excitation beam will result in a smaller spot on the sample and vice versa. With a beam width of 0.5mm, the estimated Raman spot size on the sample will be approximately 2 μm. Relay lenses can also be introduced on the Raman path to modify the beam width and the spot size.

For a high light coupling efficiency, the numerical aperture of the GRIN should be about 1.5 times the NA of the excitation fiber. The same rule should be followed when focusing light into the multimode fiber. In this case, the multi-mode fiber will have about

1.5 times the NA of the focusing lens. Despite the geometric and spherical aberrations generated by the lens, the core diameter of the MM fiber will be large enough to gather the entire Raman signal.

Raman Filters

Representative Raman filters are presented for 852nm excitation. Although the spectral width of the laser diode source will not exceed 1 nm, the following band pass filter (Filter G, 850DF7) will pass the excitation beam with 7 nm of FWHM.

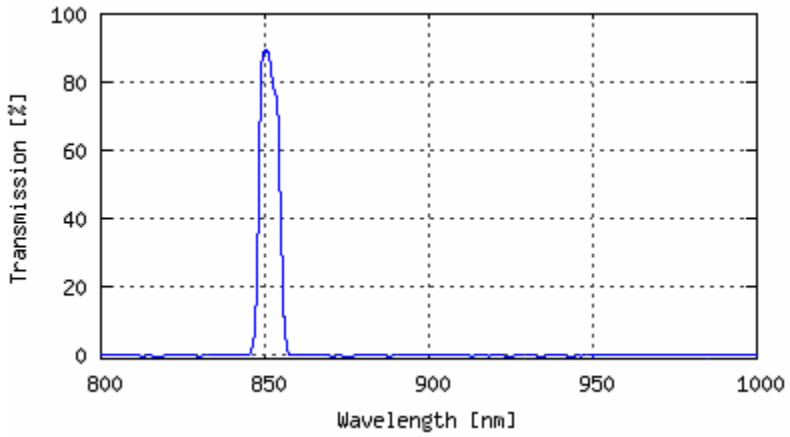

Figure 6.13: Raman excitation filter (Filter G, 850DF7) from Omega Optical, Inc.

Presented below is the spectrum of our first hot mirror (Filter F, 865DCSPXR). The transmission curve of this filter will depend on the attributes of the Raman spectrometer. The wave-numbers of our Raman spectrometer range from 350 to 1600 cm^{-1}. For the case of 852 nm excitation wavelength, these wave-numbers will correspond to a range of 878 to 986 nm. The selection of the coming Raman filters will be based on these numbers.

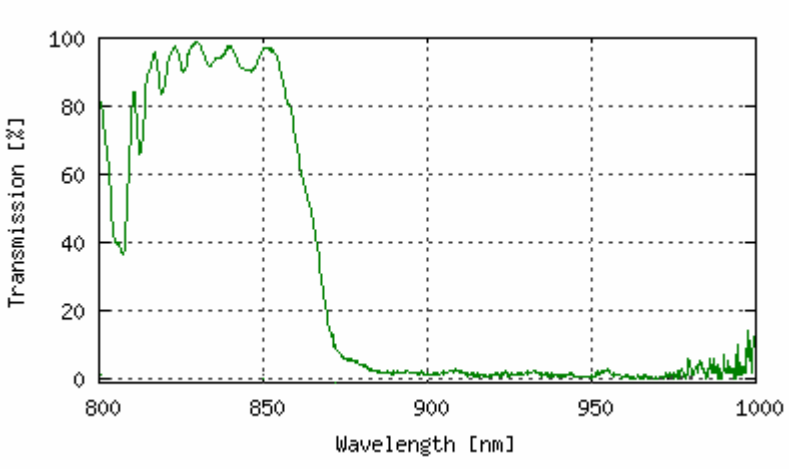

Figure 6.14: Raman hot mirror (Filter F, 865DCSPXR) from Omega Optical, Inc.

This 45 degree angled dichroic filter will pass wavelengths below 855 nm and reflects wavelengths higher than 875nm (875-1000).

The second 45 degree hot mirror (Filter E) will be shared between the fluorescence and the Raman optical path. This mirror will reflect wavelengths above 800 nm (800-1000) and pass wavelengths between 350 and 750 nm.

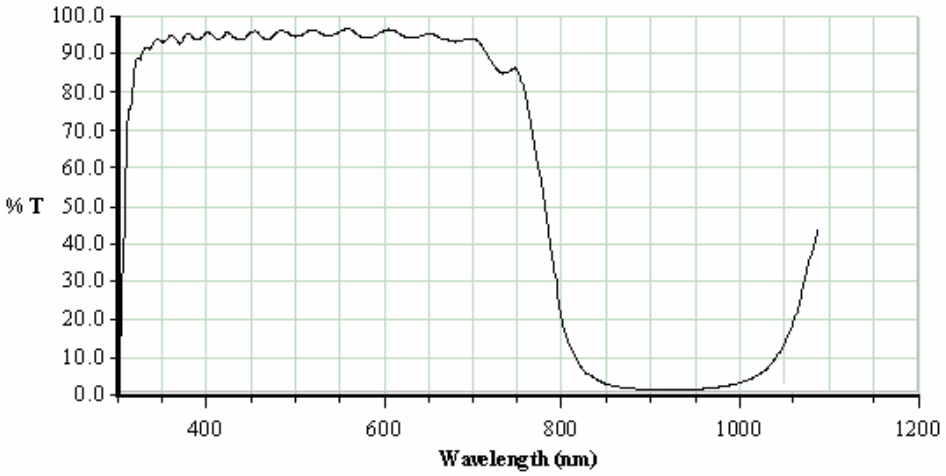

Figure 6.15: Raman second hot filter (Filter E, 770DCSP) from Chroma Technologies, Inc.

Finally, a long pass filter (Filter H) will pass all wavelengths above 878 nm and reflect shorter wavelengths.

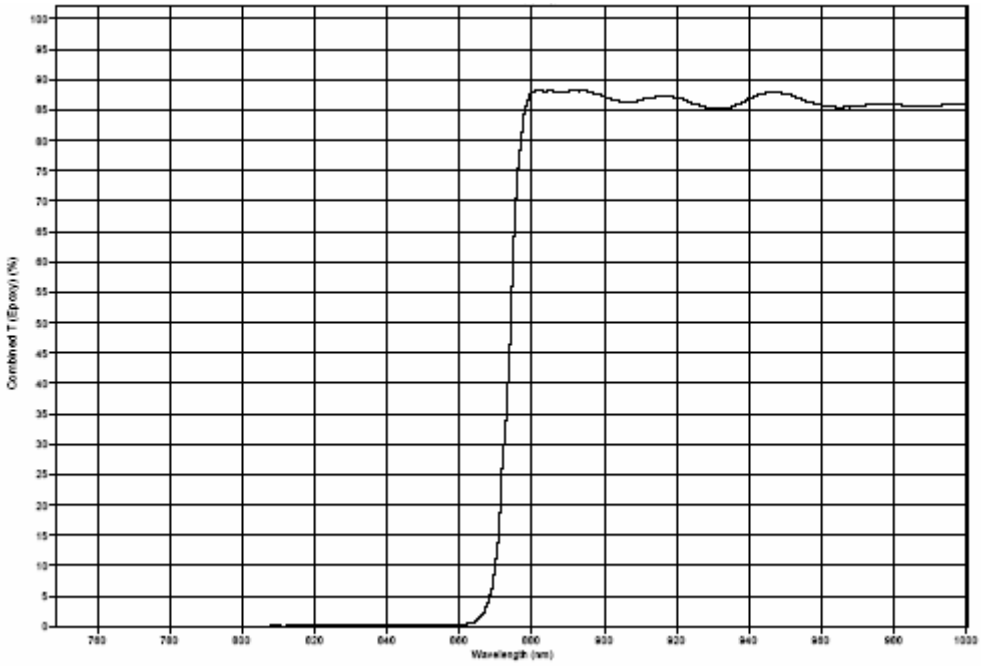

Figure 6.16: Raman longpass filter (Filter H, 874ALP) from Omega Optical, Inc.

This filter will eliminate any reflected light below 878 nm and ensure the proper working of our Raman optics.

Conclusion

The above design for fluorescence and Raman optics does not differ significantly from our tested system. The theoretical feasibility of the probe was demonstrated; however, only the building and testing can reveal the overall aberrations and optical flaws associated with this design.

REFERENCES CITED

[1] Edmund Optics Inc. 101 East Gloucester Pike, Barrington, NJ/USA 08007-1380, Phone: (800) 363-1992, from <http://www.edmundoptics.com/techsupport/>, accessed August 9, 2003.

[2] The Imaging Source, Suite 400, 1201 Greenwood Cliff, Charlotte, NC 28204, Tel: +1 704-370-0110, from <http://www.theimagingsource.com/prod/cam/gpks462/gpks462_ds.pdf>, accessed August 1, 2003.

[3] Chroma Technology Corp., 10 Imtec Lane, PO Box 489, Rockingham, VT 05101, Phone: 800-824-7662, from <http://www.chroma.com/filters>, accessed August 1, 2003.

[4] Omega Optical, Inc., 210 Main Street, Brattleboro, VT 05301, Phone: (866) 488-1064, from <http://www.omegafilters.com/curvomatic>, accessed August 10, 2003.

CHAPTER SEVEN

CONCLUSION

This thesis has presented the design of a probe combining Raman, fluorescence, and reflected light imaging. Although the FIRP probe was not constructed in its entirety, the performance and the abilities of fluorescence, and black and white imaging were demonstrated and verified, and compatibility with Raman sampling was maintained.

The LED proved to be efficient in inducing the fluorescence of our samples and helped in miniaturizing the probe design. The LED, at a peak wavelength of 500nm, induced fluorescence of our lichens and endolithic biological specimens. Real-time imaging with the CCD gave good visual detection. The detection of weak fluorescing signals was made possible by increasing the exposure time and adjusting the LED light intensity. Exposure times from 0.1 to 1 second were used to generate these images. The understanding of the CCD noise behavior gave us an optimal working range of exposure times and temperature for this imaging sensor.

Infra-red Raman excitation has been shown to give a good and distinct fingerprint of our Antarctica samples and aromatic molecules. The building of the FIRP subsequently will assess its efficiency and the repeatability of its results.

Future Work

To prove the utility, reliability and repeatability of the results, the probe will have to be built and tested in the intended application, including testing over temperature changes and in the presence of vibrations and shocks in the field.

Future work will require an overall quantification and optimization of the optical aberrations and an optimization of the filters and optical elements. Further miniaturization can be achieved by the searching for smaller optical elements or by optimizing the space between these elements.

More experiments should be done to test the system with different concentrations of aromatic molecules and with different types of soil. LED light intensity and CCD exposure should be calibrated according to the obtained results. Calibration is necessary to avoid blooming of the CCD and to ensure a satisfying signal to noise ratio of the fluorescence signal.

Color imaging of soil with blue, green, and red LED illumination can also be introduced using a monochrome CCD. This will give more details by showing the color of the specimen and could be combined with UV fluorescence through a minimal modification of the probe design.

For stronger Raman signals, shorter excitation wavelength are possible provided that there will be no interference with the visible fluorescence signal.

The introduction of movable mirrors along the Raman path can provide an automatic focus control of the Raman spot in the entire field of view. However, with the

risk of severe vibrations, the permanently fixed optics will give more stability to the probe.

These and other changes in the probe design will be assessed only after undergoing field trials.